

Identifying a Training-Set Attack’s Target Using Renormalized Influence Estimation

Zayd Hammoudeh Daniel Lowd

University of Oregon
Eugene, Oregon, USA
{zayd,lowd}@cs.uoregon.edu

ABSTRACT

Targeted training-set attacks inject malicious instances into the training set to cause a trained model to mislabel one or more specific test instances. This work proposes the task of *target identification*, which determines whether a specific test instance is the target of a training-set attack. Target identification can be combined with *adversarial-instance identification* to find (and remove) the attack instances, mitigating the attack with minimal impact on other predictions. Rather than focusing on a single attack method or data modality, we build on influence estimation, which quantifies each training instance’s contribution to a model’s prediction. We show that existing influence estimators’ poor practical performance often derives from their over-reliance on training instances and iterations with large losses. Our *renormalized* influence estimators fix this weakness; they far outperform the original estimators at identifying influential groups of training examples in both adversarial and non-adversarial settings, even finding up to 100% of adversarial training instances with no clean-data false positives. Target identification then simplifies to detecting test instances with anomalous influence values. We demonstrate our method’s effectiveness on backdoor and poisoning attacks across various data domains, including text, vision, and speech, as well as against a gray-box, adaptive attacker that specifically optimizes the adversarial instances to evade our method. Our source code is available at https://github.com/ZaydH/target_identification.

CCS CONCEPTS

- Security and privacy; Theory of computation → Adversarial learning.

KEYWORDS

Target Identification; Backdoor Attack; Data Poisoning; Influence Estimation; TracIn; GAS; Influence Functions; Representer Point

This is an extended version which includes additional details that did not fit in the peer-reviewed version. Not for redistribution. The definitive, peer-reviewed version is published in the proceedings of CCS’22 [27].

Permission to make digital or hard copies of all or part of this work for personal or classroom use is granted without fee provided that copies are not made or distributed for profit or commercial advantage and that copies bear this notice and the full citation on the first page. Copyrights for components of this work owned by others than the author(s) must be honored. Abstracting with credit is permitted. To copy otherwise, or republish, to post on servers or to redistribute to lists, requires prior specific permission and/or a fee. Request permissions from permissions@acm.org.

CCS ’22, November 7–11, 2022, Los Angeles, CA, USA

© 2022 Copyright held by the owner/author(s). Publication rights licensed to ACM. ACM ISBN 978-1-4503-9450-5/22/11...\$15.00
<https://doi.org/10.1145/3548606.3559335>

1 INTRODUCTION

Targeted training-set attacks manipulate an ML system’s prediction on one or more *target* test instances by maliciously modifying the training data [2, 22, 31, 50, 63, 64, 73]. For example, a retailer may attempt to trick a spam filter into mislabeling all of a competitor’s emails as spam [64]. Targeted attacks require very few corrupted instances [73], and their effect on the test error is quite small, making them harder to detect [11] than *availability training-set attacks* [11], which are indiscriminate/untargeted and seek to degrade an ML system’s overall performance [7, 20, 79].

Kumar et al.’s [39] recent survey of business and governmental organizations found that training-set attacks were the top ML security concern, due to previous successful attacks [40]. Kumar et al. specifically identify defenses against such attacks as a significant, practical gap. Existing training-set defenses [21, 55, 80] change the training procedure to mitigate the impact of an attack but provide little information about the attacker’s goals, methods, or identity. Learning more about the attacker is essential for anticipating their attacks [56], designing targeted defenses [1], and even building defenses outside the ML system, such as stopping spammers through their payment processors [41].

This paper’s defense against training-set attacks focuses on the related goals of learning more about an attacker and stopping their attacks. We achieve this through a pair of related tasks:

- (1) *target identification*: identifying the target of a training-set attack, which may provide insight into the attacker’s goals and how to defend against them; and
- (2) *adversarial-instance identification*: identifying the malicious instances that constitute the training-set attack.

We are not aware of any work that studies training-set attack target identification beyond very simple settings.

Our *key insight* is the synergistic interplay between the two tasks above. If attackers can add only a limited number of training instances (as is often the case) [11, 64, 73], then these malicious instances must be highly influential to change target predictions. Thus, targets are those test instances with an unusual number of highly influential training examples. In contrast, non-targets tend to have many weak influences and few very strong ones. Thus, if we can (1) determine which training instances influence which predictions and (2) detect anomalies in this distribution, then we can jointly solve both tasks.

Unfortunately, determining which training instances are responsible for which model behaviors remains a challenge, especially for complex, black-box models such as neural networks. *Influence estimators* [9, 12, 18, 35, 57, 81] attempt to quantify how much each training example contributes to a particular prediction. However, current influence analysis methods often perform poorly [5, 83].

This paper identifies a weakness common to many influence estimators [12, 35, 57, 81]: they induce a *low-loss penalty* that implicitly ranks confidently-predicted training instances as uninfluential. As a result, existing influence estimators can systematically overlook (groups of) highly influential, low-loss instances. We remedy this via a simple *renormalization* that removes the low-loss penalty. Our new *renormalized influence estimators* consistently outperform the originals in both adversarial and non-adversarial settings. The most effective of these, *gradient aggregated similarity* (GAS), often detects 100% of malicious training instances with no clean-data false positives.

Our framework for identifying targets of training-set attacks, FIT, compares the distribution of influence values across test instances checking for anomalies. More concretely, FIT marks as potential targets those test instances with an unusual number of highly influential instances as explained above. Next, FIT mitigates the attack’s effect by removing exceptionally influential training instances associated with the target(s). Since mitigation considers only targets, training instance outliers that are “helpful” to non-targets are unaffected. This *target-driven mitigation* has a positive or neutral effect on clean data yet is highly effective on adversarial data where finding even a single target suffices to disable the attack on almost all other targets.

By relying on the concepts of influence estimation and not the properties of a particular attack or domain, GAS and FIT are *attack agnostic* [62]. They can apply equally well to different attack types, including *data poisoning* attacks, which target unperturbed test data, and *backdoor* attacks on test instances activating a specific trigger. Our approach works across data domains from CNN image classifiers to speech recognition to even text transformers.

In addition to learning more about the attack and attacker, *target identification enables targeted mitigation*. Certified training-set defenses [28, 33, 42, 68, 77, 78] (which do not identify targets) implement countermeasures (e.g., smoothing [74]) that affect predictions on *all* instances – not just the very few targets. These methods can substantially degrade performance, in some cases causing up to 10× more errors on clean data [20, 28]. A strength of deep neural networks is that they can “memorize” instances to learn rare cases from one or two examples [18]; certified training prevents this by limiting any single training instance’s influence.

Our work’s contributions are enumerated below. Note that additional experiments and the proof are in the supplemental materials.

- (1) We identify a weakness common to all gradient-based influence estimators and provide a simple renormalization correction that addresses this weakness.
- (2) Inspired by influence estimation, we propose GAS – a renormalized influence estimator that is highly adept at identifying influential groups of training instances.
- (3) Leveraging techniques from anomaly detection and *robust statistics*, we extend GAS into a general framework for identifying targets of training-set attacks, FIT.
- (4) We use GAS in a target-driven data sanitizer that mitigates attacks while removing very few clean instances.
- (5) We demonstrate the effectiveness and attack agnosticism of GAS and FIT on a diverse set of attacks and data modalities, including speech recognition, vision, and text – even against an adaptive attacker that attempts to evade our method.

In the remainder of the paper, we begin by establishing notation and reviewing prior work (Sections 2 and 3). Then in Section 4, we show how existing influence estimators are inadequate for identifying (groups of) highly influential training instances. We also introduce our renormalization fix for influence estimation and describe our renormalized influence estimators. Section 5 builds on these improved influence estimates to define a framework for identifying the targets of an attack and mitigating the attack’s effect. We demonstrate the effectiveness of our methods in Section 6.

2 PROBLEM FORMULATION

Notation $x \in \mathcal{X}$ denotes a *feature vector* and $y \in \mathcal{Y}$ a *label*. Training set, $\mathcal{D}_{\text{tr}} = \{z_i\}_{i=1}^n$, consists of n training example tuples $z_i := (x_i, y_i)$. Consider model $f : \mathcal{X} \rightarrow \mathcal{A}$ parameterized by θ , where $a := f(x; \theta)$ denotes the model’s output (pre-softmax) *activations*. θ_0 denotes f ’s initial parameters, which may be randomly set and/or pre-trained.

For *loss function* $\ell : \mathcal{A} \times \mathcal{Y} \rightarrow \mathbb{R}_{\geq 0}$, denote z ’s empirical *risk* given θ as $\mathcal{L}(z; \theta) := \ell(f(x; \theta), y)$. Consider any iterative, first-order optimization algorithm (e.g., gradient descent, Adam [34]). At each iteration $t \in \{1, \dots, T\}$, the optimizer updates parameters θ_t from loss ℓ , previous parameters θ_{t-1} , and batch $\mathcal{B}_t \subseteq \mathcal{D}_{\text{tr}}$ of size b . Gradients are denoted $g_i^{(t)} := \nabla_{\theta} \mathcal{L}(z_i; \theta_t)$; the gradient’s superscript “ (t) ” is dropped when the iteration is clear from context.

Let $\hat{z}_{\text{te}} := (x_{\text{te}}, \hat{y}_{\text{te}})$ be any *a priori* unknown test instance, where \hat{y}_{te} is the final model’s predicted label for x_{te} . Observe that \hat{y}_{te} may not be x_{te} ’s *true label*. Notation $\hat{\cdot}$ (e.g., \hat{z}, \hat{g}) denotes that the final predicted label $\hat{y} = f(x; \theta_T)$ is used in place of x ’s true label y .

Threat Model

The attacker crafts an *adversarial set* of perturbed instances, $\mathcal{D}_{\text{adv}} \subset \mathcal{D}_{\text{tr}}$. Denote the *clean training set* $\mathcal{D}_{\text{cl}} := \mathcal{D}_{\text{tr}} \setminus \mathcal{D}_{\text{adv}}$. We only consider successful attacks, as defined below.

Attacker Objective & Knowledge Let $X_{\text{targ}} := \{x_j\}_{j=1}^m$ be a set of target feature vectors with shared true label $y_{\text{targ}} \in \mathcal{Y}$. The attacker crafts \mathcal{D}_{adv} to induce the model to mislabel all of X_{targ} as *adversarial label* y_{adv} . $\hat{Z}_{\text{targ}} := \{(x_j, y_{\text{adv}}) : x_j \in X_{\text{targ}}\}$ denotes the *target set* and $\hat{z}_{\text{targ}} := (x_{\text{targ}}, y_{\text{adv}})$ an arbitrary target instance. To avoid detection, the attacked model’s clean-data performance should be (essentially) unchanged. *Data poisoning* attacks only perturb adversarial set \mathcal{D}_{adv} . Target feature vectors are unperturbed/benign [7, 32, 50, 73]. *Clean-label poisoning* leaves labels unchanged when crafting \mathcal{D}_{adv} from seed instances [84]. *Backdoor* attacks perturb the features of both \mathcal{D}_{adv} and X_{targ} – often with the same *adversarial trigger* (e.g., change a specific pixel to maximum value). Generally, these triggers can be inserted into any test example targeted by the adversary, making most backdoor attacks *multi-target* ($|\hat{Z}_{\text{targ}}| > 1$) [24, 45, 70, 78]. \mathcal{D}_{adv} ’s labels may also be changed.

To ensure the strongest adversary, the attacker knows any pre-trained initial parameters. Where applicable, the attacker also knows the training hyperparameters and clean dataset \mathcal{D}_{cl} . Like previous work [73, 78, 84], the attacker does not know the training procedure’s random seed, meaning the attack must be robust to randomness in batch ordering or parameter initialization.

Defender Objective & Knowledge Let \hat{Z}_{te} denote the set of test instances the defender is concerned enough about to analyze

as potential targets.¹ Our goals are to (1) *identify* any attack targets in $\widehat{\mathcal{Z}}_{\text{te}}$, and (2) mitigate the attack by removing the adversarial instances \mathcal{D}_{adv} associated with those target(s). No assumptions are made about the modality/domain (e.g., text, vision) or adversarial perturbation. We do not assume access to clean validation data.

3 RELATED WORK

We mitigate training-set attacks by building upon influence estimation to identify the target(s) and adversarial set. This section first reviews existing defenses against training-set attacks and then formalizes training-set influence as defined in previous work.

3.1 Defenses Against Training-Set Attacks

Certifiably-robust defenses [28, 33, 42, 68, 74, 77, 78] provide guaranteed protection against specific training-set attacks under specific assumptions. *Empirical defenses* [17, 21, 55, 71, 85, 86] derive from understandings and observations about the underlying mechanisms training-set attacks exploit to change a network’s predictions. In practice, empirical defenses generally significantly outperform certified approaches with fewer harmful side effects – albeit without a guarantee [44]. These two defense categories are complementary and can be deployed together for better performance. Since our defense is largely empirical, we focus on that defense category below.

We are not aware of any existing defense – certified or empirical – that provides target identification. The most closely related task is determining whether a model is infected with a backdoor, which ignores poisoning and other training-set attacks [67, 80]. Such methods make different assumptions than this work. For instance, some assume access to known-clean data [17, 21, 46, 75, 86] but may not have access to the training set. Many also make assumptions about the type of attack or the training methodology [67].

Another task similar to target identification is *adversarial trigger synthesis*, which attempts to reconstruct any backdoor attack pattern(s) a model learned [21, 71, 72, 86]. These methods mitigate attacks by adding identified triggers to known-clean data so that retraining will cause catastrophic forgetting of the trigger.

Data-sanitization defenses mitigate attacks by removing adversarial set \mathcal{D}_{adv} from \mathcal{D}_{tr} . Existing data-sanitization defenses have shown promise [10, 55, 70], but they all share a common pitfall concerning setting the data-removal threshold [36, 44]. If this threshold is set too low, significant clean-data removal degrades overall clean-data performance. A threshold set too high results in insufficient adversarial training data removal and the attack remaining successful. Additional information (e.g., target identification) enables targeted tuning of this removal threshold.

Most existing certified and empirical defenses are not attack agnostic and assume specific data modalities (e.g., only vision [21, 71, 72, 86]), model architectures (e.g., CNNs [37]), optimizers [29], or training paradigms [67]. Attack agnosticism is more challenging and more practically useful. We achieve agnosticism by building upon existing methods that are general – namely influence estimation, which is formalized next.

¹Generally, there are far fewer potential targets ($\widehat{\mathcal{Z}}_{\text{te}}$) than possible test examples.

3.2 Training-Set Influence Estimation

In every successful attack, the inserted training instances change a model’s prediction for specific input(s). If the attacker can only add a limited number of instances (e.g., 1% of \mathcal{D}_{tr}), these inserted instances must be highly influential to achieve the attacker’s objective.

Influence estimation’s goal is to determine which training instances are most responsible for a model’s prediction for a particular input. Influence is often viewed as a counterfactual: which instance (or group of instances) induces the biggest change when removed from the training data? While there are multiple definitions of influence, as detailed below, influence estimation methods can be broadly viewed as quantifying the relative responsibility of each training instance $z_i \in \mathcal{D}_{\text{tr}}$ on some test prediction $f(x_{\text{te}}; \theta_T)$.

Static influence estimators consider only the final model parameters θ_T . For example, Koh and Liang’s [35] seminal work defines influence, $I_{\text{IF}}(z_i, \widehat{z}_{\text{te}})$, as the change in risk $\mathcal{L}(\widehat{z}_{\text{te}}; \theta_T)$ if $z_i \notin \mathcal{D}_{\text{tr}}$, i.e., the leave-one-out (LOO) change in test loss [14]. By assuming strict convexity and stationarity, Koh and Liang’s *influence functions* estimator approximates the LOO influence as

$$I_{\text{IF}}(z_i, \widehat{z}_{\text{te}}) \approx \frac{1}{n} \nabla_{\theta} \mathcal{L}(\widehat{z}_{\text{te}}; \theta_T)^T H_{\theta}^{-1} \nabla_{\theta} \mathcal{L}(z_i; \theta_T), \quad (1)$$

with H_{θ}^{-1} the inverse of risk Hessian $H_{\theta} := \frac{1}{n} \sum_{z_i \in \mathcal{D}_{\text{tr}}} \nabla_{\theta}^2 \mathcal{L}(z_i; \theta_T)$.

Yeh et al. [81]’s *representer point* static influence estimator exclusively considers the model’s final, linear classification layer. All other model parameters are treated as a fixed feature extractor. Given final parameters θ_T , let f_i denote x_i ’s penultimate feature representation (i.e., the *input* to the linear classification layer). Then the representer point influence of $z_i \in \mathcal{D}_{\text{tr}}$ on \widehat{z}_{te} is

$$I_{\text{RP}}(z_i, \widehat{z}_{\text{te}}) := -\frac{1}{2\lambda n} \left(\frac{\partial \mathcal{L}(z_i; \theta_T)}{\partial a_{y_i}} \right) \langle f_i, f_{\text{te}} \rangle, \quad (2)$$

where $\lambda > 0$ is the weight decay (L_2) regularizer and $\langle \cdot, \cdot \rangle$ denotes vector dot product. Recall that a is the *output* of the model’s linear classification layer, specifically here $a = f(x_i; \theta_T)$. Scalar $\frac{\partial \mathcal{L}(z_i; \theta_T)}{\partial a_{y_i}}$ is then the partial derivative of risk \mathcal{L} w.r.t. a ’s y_i -th dimension.

Dynamic influence estimators measure influence based on how losses change during training. More formally, influence is quantified according to how batches $\mathcal{B}_1, \dots, \mathcal{B}_T$ affect model parameters $\theta_0, \dots, \theta_T$ and by consequence risks $\mathcal{L}(\cdot; \theta_0), \dots, \mathcal{L}(\cdot; \theta_T)$. For example, Pruthi et al.’s [57] *TracIn* estimates influence by “tracing” gradient descent – aggregating changes in \widehat{z}_{te} ’s test loss each time training instance z_i ’s gradient updates parameters θ_t . For stochastic gradient descent (batch size $b = 1$), z_i ’s TracIn influence on \widehat{z}_{te} is

$$I_{\text{TracIn}}(z_i, \widehat{z}_{\text{te}}) := \sum_{t=1}^T \mathbb{1}_{z_i \in \mathcal{B}_t} (\mathcal{L}(\widehat{z}_{\text{te}}; \theta_{t-1}) - \mathcal{L}(\widehat{z}_{\text{te}}; \theta_t)), \quad (3)$$

where $\mathbb{1}_u$ is the indicator function s.t. $\mathbb{1}_u = 1$ if predicate u is true and 0 otherwise. Pruthi et al. approximate Eq. (3) as,

$$I_{\text{TracIn}}(z_i, \widehat{z}_{\text{te}}) \approx \sum_{z_i \in \mathcal{B}_t} \frac{\eta_t}{b} \left(\nabla_{\theta} \mathcal{L}(z_i; \theta_{t-1}), \nabla_{\theta} \mathcal{L}(\widehat{z}_{\text{te}}; \theta_{t-1}) \right), \quad (4)$$

where η_t is iteration t ’s learning rate.

Alg. 1 details the minimal changes made to model training to support TracIn where $\mathcal{T} \subset \{1, \dots, T\}$ is a preselected *training iteration subset* and $\mathcal{P} := \{(\eta_t, \theta_{t-1}) : t \in \mathcal{T}\}$ contains the *serialized training parameters*. Alg. 5² outlines TracIn’s influence estimation procedure for *a priori* unknown test instance \widehat{z}_{te} . Influence vector \mathbf{v} ($|\mathbf{v}| = n$) contains the TracIn influence estimates for each $z_i \in \mathcal{D}_{\text{tr}}$.

²Due to space, Alg. 1 appears in the supplement.

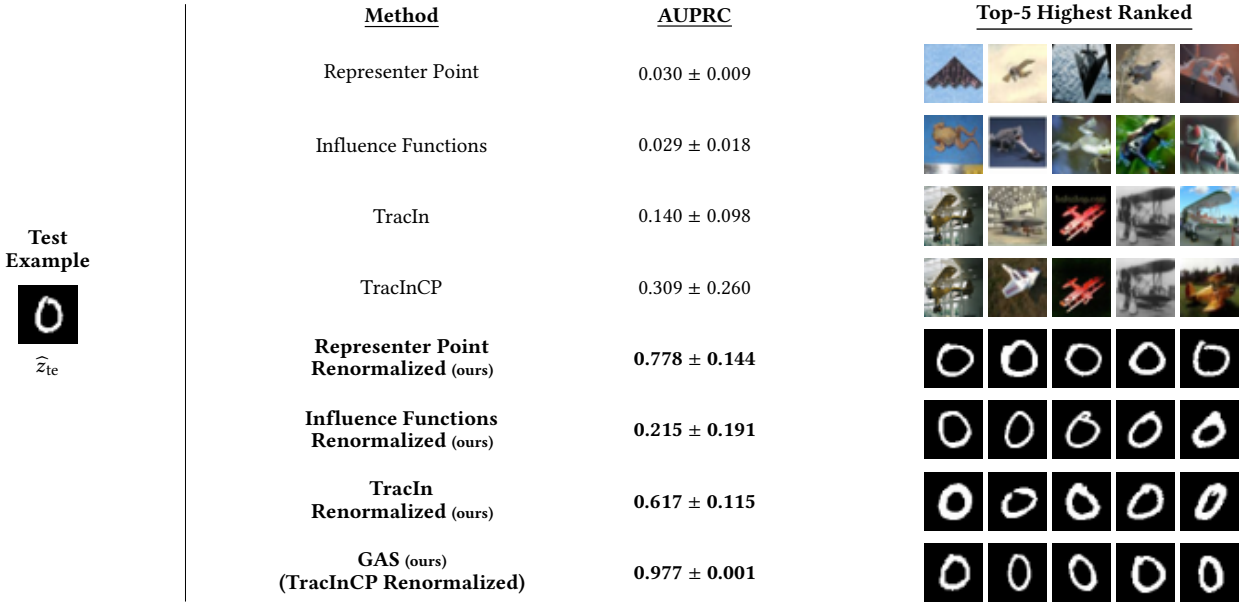


Figure 1: Renormalized Influence: CIFAR10 & MNIST joint, binary classification for [frog] vs. [airplane & MNIST 0] with $|\mathcal{D}_{cl}| = 10,000$ & $|\mathcal{D}_{adv}| = 150$. Existing influence estimators (upper half) consistently failed to rank \mathcal{D}_{adv} 's MNIST training instances as highly influential on MNIST test instances. In contrast, all of our renormalized influence estimators (Section 4.3) outperformed their unnormalized version – with AUPRC improving up to 25×. Results averaged across 30 trials.

Algorithm 1 TracIn, TracInCP, & GAS training phase

Input: Training set \mathcal{D}_{tr} , iteration subset \mathcal{T} , iteration count T , learning rates η_1, \dots, η_T , and initial parameters θ_0
Output: Training parameters \mathcal{P}

- 1: $\mathcal{P} \leftarrow \emptyset$
- 2: **for** $t \leftarrow 1$ to T **do**
- 3: **if** $t \in \mathcal{T}$ **then**
- 4: $\mathcal{P} \leftarrow \mathcal{P} \cup \{(\eta_t, \theta_{t-1})\}$
- 5: $\mathcal{B}_t \sim \mathcal{D}_{tr}$
- 6: $\theta_t \leftarrow \text{UPDATE}(\eta_t, \theta_{t-1}, \mathcal{B}_t)$
- 7: **return** \mathcal{P}

In practice, $|\mathcal{T}| \ll T$, and \mathcal{T} is evenly-spaced in $\{1, \dots, T\}$, meaning TracIn effectively treats multiple batches like a single model update.

Pruthi et al. also propose *TracIn Checkpoint* (TracInCP) – a more heuristic version of TracIn that considers *all* training examples at each checkpoint in \mathcal{T} – not just those instances in the intervening batches (see Alg. 2).³ Formally,

$$\mathcal{I}_{\text{TracInCP}}(z_i, \hat{z}_{te}) := \sum_{t \in \mathcal{T}} \frac{\eta_t}{b} \left\langle \nabla_{\theta} \mathcal{L}(z_i; \theta_{t-1}), \nabla_{\theta} \mathcal{L}(\hat{z}_{te}; \theta_{t-1}) \right\rangle. \quad (5)$$

TracInCP is more computationally expensive than TracIn – with the slowdown linear w.r.t. the number of checkpoints per epoch.

A major advantage of TracIn and TracInCP over other estimators (e.g., influence functions) is that their only hyperparameter is iteration set \mathcal{T} , which we tuned based only on compute availability.

³Algorithm 2 combines two different methods TracInCP as well as GAS – our renormalized version of TracInCP discussed in Sec. 4.3.

4 WHY INFLUENCE ESTIMATION OFTEN FAILS AND HOW TO FIX IT

Before addressing target identification, we first consider the related task of adversarial-instance identification. In the simplest case, if the attack’s target is known, then the malicious instances should be among the most influential instances for that target instance. In other words, *adversarial-instance identification reduces to influence estimation*. However, Sec. 3.2’s influence estimators share a common weakness that makes them poorly suited for this task: they all consistently rank confidently-predicted training instances as uninfluential. We illustrate this behavior below using a toy experiment. We then explain this weakness’s cause and propose a simple fix that addresses this limitation on adversarial and non-adversarial data, for all preceding estimators. Our fix is needed to successfully identify adversarial set \mathcal{D}_{adv} and, as detailed in Sec. 5, attack targets.

4.1 A Simple Experiment

Consider binary classification where clean set \mathcal{D}_{cl} is all frog and airplane training images in CIFAR10 ($|\mathcal{D}_{cl}| = 10,000$). To simulate a naive backdoor attack, adversarial set \mathcal{D}_{adv} is 150 randomly selected MNIST 0 images labeled as airplane.

Clean data’s overall influence can be estimated indirectly by training only on \mathcal{D}_{cl} and observing the target set’s misclassification rate [18]. This experiment used class pair frog and airplane because amongst the $\binom{10}{2}$ CIFAR10 class pairs, frog vs. airplane’s average MNIST test misclassification rate was closest to random (47.5% vs. 50% ideal). In contrast, when training on $\mathcal{D}_{tr} := \mathcal{D}_{adv} \sqcup \mathcal{D}_{cl}$, MNIST 0 test instances were always classified as airplane, meaning \mathcal{D}_{adv} is overwhelmingly influential on MNIST predictions. MNIST

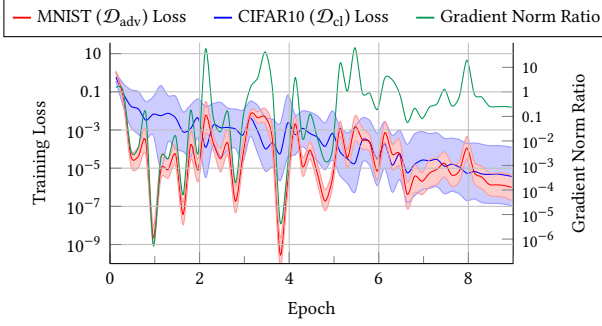


Figure 2: CIFAR10 & MNIST Intra-training Loss Tracking: \mathcal{D}_{adv} 's (—) & \mathcal{D}_{cl} 's (—) median cross-entropy losses (ℓ) at each training checkpoint for binary classification – frog vs. airplane & MNIST 0. The shaded regions correspond to each training set loss's interquartile range. MNIST's training losses are generally several orders of magnitude smaller than CIFAR10's losses. Gradient norm ratio (—) shows the tight coupling of loss & training gradient magnitude.

is used instead of other CIFAR10 classes because the large (and simple [65]) difference between the data distributions leads to a strong signal that can be consistently learned from relatively few examples – much like backdoor or poisoning attacks [82].

We use this simple setup to evaluate different influence estimation methods. We trained 30 randomly-initialized state-of-the-art ResNet9 networks, and on each network, we performed influence estimation for a random MNIST 0 test instance to determine how well each estimator identified adversarial set \mathcal{D}_{adv} provided a known target.⁴ Given the large imbalance between the amount of clean and “adversarial” data, i.e., $|\mathcal{D}_{\text{adv}}| \ll |\mathcal{D}_{\text{cl}}|$, performance is measured using area under the precision-recall curve (AUPRC), which quantifies how well \mathcal{D}_{adv} 's influence ranks relative to \mathcal{D}_{cl} . Precision-recall curves are preferred for highly-skewed classification tasks since they provide more insight into the false-positive rate [16].

Figure 1's upper half shows how well each influence estimator in Section 3.2 identifies \mathcal{D}_{adv} , both quantitatively and qualitatively. Dynamic estimators significantly outperformed their static counterparts, with TracInCP the overall top performer. However, no influence estimator consistently ranked MNIST instances (i.e., \mathcal{D}_{adv}) in the top-5 most influential, with influence functions marking instances from the other class (frog) as most influential. Influence estimation's poor performance here is particularly noteworthy as the task was designed to be unrealistically easy.

4.2 Why Influence Estimation Performs Poorly

Intra-training dynamics illuminate the primary cause of influence estimation's poor performance in our toy experiment. Fig. 2 visualizes the median training loss of \mathcal{D}_{adv} and \mathcal{D}_{cl} at each training checkpoint. Also shown is the *gradient norm ratio*, which compares the median gradient magnitude of the adversarial and clean sets at each iteration, or formally

$$\text{GNR}_t := \frac{\text{med}\{\|\mathcal{L}(z; \theta_t)\| : z \in \mathcal{D}_{\text{adv}}\}}{\text{med}\{\|\mathcal{L}(z; \theta_t)\| : z \in \mathcal{D}_{\text{cl}}\}}. \quad (6)$$

⁴See supplemental Section C for the complete experimental setup details.

The gradient norm ratio closely tracks both training sets' loss values. Both during and at the end of training, \mathcal{D}_{adv} 's *median loss* is significantly smaller than many instances in \mathcal{D}_{cl} – often by several orders of magnitude.

The Low-Loss Penalty. Observe that all influence methods in Sec. 3.2's scale their influence estimates by $\frac{\partial \ell(a, y)}{\partial a}$ either directly (representer point (2)) or indirectly via the *chain rule* (influence functions (1), TracIn (4), and TracInCP (5)) as

$$\nabla_{\theta} \mathcal{L}(z; \theta) := \frac{\partial \ell(f(x), y)}{\partial \theta} = \frac{\partial \ell(a, y)}{\partial a} \cdot \frac{\partial a}{\partial \theta}. \quad (7)$$

Therefore, gradient-based influence estimators *implicitly penalizes all training instances t with low training loss*, including \mathcal{D}_{adv} (MNIST 0) in our toy experiment above.

Theorem 4.1 summarizes this relationship when there is a single output activation ($|a| = 1$), e.g., binary classification and univariate regression. In short, when Theorem 4.1's conditions are met, loss induces a perfect ordering on the corresponding norm.

THEOREM 4.1. Let loss function $\tilde{\ell} : \mathbb{R} \rightarrow \mathbb{R}_{\geq 0}$ be twice-differentiable and strictly convex as well as either even⁵ or monotonically decreasing. Then, it holds that

$$\tilde{\ell}(a) < \tilde{\ell}(a') \implies \|\nabla_a \tilde{\ell}(a)\|_2 < \|\nabla_a \tilde{\ell}(a')\|_2. \quad (8)$$

Loss functions satisfying Theorem 4.1's conditions include binary cross-entropy (i.e., logistic) and quadratic losses. Theorem 4.1 generally applies to multiclass losses, but there are cases where the ordering is not perfect. Although Theorem 4.1 primarily relates to training instance gradients and losses, the theorem applies to test examples as well since dynamic estimators also apply a low-loss penalty to any iteration where test instance \hat{z}_{te} has low loss.

The preceding should *not* be interpreted to imply that large gradient magnitudes are unimportant. Quite the opposite, large gradients have large influences on the model. However, the approximations necessary to make influence estimation tractable go too far by often focusing almost exclusively on training loss – and by extension gradient magnitude – leading these estimators to systematically overlook training instances with smaller gradients. This overemphasis of instances with large losses and gradient magnitudes can also be viewed as a bias towards instances that are globally influential – affecting many examples' predictions – over those that are locally influential – mainly affecting a small number of targets [4].

Static Influence & the Low Loss Penalty: Fig. 1's static estimators (representer point & influence functions) significantly underperformed dynamic estimators (TracIn & TracInCP) by up to an order of magnitude. Static estimators only consider final model parameters θ_T , meaning they may only see the low-loss case. In contrast, dynamic estimators consider all of training, in particular iterations where \mathcal{D}_{adv} 's loss exceeds that of \mathcal{D}_{cl} . This allows dynamic estimators to outperform static methods, albeit still poorly.

Training Randomness & the Low-Loss Penalty: TracInCP significantly outperformed TracIn in Fig. 1 despite the TracIn being more theoretically sound. As intuition why, imagine the training set contains two identical copies of some instance. In expectation, these duplicates have equivalent influence on any test instance. However, TracIn assigns identical training examples different influence

⁵“Even” denotes that the function satisfies $\forall_a \tilde{\ell}(a) = \tilde{\ell}(-a)$.

estimates based on their batch assignments; this difference can potentially be very large depending on training dynamics.

Fig. 2 exhibits this behavior where training loss fluctuates considerably intra-epoch. For example, \mathcal{D}_{adv} 's median loss varies by seven orders of magnitude across the third epoch. TracIn's low-loss penalty attributes much more influence to \mathcal{D}_{adv} instances early in that epoch compared to those later despite all MNIST instances having similar influence. By considering all examples at each checkpoint, TracInCP removes batch randomization's direct effect on influence estimation,⁶ meaning TracInCP simulates *influence expectation* without needing to train and analyze multiple models.

4.3 Renormalizing Influence Estimation

Our CIFAR10 & MNIST joint classification experiment above demonstrates that a training example having low loss does *not* imply that it and related instances are uninfluential. Most importantly in the context of adversarial attacks, highly-related groups of (adversarial) training instances may collectively cause those group members' to have very low training losses – so-called *group effects*. Generally, targeted attacks succeed by leveraging the group effect of adversarial set \mathcal{D}_{adv} on the target(s). We address these group effects via *renormalization*, which is defined below.

Definition 4.2. For influence estimator \mathcal{I} , the *renormalized influence*, $\tilde{\mathcal{I}}$, replaces each gradient g in \mathcal{I} by its corresponding unit vector $\frac{g}{\|g\|}$.

We refer to this computation as renormalization since rescaling gradients removes the low-loss penalty. Renormalization places all training instances on equal footing and ensures that gradient and/or feature similarity is prioritized – not loss.

Renormalization is related to the relative influence (RelatIF) method introduced by Barshan et al. [4], since both methods use a function of the gradient to downweight training instances with high losses. However, RelatIF only applies to influence functions and requires computing expensive Hessian-vector products, while renormalization is more efficient and can be applied to many influence estimators, as we show below. See suppl. Section F.7 for additional discussion of alternative renormalization schemes.

Renormalized versions of Section 3.2's static influence estimators are below. *Renormalized influence functions* in Eq. (9) does not include target gradient norm $\|\hat{g}_{\text{te}}\|$ since it is a constant factor. For simplicity, Eq. (10)'s *renormalized representer point* uses signum function $\text{sgn}(\cdot)$ since for any scalar $u \neq 0$, $\text{sgn}(u) = \frac{u}{|u|}$, i.e., signum is equivalent to normalizing by magnitude.

$$\tilde{\mathcal{I}}_{\text{IF}}(z_i, \hat{z}_{\text{te}}) := \frac{1}{n} \nabla_{\theta} \mathcal{L}(\hat{z}_{\text{te}}; \theta_T)^{\top} H_{\theta}^{-1} \left(\frac{\nabla_{\theta} \mathcal{L}(z_i; \theta_T)}{\|\nabla_{\theta} \mathcal{L}(z_i; \theta_T)\|} \right) \quad (9)$$

$$\tilde{\mathcal{I}}_{\text{RP}}(z_i, \hat{z}_{\text{te}}) := -\frac{1}{2\lambda n} \text{sgn} \left(\frac{\partial \mathcal{L}(z_i; \theta_T)}{\partial a_{y_i}} \right) \langle f_i, f_{\text{te}} \rangle \quad (10)$$

Renormalized versions of Section 3.2's dynamic influence estimators appear below. Going forward, we refer to renormalized TracInCP (Eq. (12)) as *gradient aggregated similarity*, GAS, since it is essentially the weighted, gradient cosine similarity averaged

⁶Batch randomization still indirectly affects TracInCP and GAS (Sec. 4.3) through the model parameters. This effect could be mitigated by training multiple models and averaging the (renormalized) influence, but that is beyond the scope of this work.

Algorithm 2 GAS vs. TracInCP

Input: Training params. \mathcal{P} , training set \mathcal{D}_{tr} , batch size b , & test ex. \hat{z}_{te}
Output: (Renormalized) influence vector \mathbf{v}

```

1:  $\mathbf{v} \leftarrow \vec{0}$                                 ▷ Initialize
2: for each  $(\eta_t, \theta_{t-1}) \in \mathcal{P}$  do
3:    $\hat{g}_{\text{te}} \leftarrow \nabla_{\theta} \mathcal{L}(\hat{z}_{\text{te}}; \theta_{t-1})$ 
4:   for each  $z_i \in \mathcal{D}_{\text{tr}}$  do                  ▷ All examples
5:      $g_i \leftarrow \nabla_{\theta} \mathcal{L}(z_i; \theta_{t-1})$ 
6:     if calculating TracInCP then
7:        $\mathbf{v}_i \leftarrow \mathbf{v}_i + \frac{\eta_t}{b} \langle g_i, \hat{g}_{\text{te}} \rangle$       ▷ Unnormalized (Sec. 3.2)
8:     else if calculating GAS then
9:        $\mathbf{v}_i \leftarrow \mathbf{v}_i + \frac{\eta_t}{b} \left\langle \frac{g_i}{\|g_i\|}, \frac{\hat{g}_{\text{te}}}{\|\hat{g}_{\text{te}}\|} \right\rangle$     ▷ Renormalized (Sec. 4.3)
10:   return  $\mathbf{v}$ 

```

across all of training. GAS's procedure is detailed in Algorithm 2.⁷

$$\tilde{\mathcal{I}}_{\text{TracIn}}(z_i, \hat{z}_{\text{te}}) := \sum_{z_j \in \mathcal{B}_t} \frac{\eta_t}{b} \frac{\langle \nabla_{\theta} \mathcal{L}(z_i; \theta_{t-1}), \nabla_{\theta} \mathcal{L}(\hat{z}_{\text{te}}; \theta_{t-1}) \rangle}{\|\nabla_{\theta} \mathcal{L}(z_i; \theta_{t-1})\| \|\nabla_{\theta} \mathcal{L}(\hat{z}_{\text{te}}; \theta_{t-1})\|} \quad (11)$$

$$\begin{aligned} \tilde{\mathcal{I}}_{\text{TracInCP}}(z_i, \hat{z}_{\text{te}}) &:= \sum_{t \in \mathcal{T}} \frac{\eta_t}{b} \frac{\langle \nabla_{\theta} \mathcal{L}(z_i; \theta_{t-1}), \nabla_{\theta} \mathcal{L}(\hat{z}_{\text{te}}; \theta_{t-1}) \rangle}{\|\nabla_{\theta} \mathcal{L}(z_i; \theta_{t-1})\| \|\nabla_{\theta} \mathcal{L}(\hat{z}_{\text{te}}; \theta_{t-1})\|} \\ &=: \text{GAS}(z_i, \hat{z}_{\text{te}}) \end{aligned} \quad (12)$$

Unlike static estimators, rescaling dynamic influence by target gradient norm $\|\hat{g}_{\text{te}}\|$ is quite important as mentioned earlier. Intuitively, $\|\hat{z}_{\text{te}}\|$ tends to be largest in two cases: (1) early in training due to initial parameter randomness and (2) when iteration t 's predicted label conflicts with final label \hat{y}_{te} . Both cases are consistent with the features most responsible for predicting \hat{y}_{te} not yet dominating. Therefore, rescaling dynamic influence by $\|\hat{g}_{\text{te}}\|$ implicitly upweights iterations where \hat{y}_{te} is predicted confidently. It also inhibits any single checkpoint dominating the estimate.

Applying Renormalization to CIFAR10 & MNIST Joint Classification: Figure 1's lower half demonstrates renormalization's significant performance advantage over standard influence estimation – with the improvement in AUPRC as large as 25×. In particular, our renormalized estimators' top-5 highest-ranked instances were all consistently from MNIST, unlike any of the standard influence estimators. Overall, GAS (renormalized TracInCP) was the top performer – even outperforming our other renormalized estimators by a wide margin.

4.4 Renormalization & More Advanced Attacks

Section 4.2 illustrates why influence performs poorly under a naive backdoor-style attack where the adversary does not optimize the adversarial set. Those concepts also generalize to more sophisticated attacks. For example, recent work shows that deep networks often predict the adversarial set with especially high confidence (i.e., low loss) due to *shortcut learning* – even on advanced attacks [23, 82]. Those findings reinforce the need for renormalization. This can be viewed through the lens of *simplicity bias* where neural networks tend to confidently learn simple features (shortcuts) – regardless of whether those features actually generalize [65].

⁷As shown in Algorithm 2, TracInCP's procedure (Line 7) is identical to GAS (Line 9) other than influence renormalization.

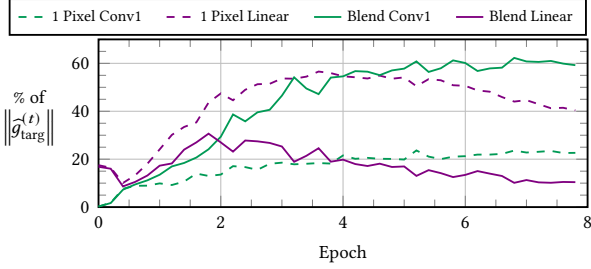


Figure 3: Layerwise Decomposition of an Attack Target’s Intra-Training Gradient Magnitude: One-pixel & blend backdoor adversarial triggers (dashed & solid lines respectively) trained separately on CIFAR10 binary classification ($y_{\text{targ}} = \text{airplane}$ & $y_{\text{adv}} = \text{bird}$) using ResNet9. The network’s first convolutional (Conv1) and final linear layers are a small fraction of the parameters (0.03% & 0.01% resp.) but constitute most of the target’s gradient magnitude ($\|\hat{g}_{\text{targ}}\|$) with the dominant layer attack dependent. Results are averaged over 20 trials.

Dynamic estimators – both TracIn and GAS – outperform static ones for Sec. 4.1’s naive attack. The same can be expected for sophisticated attacks including ones that track adversarial-set gradients through simulated training [31, 73]. For those attacks, adversaries can craft \mathcal{D}_{adv} to exhibit particular gradient signatures at the end of training to avoid static detection. Moreover, models learn adversarial data faster than clean data meaning training loss often drops abruptly and significantly early in training [43]. For an attack to succeed, adversarial instances must align with the target at some point during training, meaning dynamic methods can detect them.

Lastly, our threat model specifies that attackers never know the random batch sequence nor any randomly initialized parameters. Therefore, attackers can only craft \mathcal{D}_{adv} to be *influential in expectation* over that randomness. Influence is stochastic, varying significantly across random seeds. However, estimating the true expected influence is computationally expensive. GAS and TracInCP, which simulate expectation, better align with how the adversary actually crafts the adversarial set, resulting in better \mathcal{D}_{adv} identification.

Below we detail how renormalization can be specialized further for better adversarial-set identification.

Extending Renormalization Layerwise: In practice, gradient magnitudes are often unevenly distributed across a neural network’s layers. For example, Figure 3 tracks an attack target’s average intra-training gradient magnitude for two different backdoor adversarial triggers on CIFAR10 binary classification ($y_{\text{targ}} = \text{airplane}$ and $y_{\text{adv}} = \text{bird}$).⁸ Specifically, target gradient norm, $\|\nabla_{\theta} \mathcal{L}(\hat{z}_{\text{targ}}; \theta_t)\|$, is decomposed into just the contributions of the network’s first convolutional layer (Conv1) and the final linear layer. Despite being only 0.04% of the model parameters, these two layers combined constitute >50% of the gradient norm. Therefore, the first and last layers’ parameters are, on average, weighted >2,000× more than

⁸See supplemental Section C for the complete experimental setup. The class pair and adversarial triggers were proposed by Weber et al. [78].

other layers’ parameters. With simple renormalization, important parameters in those other layers may go undetected.

As an alternative to simply renormalizing by $\|\nabla_{\theta} \mathcal{L}(z; \theta_t)\|$, partition gradient vector g by layer into L disjoint vectors (where L is model f ’s layer count) and then independently renormalize each subvector separately. This *layerwise renormalization* can be applied to any estimator that uses training gradient g_i or test gradient \hat{g}_{te} , including influence functions, TracIn, and TracInCP. Layerwise renormalization still corrects for the low-loss penalty and does not change the asymptotic complexity. To switch GAS to layerwise, the only modification to Algorithm 2 is on Line 10 where each dimension is divided by its corresponding layer’s norm instead of the full gradient norm.

Notation: “-L” denotes layerwise renormalization, e.g., *layerwise GAS* is GAS-L. Suffix “(-L)”, e.g., GAS(-L), signifies that a statement applies irrespective of whether the renormalization is layerwise.

4.5 Renormalization & Non-Adversarial Data

Renormalization not only improves performance identifying an inserted adversarial set; it also improves performance in *non-adversarial* settings. Sec. 3.2 defines influence w.r.t. a single training example. Just as one instance may be more influential on a prediction than another, a group of training instances may be more influential than a different group. Renormalization improves identification of influential groups of examples, even on non-adversarial data.

To empirically demonstrate this, consider CIFAR10 binary classification again. In each trial, ResNet9 was pre-trained on eight ($= 10 - 2$) held-out CIFAR10 classes. From the other two classes, test example z_{fil} was selected u.a.r. from those test instances with a moderate misclassification rate (10–20%) across multiple retrainings (i.e., fine-tunings) of the pre-trained network.⁹ (Renormalized) influence was then calculated for z_{fil} , with each estimator yielding a training-set ranking. Each estimator’s top $p\%$ ranked instances were removed from the training set and 20 models trained from the pre-trained parameters using these reduced training sets. Performance is measured using z_{fil} ’s misclassification rate across those 20 models where a larger error rate entails a better overall ranking.

Figure 4 compares influence estimation’s filtering performance, with and without renormalization, against a random baseline averaged across five CIFAR10 class pairs, namely the two pairs specified by Weber et al. [78] and three additional random pairs. Influence, irrespective of renormalization, significantly outperformed random removal, meaning all of these estimators found influential subsets, albeit of varying quality.¹⁰ In all cases, renormalized influence had better or equivalent performance to the original estimator across all filtering fractions. This demonstrates that renormalization generalizes across estimators even beyond adversarial settings.

Overall, layerwise renormalization was the top performer across all setups except for large filtering percentages where GAS surpassed it slightly. Renormalized(-L) Influence functions and GAS(-L) performed similarly when filtering a small fraction (e.g., $\leq 5\%$) of the training data. However, the performance of renormalized influence functions plateaued for larger filtering fractions ($\geq 10\%$) while

⁹Using examples with a moderate misclassification rate ensures that dataset filtering’s effects are measurable even with a small fraction of the training data removed.

¹⁰Representer point (Eq. (2)) is excluded as it underperformed random filtering.

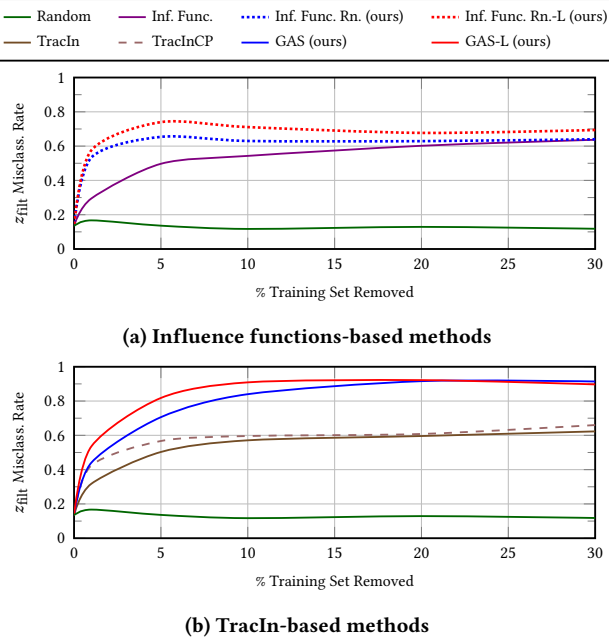


Figure 4: Effect of Removing Influential, Non-Adversarial Training Data: Test example z_{filt} 's misclassification rate (larger is better) when filtering the training set using influence rankings based on influence functions (top) and TracIn (bottom). Renormalization (Rn.) always improved mean performance across all training-set filtering percentages. Results are averaged across five CIFAR10 class pairs with 30 trials per class pair and 20 models trained per method per trial. Results are separated by the reference influence estimator.

GAS(-L)'s performance continued to improve. In addition, renormalization's performance advantage over vanilla influence functions narrowed at larger filtering fractions. In contrast, GAS(-L)'s advantage over TracIn and TracInCP remained consistent. Recall that dynamic methods (e.g., GAS(-L) and TracIn) use significantly more gradient information than static methods (e.g., influence functions). This experiment again demonstrates that loss-based renormalization's benefits increase as more gradient information is used.

5 IDENTIFYING ATTACK TARGETS

Recall that non-targets have primarily weak influences and few very strong ones. Target instances are anomalous in that they have an unusual number of highly-influential training instances (Figure 5). This idea is the core of our *framework for identifying targets* of training-set attacks, FIT. Alg. 3 formalizes FIT as an end-to-end procedure to identify any targets in test example analysis set $\tilde{\mathcal{Z}}_{\text{te}}$.¹¹ Overall, FIT has three sub-steps, described chronologically:

- (1) INF: Calculates (renormalized) influence vector \mathbf{v} for each test instance in analysis set $\tilde{\mathcal{Z}}_{\text{te}}$.
- (2) ANOMSCORE: Targets have an unusual number of highly-influential instances. Leveraging ideas from anomaly detection, this step

¹¹For simplicity, Alg. 3 considers a single identified target. If there are multiple identified targets, MITIGATE is invoked on each target serially with parameters θ_T and $\tilde{\mathcal{D}}_{\text{tr}}$.

Algorithm 3 FIT target identification & mitigation

Input: Training set \mathcal{D}_{tr} , test example set $\tilde{\mathcal{Z}}_{\text{te}}$, and final params. θ_T
Output: Sanitized model parameters $\bar{\theta}_T$ & training set $\tilde{\mathcal{D}}_{\text{tr}}$

- 1: $\mathcal{V} \leftarrow \{\text{INF}(\hat{z}; \mathcal{D}_{\text{tr}}) : \hat{z} \in \tilde{\mathcal{Z}}_{\text{te}}\}$ ▷ (Renorm.) Inf. (Alg. 2)
- 2: $\Sigma \leftarrow \{\text{ANOMSCORE}(\mathbf{v}, \mathcal{V}) : \mathbf{v} \in \mathcal{V}\}$ ▷ Anomaly score (Sec. 5.2)
- 3: Rank $\tilde{\mathcal{Z}}_{\text{te}}$ by anomaly scores Σ
- 4: $\hat{z}_{\text{targ}} \leftarrow$ Most anomalous test example in $\tilde{\mathcal{Z}}_{\text{te}}$
- 5: $\bar{\theta}_T, \tilde{\mathcal{D}}_{\text{tr}} \leftarrow \text{MITIGATE}(\hat{z}_{\text{targ}}, \theta_T, \mathcal{D}_{\text{tr}})$ ▷ Sec. 5.3
- 6: **return** $\bar{\theta}_T, \tilde{\mathcal{D}}_{\text{tr}}$

analyzes each test instance's influence vector \mathbf{v} and ranks those instances based on how anomalous their influence values are.

- (3) **MITIGATE:** Target-driven mitigation sanitizes model parameters θ_T and training set \mathcal{D}_{tr} to remove the attack's influence on the most likely target \hat{z}_{targ} (e.g., the most anomalous misclassified instance).

FIT is referred to as a “framework” since these subroutines are general and their underlying algorithms can change as new versions are developed. The next three subsections describe our implementation of each of these methods. For reference, suppl. Alg. 6 specializes Alg. 3 to more closely align with the implementation details below. Suppl. Sec. A.1 details FIT's end-to-end computational complexity.

5.1 Measuring (Renormalized) Influence

Algorithm 3 is agnostic of the specific (renormalized) influence estimator used to calculate \mathbf{v} , provided that method is sufficiently adept at identifying adversarial set \mathcal{D}_{adv} . We use GAS(-L) for the reasons explained in Section 4 as well as its simplicity, computational efficiency, and strong, consistent empirical performance.

Time and Space Complexity: Computing a gradient requires $\mathcal{O}(|\theta|)$ time and space. For fixed T and $|\theta|$, TracInCP, GAS, and GAS-L require $\mathcal{O}(n)$ time and space to calculate each test instance's influence vector \mathbf{v} . The next section explains that FIT analyzes each test instance's influence vector \mathbf{v} meaning GAS(-L) can be significantly sped-up by amortizing training gradient ($g_i^{(t)}$) computation across multiple test examples – either on a single node (suppl. Sec. F.10) or across multiple nodes (e.g., using all-reduce).

5.2 Identifying Anomalous Influence

To change a prediction, adversarial set \mathcal{D}_{adv} must be highly influential on the target. When visualizing \hat{z}_{te} 's influence vector \mathbf{v} as a density distribution, an exceptionally influential \mathcal{D}_{adv} manifests as a distinct density mass at the distribution's positive extreme.

Figures 5a and 5d each plot an attack target's GAS influence as a density for two different training-set attacks – the first poisoning on vision [84] and the other a backdoor attack on speech recognition [47]. For both attacks, adversarial set \mathcal{D}_{adv} 's influence significantly exceeds that of \mathcal{D}_{cl} . When compared to theoretical normal (calculated¹² w.r.t. complete training set \mathcal{D}_{tr}), \mathcal{D}_{adv} 's target influence is highly anomalous. In Figures 5b and 5e, which plot the GAS influence of non-targets for the same two attacks, no extremely high influence instances are present.

¹²The plotted theoretical normal used robust statistics median and Q in place of mean and standard deviation.

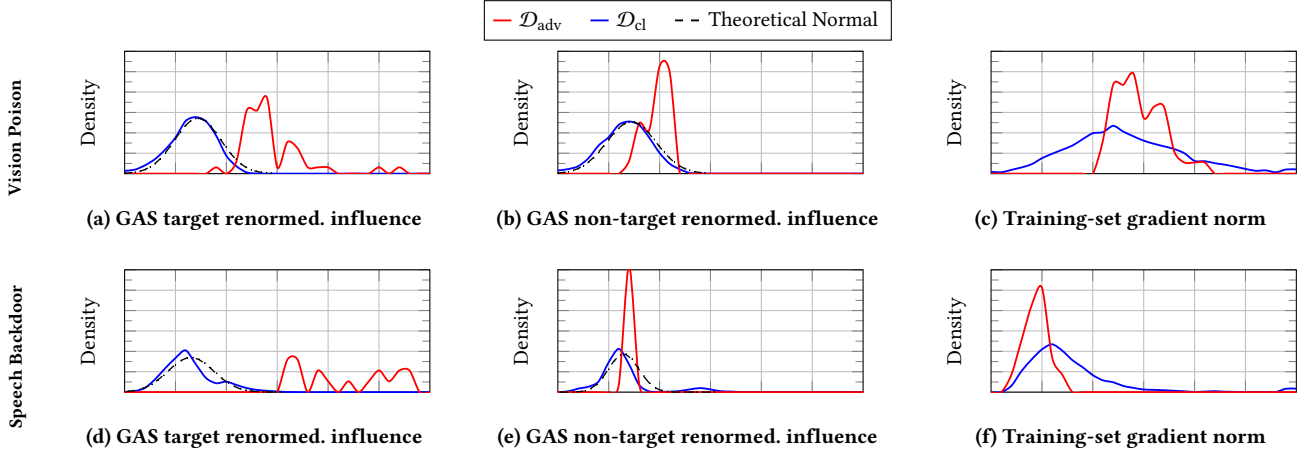


Figure 5: GAS renormalized influence, v , density distributions for two training-set attacks: CIFAR10 vision poisoning [84] ($y_{\text{targ}} = \text{dog}$ & $y_{\text{adv}} = \text{bird}$) & speech-recognition backdoor [47] ($y_{\text{targ}} = 4$ & $y_{\text{adv}} = 5$). Theoretical normal (---) is w.r.t. $\mathcal{D}_{\text{tr}} := \mathcal{D}_{\text{adv}} \cup \mathcal{D}_{\text{tr}}$. Observe that target examples (Figs. 5a & 5d) have significant \mathcal{D}_{adv} mass (—) well to the right of \mathcal{D}_{cl} 's mass (—). This upper-mass phenomenon is absent in non-targets (Figs. 5b & 5e). Training example gradient norms (Fig. 5c & 5f) are poorly correlated with whether the training example is adversarial. For example, speech recognition has \mathcal{D}_{cl} mass well to the right of even the right-most \mathcal{D}_{adv} mass, necessitating renormalization. See Sections 6.1 and C for more details on these attacks.

Going forward, influence vectors v with exceptionally high influence instances are referred to as having a *heavy upper tail*. Then, *target identification simplifies to identifying influence vectors whose values have anomalously heavy upper tails*. The preceding insight is relative and is w.r.t. to other test instances' influence value distributions. Non-target baseline anomaly quantities vary with model, dataset, and hyperparameters. That is why suppl. Algorithm 6 ranks candidates in $\hat{\mathcal{Z}}_{\text{te}}$ based on their upper-tail heaviness.

Quantifying Tail Heaviness: Determining whether \hat{z}_{te} 's influence vector v is abnormal simplifies to univariate anomaly detection for which significant previous work exists [3, 30, 60, 61]. Observe in Figures 5b and 5e that \mathcal{D}_{cl} 's GAS influence vector v tends to be normally distributed (see the close alignment to the dashed line). We, therefore, use the traditional *anomaly score*, $\sigma := \frac{v - \mu}{s}$, where μ and s are each v 's center and dispersion statistics, resp.¹³ Mean and standard deviation, the traditional center and dispersion statistics, resp., are not robust to outliers. Both have an asymptotic *breakdown point* of 0 (one anomaly can shift the estimator arbitrarily). Since \mathcal{D}_{adv} instances are inherently outliers, robust statistics are required.

Median serves as our center statistic μ given its optimal breakdown (50%). Although median absolute deviation (MAD) is the best known robust dispersion statistic, we use Rousseeuw and Croux's [59] Q estimator, which retains MAD's benefits while addressing its weaknesses. Specifically, both MAD and Q have optimal breakdowns, but Q has better Gaussian data *efficiency* (82% vs. 37%). Critically for our setting with one-sided anomalies, Q does not assume data symmetry – unlike MAD. Formally,

$$Q := c \{ |v_i - v_l| : 1 \leq i < l \leq n \}_{(r)}, \quad (13)$$

¹³In suppl. Algorithm 6, statistics $\mu^{(j)}$ and $Q^{(j)}$ are calculated separately for each test instance \hat{z}_j 's influence vector $v^{(j)}$.

where $\{\cdot\}_{(r)}$ denotes the set's r -th *order statistic* with $r = (\lfloor \frac{n}{2} \rfloor + 1)$ and c is a distribution consistency constant which for Gaussian data, $c \approx 2.2219$ [60]. Eq. (13) requires only $\mathcal{O}(n)$ space and $\mathcal{O}(n \lg n)$ time as proven by Croux and Rousseeuw [15]. Provided anomaly score vector σ , upper-tail heaviness is simply $\sigma_{(n-\kappa)}$, which is σ 's $(n - \kappa)^{\text{th}}$ order statistic, i.e., \hat{z}_{te} 's κ^{th} largest anomaly score value. The value of κ implicitly affects the size of the smallest detectable attack, where any attack with $|\mathcal{D}_{\text{adv}}| < \kappa$ is much harder to detect.

Multiclass vs. Binary Classification Different classes are implicitly generated from different data distributions. Each class's data distribution may have different influence tails – in particular in multiclass settings. Target identification performance generally improves (1) when μ and Q are calculated w.r.t. only training instances labeled \hat{y}_{te} and (2) \hat{z}_{te} 's upper-tail heaviness is ranked w.r.t. other test instances labeled \hat{y}_{te} .

Faster FIT The execution time of TracInCP and by extension GAS(-L), depends on parameter count $|\theta|$. For very large models, target identification can be significantly sped up via a two-phase strategy. In phase 1, GAS(-L) uses a very small iteration subset (e.g., $\mathcal{T} = \{\mathcal{T}\}$) to coarsely rank analysis set $\hat{\mathcal{Z}}_{\text{te}}$. Phase 2 then uses the complete \mathcal{T} but only on a small fraction (e.g., 10%) of $\hat{\mathcal{Z}}_{\text{te}}$ with the heaviest phase 1 tails. Section 6.3 applies this approach to natural-language data poisoning on RoBERTaBASE [48].

Computing each test instance's ($\hat{z}_{\text{te}} \in \hat{\mathcal{Z}}_{\text{te}}$) influence vector v is independent. Each dimension v_i is also independent and can be separately computed. Hence, GAS(-L) is embarrassingly parallel allowing linear speed-up of target identification via parallelization.

5.3 Target-Driven Attack Mitigation

A primary benefit of target identification is that attack mitigation becomes straightforward. Algorithm 4 mitigates attacks by sanitizing training set \mathcal{D}_{tr} of adversarial set \mathcal{D}_{adv} . Most importantly, target

Algorithm 4 Target-driven mitigation & sanitization

Input: Target $\tilde{z}_{\text{targ}} := (x_{\text{targ}}, y_{\text{adv}})$, anomaly cutoff ζ , model f , initial params. θ_0 , final params. θ_T , and training set \mathcal{D}_{tr}

Output: Clean model parameters $\tilde{\theta}_T$ & sanitized training set $\tilde{\mathcal{D}}_{\text{tr}}$

- 1: **function** MITIGATE(\tilde{z}_{targ} , θ_T , \mathcal{D}_{tr})
- 2: $\tilde{\theta}_T, \tilde{\mathcal{D}}_{\text{tr}} \leftarrow \theta_T, \mathcal{D}_{\text{tr}}$
- 3: **while** $\arg \max(f(x_{\text{targ}}; \tilde{\theta}_T)) = y_{\text{adv}}$ **do**
- 4: $v \leftarrow \text{INF}(\tilde{z}_{\text{targ}}; \mathcal{D}_{\text{tr}})$ ▷ Renorm. Influence (Alg. 2)
- 5: $\sigma \leftarrow \frac{v - \mu}{Q}$ ▷ Anomaly score (Sec. 5.2)
- 6: $\tilde{\mathcal{D}}_{\text{tr}} \leftarrow \tilde{\mathcal{D}}_{\text{tr}} \setminus \{z_i : \sigma_i \geq \zeta \wedge z_i \in \tilde{\mathcal{D}}_{\text{tr}}\}$ ▷ Sanitize
- 7: $\tilde{\theta}_T \leftarrow \text{RETRAIN}(\theta_0, \tilde{\mathcal{D}}_{\text{tr}})$
- 8: Optionally anneal ζ
- 9: **return** $\tilde{\theta}_T, \tilde{\mathcal{D}}_{\text{tr}}$

identification solves data sanitization’s common pitfall (Sec. 3.1) of determining how much data to remove. *Sanitization stops when the target’s misprediction is eliminated.* Therefore, successfully identifying a target means sanitization is *guaranteed to succeed tautologically* (i.e., attack success rate on any analyzed targets is 0).

More concretely, Alg. 4 iteratively filters \mathcal{D}_{tr} by thresholding anomaly score vector, σ .¹⁴ Since adversarial instances are abnormally influential on targets, Alg. 4 filters \mathcal{D}_{adv} instances first. After each iteration, influence is remeasured to account for estimation stochasticity and because training dynamics may change with different training sets. Data removal cutoff ζ is tuned based on computational constraints – larger ζ results in less clean data removed but may take more iterations. Slowly annealing ζ also results in less clean-data removal.

Given forensic or human analysis of the identified target(s), simpler mitigation than Algorithm 4 is possible, e.g., a naive, rule-based, corrective lookup table that entails no clean data removal at all.

For learning environments where *certified training data deletion* is possible [25, 49], retraining (Alg. 4 Line 7) may not even be required — making our method even more efficient.

Enhancing Mitigation’s Robustness An adversary could attack FIT by injecting adversarial instances into \mathcal{D}_{tr} to specifically trigger excessive, unnecessary sanitization. To mitigate such a risk, Alg. 4 could be tweaked to include a maximum sanitization threshold¹⁵ that would trigger additional (e.g., human, forensic) analysis. This threshold could be set empirically or using domain-specific knowledge (e.g., maximum possible poisoning rate). See supplemental Section F.4 for further discussion.

6 EVALUATION

We empirically demonstrate our method’s generality by evaluating training-set attacks on different data modalities, including text, vision, and speech recognition. We consider both poisoning and backdoor attacks on pre-trained and randomly-initialized, state-of-the-art models in binary and multiclass settings. Due to space, most evaluation setup details (e.g., hyperparameters) are deferred

¹⁴Alg. 4 considers the more general case of a single identified target but can be extended to consider multiple targets. For instance, provided there is a single attack, average v across all targets, and stop sanitizing once all targets are classified correctly.

¹⁵This threshold could be w.r.t. the number of examples removed or the change in held-out loss. These quantities can be measured cumulatively or for targets individually.

to suppl. Section C. Additional experimental results also appear in the supplement, including an analysis of a novel adversarial attack on target-driven mitigation (Sec. F.4), a poisoning-rate ablation study (Sec. F.5), a hyperparameter sensitivity study (Sec. F.6), an alternative renormalization approach (Sec. F.7), analysis of gradient aggregation’s benefits (Sec. F.8), & execution times (Sec. F.10).

6.1 Training-Set Attacks Evaluated

We evaluated our method on four published training-set attacks – two *single-target* data poisoning and two multi-target backdoor. Below are brief details regarding how each attack crafts adversarial set \mathcal{D}_{adv} , with the full details in suppl. Sec. C.2.4. Representative clean and adversarial training instances for each attack appear in suppl. Sec. E. Table 1 lists each attack’s mean *success rate* aggregated across all related setups. Full granular results are in Section F.1.

Below, $y_{\text{targ}} \rightarrow y_{\text{adv}}$ denotes the target’s true and adversarial labels, respectively. When an attack considers multiple class pairs or setups, each is evaluated separately.

(1) *Speech Backdoor*: Liu et al.’s [47] speech recognition dataset contains spectrograms of human speech pronouncing in English digits 0 to 9 (10 classes, $|\mathcal{D}_{\text{cl}}| = 3,000$ – 1% backdoors). Liu et al. also provide 300 backdoored training instances evenly split between the 10 classes. Each class’s adversarial trigger – a short burst of white noise at the recording’s beginning – induces the spoken digit to be misclassified as the next largest digit (e.g., 0 → 1, 1 → 2, etc.). This small input-space signal induces a large feature-space perturbation – too large for many certified methods. Following Liu et al., our evaluation used a speech recognition CNN trained from scratch.

(2) *Vision Backdoor*: Weber et al. [78] consider three different backdoor adversarial trigger patterns on CIFAR10 binary classification. Specifically, Weber et al.’s “pixel” attack patterns increase the pixel value of either one or four central pixel(s) by a specified maximum ℓ_2 perturbation distance while their “blend” trigger pattern adds fixed $\mathcal{N}(0, I)$ Gaussian noise across all perturbed images. We considered the same class pairs as Weber et al. (auto → dog and plane → bird) on the state-of-the-art ResNet9 [52] CNN trained from scratch with $|\mathcal{D}_{\text{adv}}| = 150$ and $|\mathcal{D}_{\text{tr}}| = 10,000$ (1.5% backdoors).

(3) *Natural Language Poison*: Wallace et al. [73] construct text-based poison by simulating bilevel optimization via second-order gradients. \mathcal{D}_{adv} ’s instances are crafted via iterative word-level substitution given a target phrase. We follow Wallace et al.’s [73] experimental setup of poisoning the Stanford Sentiment Treebank v2 (SST-2) sentiment analysis dataset [66] ($|\mathcal{D}_{\text{cl}}| = 67,349$ & $|\mathcal{D}_{\text{adv}}| = 50$ – 0.07% poison) on the RoBERTaBASE transformer architecture (125M parameters) [48].

(4) *Vision Poison*: Zhu et al.’s [84] targeted, clean-label attack crafts poisons by forming a convex polytope around a single target’s feature representation. Following Zhu et al., the pre-train then fine-tune paradigm was used. In each trial, ResNet9 was pre-trained using half the classes (none were y_{targ} or y_{adv}). Targets were selected uniformly at random (u.a.r.) from test examples labeled y_{targ} , and 50 poison instances (0.2% of \mathcal{D}_{tr}) were then crafted from seed examples labeled y_{adv} . The pre-trained network was fine-tuned using \mathcal{D}_{adv} and the five held-out classes’ training data ($|\mathcal{D}_{\text{tr}}| = 25,000$). Like previous work [31, 64], CIFAR10 class pairs dog vs. bird and

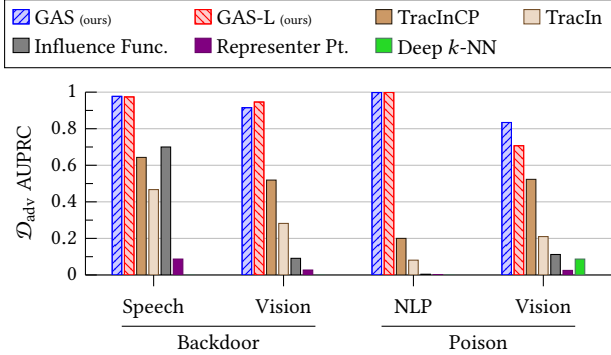


Figure 6: Adversarial-Set Identification: Mean AUPRC identifying adversarial set \mathcal{D}_{adv} using a randomly selected target for Sec. 6.1’s four attacks. Results averaged across related setups with ≥ 10 trials per setup. See supplemental Section F.1 for the full granular results, including variance.

deer vs. frog were evaluated, where each class in a pair serves alternately as y_{targ} and y_{adv} .

While it is not feasible to evaluate our approach on every attack (as new attacks are developed & published so frequently) we believe this diverse set of attacks is representative of training-set attacks in general and demonstrates our approach’s broad applicability. In particular, our method is not tailored to these attacks and could be used against future attacks as well, as long as the attack includes highly-influential training examples that attack specific targets.

6.2 Identifying Adversarial Set \mathcal{D}_{adv}

To identify the target (Alg. 3) or mitigate the attack (Alg. 4), we must be able to identify the likely adversarial instances \mathcal{D}_{adv} associated with a possible target \hat{z}_{targ} . Our approach is to use influence-estimation methods, which should rank an actual adversarial attack \mathcal{D}_{adv} as more influential than clean instances \mathcal{D}_{cl} on the target. In this section, we evaluate how well different influence-estimation methods succeed at performing this ranking for a given target.

We compare the performance of our renormalized estimators, GAS and GAS-L, against Section 3.2’s four influence estimators: TracInCP, TracIn, influence functions, and representer point. As an even stronger baseline, where applicable, we also compare against Peri et al.’s [55] Deep k -NN empirical training-set defense specifically designed for Zhu et al.’s [84]’s vision, clean-label poisoning attack; described briefly, Deep k -NN sanitizes the training set of instances whose nearest feature-space neighbors have a different label. Like Section 4’s CIFAR10 & MNIST joint classification experiment, class sizes are imbalanced ($|\mathcal{D}_{\text{adv}}| \ll |\mathcal{D}_{\text{cl}}|$) so performance is again measured using AUPRC.

For targets selected u.a.r., Figure 6 details each method’s averaged adversarial-set identification AUPRC for Section 6.1’s four attacks. In summary, GAS and GAS-L were each the top performer for one attack and had comparable performance for the other two.

GAS and GAS-L identified the adversarial instances nearly perfectly for Liu et al.’s speech backdoor and Wallace et al.’s text poisoning attacks. Standard influence estimation performed poorly on the text poisoning attack (in particular the static estimators) due to

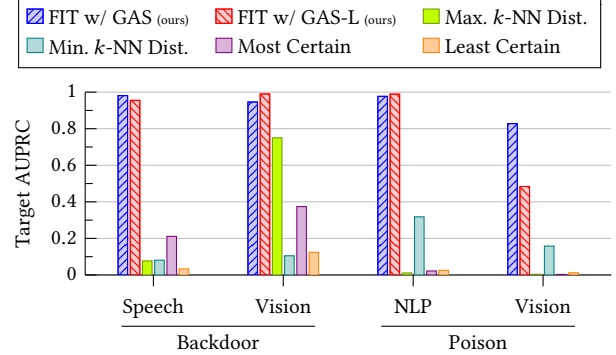


Figure 7: Target Identification: Mean target identification AUPRC for Sec. 6.1’s four attacks. “FIT w/ GAS” denotes GAS was FIT’s influence estimator with matching notation for GAS-L. Results averaged across setups with ≥ 10 trials per setup. See Sec. F.1 for the full granular results, inc. variance.

the large model, RoBERTa_{BASE}, that Wallace et al.’s attack considers. For the vision backdoor and poisoning attacks, our renormalized estimators successfully identified most of \mathcal{D}_{adv} – again, much better than the four original estimators. While Peri et al.’s [55] Deep k -NN defense can be effective at stopping clean-label vision poisoning, it does so by removing a comparatively large fraction of clean data (up to 4.3% on average) resulting in poor AUPRC.

For completeness, Figure 8 provides adversarial-set identification results for our renormalized, static influence estimators. In all cases, renormalization improved the estimator’s performance, generally by an order of magnitude with a maximum improvement of 600 \times . These experiments highlight layerwise renormalization’s benefits. Influence functions’ Hessian-vector product algorithm [54] can assign a large magnitude to some layers, and these layers then dominate the influence and GAS estimates. Layerwise renormalization addresses this, improving renormalized influence function’s adversarial-set identification AUPRC by up to 3.5 \times .

6.3 Identifying Attack Targets

The previous experiments demonstrate that knowledge of a target enables identification of the adversarial set when using renormalization. This section demonstrates that the distribution of renormalized influence values actually enables us to identify target(s) in the first place, through the interplay foundational to our target identification framework, FIT. Since target identification is a new task, we propose four target identification baselines. First, inspired by Peri et al.’s [55] Deep k -NN empirical defense, *maximum k -NN distance* computes the distance from each test instance to its k^{th} nearest neighbor in the training data, as measured by the L_2 distance between their penultimate feature representations (f). It orders them by this distance, starting with the largest distance to the k^{th} neighbor, thus prioritizing outliers and instances in sparse regions of the learned representation space. *Minimum k -NN distance* is the reverse ordering, prioritizing instances in dense regions. The other two baselines are *most certain*, which ranks test examples in ascending order by loss while *least certain* ranks by descending loss.

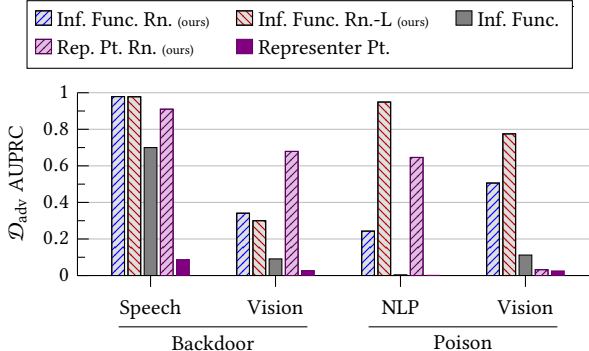


Figure 8: Static Influence Adversarial-Set Identification: Comparing the mean adversarial-set identification AUPRC of the static influence estimators and their corresponding renormalized (Rn.) versions. For all attacks, renormalization improved the static estimators’ mean performance by up to a factor of $>600\times$. These experiments also highlight layerwise renormalization’s performance gains, e.g., influence functions on natural-language poison. Results are averaged across related experimental setups with ≥ 10 trials per setup.

There are far fewer targets than possible test examples so performance is again measured using AUPRC. See suppl. Table 6 for the number of targets and non-targets analyzed for each attack. For single-target attacks (vision and natural language poisoning), target identification AUPRC is equivalent to the target’s inverse rank, causing AUPRC to decline geometrically.

Figure 7 shows that FIT – using either GAS or GAS-L as the influence estimator – achieves near-perfect target identification for both backdoor attacks and natural language poisoning. Overall, FIT with GAS was the top performer on two attacks, and FIT with GAS-L was the best for the other two. Recall that the vision poisoning attack is single target. Hence, GAS-based FIT’s mean AUPRC of >0.8 equates to an average target rank better than 1.25 (1/0.8), i.e., three out of four times on average \hat{z}_{targ} was the top-ranked – also very strong target detection. FIT’s performance degradation on vision poisoning is due to GAS and GAS-L identifying this attack’s \mathcal{D}_{adv} slightly worse (Fig. 6). Only maximum k -NN approached FIT’s performance – specifically for Weber et al.’s vision backdoor attack. Note also that no baseline consistently outperformed the others. Hence, these attacks affect network behavior differently, further supporting that FIT is attack agnostic.

Suppl. Sec. F.6 shows that FIT’s performance is stable across a wide range of upper-tail cutoff thresholds κ . For example, FIT’s natural language target identification AUPRC varied only 0.2% and 2.1% when using GAS-L and GAS respectively for $\kappa \in [1, 25]$.

6.4 Target-Driven Mitigation

Section 5.3 explains that successfully identifying the target(s) enables *guaranteed attack mitigation* on those instances. Here, we evaluate GAS and GAS-L’s effectiveness in targeted data sanitization. Table 1 details our defense’s effectiveness against Sec. 6.1’s four attacks. As above, results are averaged across each attack’s class pairs/setups. Section 6’s baselines all have large false-positive

Table 1: Target-Driven Attack Mitigation: Alg. 4’s target-driven, iterative data sanitization applied to Sec. 6.1’s four attacks for randomly selected targets. The attacks were neutralized with few clean instances removed and little change in test accuracy. Attack success rate (ASR) is w.r.t. the analyzed target. Results are averaged across related setups with ≥ 10 trials per setup. Detailed results appear in Sec. F.1.1–F.1.4.

	Dataset	Method	% Removed		ASR %		Test Acc. %	
			\mathcal{D}_{adv}	\mathcal{D}_{cl}	Orig.	Ours	Orig.	Chg.
Backdoor	Speech	GAS	98.4	0.07	99.8	0	97.7	0.0
		GAS-L	98.1	0.17	0	0	97.7	0.0
	Vision	GAS	87.6	0.50	90.5	0	96.2	-0.1
		GAS-L	92.3	0.73	0	0	96.2	-0.1
Poison	NLP	GAS	99.6	0.02	97.9	0	94.2	+0.2
		GAS-L	99.9	0.03	0	0	94.2	+0.1
	Vision	GAS	65.1	0.02	77.9	0	87.1	0.0
		GAS-L	58.6	0.03	0	0	87.1	0.0

rates when identifying \mathcal{D}_{adv} (Fig. 6), which caused them to remove a large fraction of \mathcal{D}_{cl} and are not reported in these results.

For three of four attacks, clean test accuracy after sanitization either improved or stayed the same. In the case of Weber et al.’s vision backdoor attack, the performance degradation was very small – 0.1%. Similarly, owing to renormalized influence’s effectiveness identifying \mathcal{D}_{adv} (Fig. 7), our defense removes very little clean data when mitigating the attack – generally $<0.2\%$ of the clean training set. For comparison, Peri et al. [55] report that their Deep k -NN clean-label, poisoning defense removes on average 4.3% of \mathcal{D}_{cl} on Zhu et al.’s [84] vision poisoning attack. This is despite Peri et al.’s method being specifically tuned for Zhu et al.’s attack and their evaluation setup being both easier and less realistic by pre-training their model using a large known-clean set that is identically distributed to their \mathcal{D}_{cl} . In contrast, target-driven mitigation removed at most 0.03% of clean data on this attack – better than Peri et al. by two orders of magnitude.

Following Algorithm 4, Table 1’s experiments used only a single, randomly-selected target when performing sanitization. No steps were taken to account for additional potential targets, e.g., over-filtering the training set. Nonetheless, target-driven mitigation still significantly degraded multi-target attacks’ performance on other targets not considered when sanitizing. For example, despite considering one target, speech backdoor’s overall attack success rate (ASR) across all targets decreased from 100% to 4.7% and 6.5% for GAS and GAS-L, respectively – a 20 \times reduction. For Weber et al.’s vision backdoor attack, ASR dropped from 90.5% to 11.9% and 6.7% with GAS and GAS-L, respectively. The *key takeaway* is that identifying a single target almost entirely mitigates the attack everywhere.

7 ADAPTIVE ATTACKS

We now consider how an attacker who knows about our defense could evade it or otherwise exploit it. Our method relies on multiple

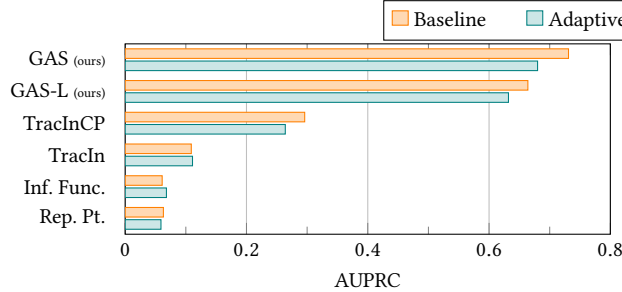


Figure 9: Adversarial-Set Identification for the Adaptive Vision Poison Attack: Mean AUPRC identifying the adversarial set where Zhu et al.’s vision poison attack is adapted to jointly minimize the adversarial loss and the GAS influence. The baseline results (orange) used Zhu et al.’s standard attack. Our jointly-optimized attack reduced the GAS similarity by 7% at the cost of a 19% decrease in ASR w.r.t. Table 1. See suppl. Sec. F.2 for the granular results, including variance.

attack instances having unusually high influence on the target instance, as measured by model gradients during training. As such, it may fail to detect an attack if (1) there are too few attack instances (relative to upper-tail count κ); (2) the attack is a large fraction of the data (e.g., 10%), in which case the instances are too common to be considered outliers; or (3) the attack instances appear no more influential on the target than clean instances. The first case is only a risk when the target instance is “easy” enough to influence that the attack can be carried out with very few instances. The second case requires a very powerful attacker, one who would be hard to stop without additional constraints or assumptions. The third case represents a possible weakness: if attackers can craft an attack that successfully changes the target label without appearing unusual, then our defense will fail. Whether or not the attacker can succeed is an empirical question, which will depend on the dataset, the model, the choice of target instance, and the attack method. Below, we provide evidence that FIT (and GAS in particular) remain effective against an attacker who is trying to evade our defense.

Seed-Instance Optimization: Some training-set attacks rely on a *fixed*, predefined adversarial perturbation which is applied to clean seed instances [47, 78]. An attacker who is aware of our defense could choose seed instances that organically appear uninfluential on some target, as estimated by GAS(-L). We apply this idea to Weber et al.’s [78] CIFAR10 backdoor attack and find that our method continues to perform well against this simple, adaptive attacker: GAS(-L) achieve 0.93 AUPRC for adversarial-set identification, a 7% decline versus the baseline, even when the attacker is given information beyond our threat model, e.g., knowledge of the random, initial parameters. Overall, the attacker’s gains from choosing different seed instances are limited. See suppl. Sec. F.3 for full details.

Perturbation Optimization: A stronger adaptive adversary actively optimizes the adversarial perturbation to be both highly effective *and* have a low (GAS) influence estimate. For attacks that find perturbations through gradient-based optimization [73, 84], the most natural way to incorporate knowledge of our method would be to add some estimate of GAS to the loss being optimized.

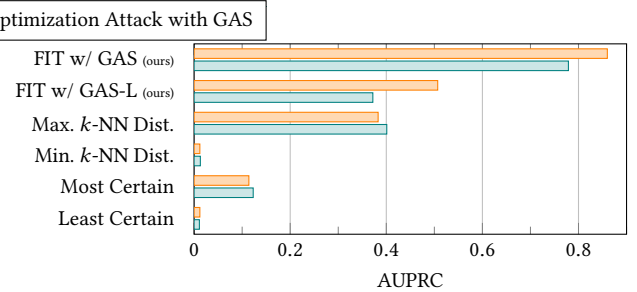


Figure 10: Target Identification for the Adaptive Vision Poison Attack: Mean target identification AUPRC where Zhu et al.’s vision poison attack is jointly optimized with minimizing GAS. FIT with GAS’s mean target identification AUPRC declined only 9% versus the baseline – an average change in target rank of 1.16 to 1.28 – still strong performance. Results are averaged across related setups with ≥ 10 trials per setup. See suppl. Sec. F.2 for the full results, including variance.

Since GAS – like poison – relies on the entire training trajectory of the model, which in turn relies on the perturbations being crafted, computing GAS’s exact gradient is intractable [8]. However, the attacker can still use a surrogate that approximates GAS, such as using fixed model checkpoints in the computation of GAS.

To evaluate the robustness of our methods to adaptive perturbations, we apply this joint optimization idea to Zhu et al.’s [84] vision poison attack. We focused on Zhu et al.’s attack because (1) it is the attack on which our method performed the worst and (2) the other optimized attack we consider [73] is restricted to only discrete token replacements, which reduces the attacker’s flexibility.

Zhu et al. iteratively optimize a set of poison examples to minimize the adversarial loss. To increase the likelihood of successfully changing the target’s label, Zhu et al. compute this loss over multiple surrogate models. The perturbations of the poison examples are constrained to an ℓ_∞ ball so that they appear relatively natural to humans. Our jointly optimized, adaptive attack adds a second term to Zhu et al.’s adversarial loss. This new term estimates the GAS influence using the same surrogate models. Hyperparameter λ balances the two objectives. See suppl. Section D for the full details of this jointly-optimized, adaptive attack, including tuning of λ .

Where possible, these adaptive experiments followed the same vision poison evaluation setup detailed in Section 6.1. However, simultaneously optimizing surrogate GAS has a much higher GPU memory cost, so we were forced to adjust the poison size and number of surrogate checkpoints to 40 and four, respectively, which degrades the attacker’s success rate from 77.9% in Table 1 to 64.3%.

Fig. 9 summarizes our adversarial-set identification performance on Zhu et al.’s vision poisoning attack with and without the jointly optimized surrogate GAS loss term.¹⁶ Observe that the attack degraded the performance of GAS(-L) & TracInCP, albeit slightly. After accounting for all other factors, this joint optimization decreased GAS’s mean adversarial-set identification from a baseline of 0.73 AUPRC to 0.68 (a 7% drop). Fig. 10 visualizes joint attack

¹⁶Both versions of the attack (i.e., with & without joint optimization) used the same evaluation setup, including the reduced surrogate model count.

Table 2: Attack Mitigation for the Adaptive Vision Poison Attack: Algorithm 4’s target-driven data sanitization where Zhu et al.’s [84] vision poison attack is jointly optimized with minimizing the GAS influence. The results below consider exclusively the jointly-optimized attack with $\lambda = 10^{-2}$. Clean-data removal remains low, and test accuracy either improved or stayed the same for in but one setup. The performance is comparable to the results with Zhu et al.’s [84]’s standard vision poisoning attack (see Table 29). Bold denotes the best mean performance with ≥ 10 trials per class pair.

Classes		Method	% Removed		ASR %		Test Acc. %	
y_{targ}	y_{adv}		\mathcal{D}_{adv}	\mathcal{D}_{cl}	Orig.	Ours	Orig.	Chg.
Bird	Dog	GAS	36.0	0.02	76.2	0	87.0	+0.1
		GAS-L	30.3	0.00	0	0	87.0	+0.1
Dog	Bird	GAS	21.6	0.00	57.1	0	87.1	+0.1
		GAS-L	21.9	0.00	0	0	87.1	-0.1
Frog	Deer	GAS	17.5	0.00	38.1	0	87.1	0.0
		GAS-L	19.4	0.00	0	0	87.1	0.0
Deer	Frog	GAS	85.0	0.18	81.0	0	87.1	0.0
		GAS-L	82.3	0.13	0	0	87.1	+0.1

optimization’s effect on target identification. Overall, joint optimization reduced FIT with GAS’s mean target identification AUPRC from a baseline of 0.86 to 0.78 (9% drop). Since Zhu et al.’s attack is single-target, this translates to the target’s average rank declining from 1.16 to 1.28 – still high performance.

Table 2 details target-driven mitigation’s effectiveness under this jointly-optimized attack. In summary, the attack results in very little clean data removal (at most 0.05% of \mathcal{D}_{cl} on average). Also, the average test accuracy after mitigation either improved or stayed the same in all but one case where it decreased by only 0.1%.

In summary, even when the adversary specifically optimized for our defense, we still effectively identify both the adversarial set and the target and then mitigate the adaptive attack.

8 DISCUSSION AND CONCLUSIONS

This paper explores two related tasks. First, we propose training-set attack *target identification*. This task is an important part of protecting critical ML systems but has thus far received relatively little attention. For example, it is impossible to conduct a truly informed cost-benefit analysis of risk without knowing the attacker’s target and by extension their objective. Knowledge of the target also enables forensic and security analysts to reason about an attacker’s identity – a key step to permanently stopping attacks by disabling the attacker. An open question is whether target identification can be combined with certified guarantees, either building on our FIT framework or creating an alternative to it.

FIT relies on identifying (groups of) highly influential training instances. To that end, we propose *renormalized influence*. By addressing influence’s low-loss penalty, renormalization significantly improves influence estimation in both adversarial and non-adversarial settings – often by an order of magnitude or more.

ACKNOWLEDGMENTS

The authors thank Jonathan Brophy for helpful discussions. This work was supported by a grant from the Air Force Research Laboratory and the Defense Advanced Research Projects Agency (DARPA) – agreement number FA8750-16-C-0166, subcontract K001892-00-S05, as well as a second grant from DARPA, agreement number HR00112090135. This work benefited from access to the University of Oregon’s HPC Talapas.

REFERENCES

- [1] Shruti Agarwal, Hany Farid, Yuming Gu, Mingming He, Koki Nagano, and Hao Li. 2019. Protecting World Leaders Against Deep Fakes. In *Proceedings of the CVPR Workshop on Media Forensics*. Long Beach, California.
- [2] Hojjat Aghakhani, Thorsten Eisenhofer, Lea Schönherr, Dorothea Kolossa, Thorsten Holz, Christopher Kruegel, and Giovanni Vigna. 2020. VENOMAVE: Clean-Label Poisoning Against Speech Recognition. *CoRR* (2020). arXiv:2010.10682 [cs.SD]
- [3] Vic Barnett and Toby Lewis. 1978. *Outliers in Statistical Data* (2nd edition ed.). John Wiley & Sons Ltd., Hoboken, New Jersey, USA.
- [4] Elnaz Barshan, Marc-Etienne Brunet, and Gintare Karolina Dziugaite. 2020. RelatIF: Identifying Explanatory Training Samples via Relative Influence. In *Proceedings of the 23rd International Conference on Artificial Intelligence and Statistics (AISTATS’20)*.
- [5] Samyadeep Basu, Phil Pope, and Soheil Feizi. 2021. Influence Functions in Deep Learning Are Fragile. In *Proceedings of the 9th International Conference on Learning Representations (ICLR’21)*. Virtual Only.
- [6] Samyadeep Basu, Xuchen You, and Soheil Feizi. 2020. On Second-Order Group Influence Functions for Black-Box Predictions. In *Proceedings of the 37th International Conference on Machine Learning (ICML’20)*. PMLR, Virtual Only.
- [7] Battista Biggio, Blaine Nelson, and Pavel Laskov. 2012. Poisoning Attacks against Support Vector Machines. In *Proceedings of the 29th International Conference on Machine Learning (ICML’12)*. PMLR, Edinburgh, Great Britain.
- [8] Avrim L. Blum and Ronald L. Rivest. 1992. Training a 3-node neural network is NP-complete. *Neural Networks* 5, 1 (1992), 117–127.
- [9] Jonathan Brophy, Zayd Hammoudeh, and Daniel Lowd. 2022. Adapting and Evaluating Influence-Estimation Methods for Gradient-Boosted Decision Trees. arXiv:2205.00359 [cs.LG] arXiv.
- [10] Bryant Chen, Wilka Carvalho, Nathalie Baracaldo, Heiko Ludwig, Benjamin Edwards, Taesung Lee, Ian Molloy, and Biplav Srivastava. 2019. Detecting Backdoor Attacks on Deep Neural Networks by Activation Clustering. In *Proceedings of the AAAI Workshop on Artificial Intelligence Safety (SafeAI’19)*. Association for the Advancement of Artificial Intelligence, Honolulu, Hawaii, USA.
- [11] Xinyun Chen, Chang Liu, Bo Li, Kimberly Lu, and Dawn Song. 2017. Targeted Backdoor Attacks on Deep Learning Systems Using Data Poisoning. arXiv:1712.05526 [cs.CR]
- [12] Yuanyuan Chen, Boyang Li, Han Yu, Pengcheng Wu, and Chunyan Miao. 2021. HyDRA: Hypergradient Data Relevance Analysis for Interpreting Deep Neural Networks. In *Proceedings of the 35th AAAI Conference on Artificial Intelligence (AAAI’21)*. Association for the Advancement of Artificial Intelligence, Virtual Only.
- [13] Cody A. Coleman, Deepak Narayanan, Daniel Kang, Tian Zhao, Jian Zhang, Luigi Nardi, Peter Bailis, Kunle Olukotun, Chris Ré, and Matei Zaharia. 2017. DAWN Bench: An End-to-End Deep Learning Benchmark and Competition. In *Proceedings of the 2017 NeurIPS Workshop on Machine Learning Systems*. Curran Associates, Inc., Long Beach, California, USA.
- [14] R. Dennis Cook and Sanford Weisberg. 1982. *Residuals and Influence in Regression*. Chapman and Hall, New York.
- [15] Christophe Croux and Peter J. Rousseeuw. 1992. A Class of High-Breakdown Scale Estimators Based on Subranges. *Communications in Statistics - Theory and Methods* 21, 7 (1992), 1935–1951.
- [16] Jesse Davis and Mark Goadrich. 2006. The Relationship Between Precision-Recall and ROC Curves. In *Proceedings of the 23rd International Conference on Machine Learning (ICML’06)*. PMLR, Pittsburgh, Pennsylvania.
- [17] Bao Gia Doan, Ehsan Abbasnejad, and Damith C. Ranasinghe. 2020. Februous: Input Purification Defense Against Trojan Attacks on Deep Neural Network Systems. In *Proceedings of the 36th Annual Computer Security Applications Conference (ACSAC’20)*. Association for Computing Machinery, Virtual Only.
- [18] Vitaly Feldman and Chiyan Zhang. 2020. What Neural Networks Memorize and Why: Discovering the Long Tail via Influence Estimation. In *Proceedings of the 34th Conference on Neural Information Processing Systems (NeurIPS’20)*. Curran Associates, Inc., Virtual Only.
- [19] Chelsea Finn, Pieter Abbeel, and Sergey Levine. 2017. Model-Agnostic Meta-Learning for Fast Adaptation of Deep Networks. In *Proceedings of the 34th International Conference on Machine Learning (ICML’17)*. PMLR, Sydney, Australia.

- [20] Liam Fowl, Micah Goldblum, Ping-yeh Chiang, Jonas Geiping, Wojciek Czaja, and Tom Goldstein. 2021. Adversarial Examples Make Strong Poisons. In *Proceedings of the 35th Conference on Neural Information Processing Systems (NeurIPS'21)*. Curran Associates, Inc., Virtual Only.
- [21] Yansong Gao, Change Xu, Derui Wang, Shiping Chen, Damith C. Ranasinghe, and Surya Nepal. 2019. STRIP: A Defence against Trojan Attacks on Deep Neural Networks. In *Proceedings of the 35th Annual Computer Security Applications Conference (ACSAC'19)*. Association for Computing Machinery, San Juan, Puerto Rico, USA.
- [22] Jonas Geiping, Liam Fowl, W. Ronny Huang, Wojciek Czaja, Gavin Taylor, Michael Moeller, and Tom Goldstein. 2021. Witches’ Brew: Industrial Scale Data Poisoning via Gradient Matching. In *Proceedings of the 9th International Conference on Learning Representations (ICLR'21)*. Virtual Only.
- [23] Robert Geirhos, Jörn-Henrik Jacobsen, Claudio Michaelis, Richard Zemel, Wieland Brendel, Matthias Bethge, and Felix A. Wichmann. 2020. Shortcut Learning in Deep Neural Networks. *Nature Machine Intelligence* 2, 11 (2020), 665–673.
- [24] Tianyu Gu, Kang Liu, Brendan Dolan-Gavitt, and Siddharth Garg. 2019. BadNets: Evaluating Backdooring Attacks on Deep Neural Networks. *IEEE Access* 7 (2019), 47230–47244.
- [25] Chuan Guo, Tom Goldstein, Awini Y. Hannun, and Laurens van der Maaten. 2020. Certified Data Removal from Machine Learning Models. In *Proceedings of the 37th International Conference on Machine Learning (ICML'20, Vol. 119)*, 3832–3842.
- [26] Han Guo, Nazneen Fatema Rajani, Peter Hase, Mohit Bansal, and Caiming Xiong. 2020. FastIF: Scalable Influence Functions for Efficient Model Interpretation and Debugging. *CoRR* abs/2012.15781 (2020). arXiv:2012.15781 <http://arxiv.org/abs/2012.15781>
- [27] Zayd Hammoudeh and Daniel Lowd. 2022. Identifying a Training-Set Attack’s Target Using Renormalized Influence Estimation. In *Proceedings of the 29th ACM SIGSAC Conference on Computer and Communications Security (CCS'22)*. Association for Computing Machinery.
- [28] Zayd Hammoudeh and Daniel Lowd. 2022. Reducing Certified Regression to Certified Classification. arXiv:2208.13904 [cs.LG]
- [29] Satoshi Hara, Atsushi Nitanda, and Takanori Maehara. 2019. Data Cleansing for Models Trained with SGD. In *Proceedings of the 33rd Conference on Neural Information Processing Systems (NeurIPS'19)*. Curran Associates, Inc., Vancouver, Canada.
- [30] Victoria J. Hodge and Jim Austin. 2004. A Survey of Outlier Detection Methodologies. *Artificial Intelligence Review* 22, 2 (Oct 2004), 85–126.
- [31] W. Ronny Huang, Jonas Geiping, Liam Fowl, Gavin Taylor, and Tom Goldstein. 2020. MetaPoison: Practical General-purpose Clean-label Data Poisoning. In *Proceedings of the 34th Conference on Neural Information Processing Systems (NeurIPS'20)*. Curran Associates, Inc., Virtual Only.
- [32] Matthew Jagielski, Giorgio Severi, Niklas Pousette Harger, and Alina Oprea. 2021. Subpopulation Data Poisoning Attacks. In *Proceedings of the 28th ACM SIGSAC Conference on Computer and Communications Security (CCS'21)*. Association for Computing Machinery, Virtual Only.
- [33] Jinyuan Jia, Xiaoyu Cao, and Neil Zhenqiang Gong. 2021. Intrinsic Certified Robustness of Bagging against Data Poisoning Attacks. In *Proceedings of the 35th AAAI Conference on Artificial Intelligence (AAAI'21)*.
- [34] Diederik P. Kingma and Jimmy Ba. 2015. Adam: A Method for Stochastic Optimization. In *Proceedings of the 3rd International Conference on Learning Representations (ICLR'15)*.
- [35] Pang Wei Koh and Percy Liang. 2017. Understanding Black-box Predictions via Influence Functions. In *Proceedings of the 34th International Conference on Machine Learning (ICML'17)*. PMLR, Sydney, Australia.
- [36] Pang Wei Koh, Jacob Steinhardt, and Percy Liang. 2018. Stronger Data Poisoning Attacks Break Data Sanitization Defenses. arXiv:1811.00741 [cs.LG]
- [37] Soheil Kolouri, Aniruddha Saha, Hamed Pirsiavash, and Heiko Hoffmann. 2019. Universal Litmus Patterns: Revealing Backdoor Attacks in CNNs. In *Proceedings of the 32nd Conference on Computer Vision and Pattern Recognition (CVPR'19)*. Long Beach, California, USA.
- [38] Alex Krizhevsky, Vinod Nair, and Geoffrey Hinton. 2014. The CIFAR-10 Dataset.
- [39] Ram Shankar Siva Kumar, Magnus Nyström, John Lambert, Andrew Marshall, Mario Goertzel, Andi Comissoneru, Matt Swann, and Sharon Xia. 2020. Adversarial Machine Learning – Industry Perspectives. In *Proceedings of the 2020 IEEE Security and Privacy Workshops (SPW'20)*.
- [40] Peter Lee. 2016. Learning from Tay’s Introduction. <https://blogs.microsoft.com/blog/2016/03/25/learning-tays-introduction/>
- [41] Kirill Levchenko, Andreas Pitsillidis, Neha Chachra, Brandon Enright, Márk Félegyházi, Chris Grier, Tristan Halvorson, Chris Kanich, Christian Kreibich, He Liu, Damon McCoy, Nicholas C. Weaver, Vern Paxson, Geoffrey M. Voelker, and Stefan Savage. 2011. Click Trajectories: End-to-End Analysis of the Spam Value Chain. *2011 IEEE Symposium on Security and Privacy (2011)*, 431–446.
- [42] Alexander Levine and Soheil Feizi. 2021. Deep Partition Aggregation: Provable Defenses against General Poisoning Attacks. In *Proceedings of the 9th International Conference on Learning Representations (ICLR'21)*. Virtual Only.
- [43] Yige Li, Xixiang Lyu, Nodens Koren, Lingjuan Lyu, Bo Li, and Xingjun Ma. 2021. Anti-Backdoor Learning: Training Clean Models on Poisoned Data. In *Proceedings of the 35th Conference on Neural Information Processing Systems (NeurIPS'21)*. Curran Associates, Inc., Virtual Only.
- [44] Yiming Li, Baoyuan Wu, Yong Jiang, Zhifeng Li, and Shu-Tao Xia. 2020. Backdoor Learning: A Survey. arXiv:2007.08745 [cs.CR]
- [45] Junyu Lin, Lei Xu, Yingqi Liu, and Xiangyu Zhang. 2020. Composite Backdoor Attack for Deep Neural Network by Mixing Existing Benign Features. In *Proceedings of the 2020 ACM SIGSAC Conference on Computer and Communications Security (CCS'20)*. Association for Computing Machinery, Virtual Only.
- [46] Kang Liu, Brendan Dolan-Gavitt, and Siddharth Garg. 2018. Fine-Pruning: Defending Against Backdooring Attacks on Deep Neural Networks. In *Proceedings of the International Symposium on Research in Attacks, Intrusions, and Defenses (RAID'18)*. Springer, Heraklion, Crete, Greece, 273–294.
- [47] Yingqi Liu, Shiqing Ma, Yours Aafet, Wen-Chuan Lee, Juan Zhai, Weihang Wang, and Xiangyu Zhang. 2018. Trojaning Attack on Neural Networks. In *Proceedings of the 25th Annual Network and Distributed System Security Symposium (NDSS'18)*. San Diego, California, USA.
- [48] Yinhai Liu, Myle Ott, Naman Goyal, Jingfei Du, Mandar Joshi, Danqi Chen, Omer Levy, Mike Lewis, Luke Zettlemoyer, and Veselin Stoyanov. 2020. RoBERTa: A Robustly Optimized BERT Pretraining Approach. In *Proceedings of the 8th International Conference on Learning Representations (ICLR'20)*. Virtual Only.
- [49] Neil G. Marchant, Benjamin I. P. Rubinstein, and Scott Alfeld. 2022. Hard to Forget: Poisoning Attacks on Certified Machine Unlearning. In *Proceedings of the 36th AAAI Conference on Artificial Intelligence (AAAI'22)*.
- [50] Luis Muñoz-González, Battista Biggio, Ambra Demontis, Andrea Paudice, Vasin Wongrassamee, Emil C Lupu, and Fabio Roli. 2017. Towards Poisoning of Deep Learning Algorithms with Back-gradient Optimization. In *Proceedings of the 10th ACM Workshop on Artificial Intelligence and Security (AISec'17)*. Association for Computing Machinery, Dallas, Texas, USA.
- [51] Myle Ott, Sergey Edunov, Alexei Baevski, Angela Fan, Sam Gross, Nathan Ng, David Grangier, and Michael Auli. 2019. fairseq: A Fast, Extensible Toolkit for Sequence Modeling. In *Proceedings of NAACL-HLT 2019: Demonstrations*.
- [52] David Page. 2020. How to Train Your ResNet. <https://myrtle.ai/learn/how-to-train-your-resnet/>
- [53] Adam Paszke, Sam Gross, Francisco Massa, Adam Lerer, James Bradbury, Gregory Chanan, Trevor Killeen, Zeming Lin, Natalia Gimelshein, Luca Antiga, Alban Desmaison, Andreas Kopf, Edward Yang, Zachary DeVito, Martin Raison, Alykhan Tejani, Sasank Chilamkurthy, Benoit Steiner, Lu Fang, Junjie Bai, and Soumith Chintala. 2019. PyTorch: An Imperative Style, High-Performance Deep Learning Library. In *Proceedings of the 33rd Conference on Neural Information Processing Systems (NeurIPS'19)*. Curran Associates, Inc., Vancouver, Canada.
- [54] Barak A. Pearlmutter. 1994. Fast Exact Multiplication by the Hessian. *Neural Computation* 6 (1994), 147–160.
- [55] Neehar Peri, Neal Gupta, W. Ronny Huang, Liam Fowl, Chen Zhu, Soheil Feizi, Tom Goldstein, and John P. Dickerson. 2020. Deep k-NN Defense Against Clean-label Data Poisoning Attacks. In *Proceedings of the ECCV Workshop on Adversarial Robustness in the Real World (AROW'20)*. Virtual Only.
- [56] James Pita, Manish Jain, Fernando Ordóñez, Christopher Portway, Milind Tambe, Craig Western, Praveen Paruchuri, and Sarit Kraus. 2009. Using Game Theory for Los Angeles Airport Security. *AI Magazine* 30 (2009), 43–57.
- [57] Garima Pruthi, Frederick Liu, Satyen Kale, and Mukund Sundararajan. 2020. Estimating Training Data Influence by Tracing Gradient Descent. In *Proceedings of the 34th Conference on Neural Information Processing Systems (NeurIPS'20)*. Curran Associates, Inc., Virtual Only.
- [58] Alex Radford, Jeff Wu, Rewon Child, David Luan, Dario Amodei, and Ilya Sutskever. 2019. Language Models are Unsupervised Multitask Learners.
- [59] Peter Rousseeuw and Christophe Croux. 1993. Alternatives to the Median Absolute Deviation. *J. Amer. Statist. Assoc.* (1993).
- [60] Peter J. Rousseeuw and Mia Hubert. 2017. Anomaly Detection by Robust Statistics. *WIREs Data Mining and Knowledge Discovery* 8, 2 (Nov 2017).
- [61] P. J. Rousseeuw and A. M. Leroy. 1987. *Robust Regression and Outlier Detection*. John Wiley & Sons, Inc., USA.
- [62] Sambuddha Saha, Aashish Kumar, Pratyush Sahay, George Jose, Srinivas Kruthiventi, and Harikrishna Muralidhara. 2019. Attack Agnostic Statistical Method for Adversarial Detection. In *Proceedings of the 1st ICCV Workshop on Statistical Deep Learning for Computer Vision*. Seoul, Korea.
- [63] Ahmed Salem, Rui Wen, Michael Backes, Shiqing Ma, and Yang Zhang. 2020. Dynamic Backdoor Attacks Against Machine Learning Models. *CoRR* (2020). arXiv:2003.03675 [cs.CR]
- [64] Ali Shahabi, W. Ronny Huang, Mahyar Najibi, Octavian Suciu, Christoph Studer, Tudor Dumitras, and Tom Goldstein. 2018. Poison Frogs! Targeted Clean-Label Poisoning Attacks on Neural Networks. In *Proceedings of the 32nd Conference on Neural Information Processing Systems (NeurIPS'18)*. Curran Associates, Inc., Montreal, Canada.
- [65] Harshay Shah, Kaustav Tamuly, Aditi Raghunathan, Prateek Jain, and Praneeth Netrapalli. 2020. The Pitfalls of Simplicity Bias in Neural Networks. In *Proceedings of the 34th Conference on Neural Information Processing Systems (NeurIPS'20)*.

- [66] Richard Socher, Alex Perelygin, Jean Wu, Jason Chuang, Christopher D. Manning, Andrew Ng, and Christopher Potts. 2013. Recursive Deep Models for Semantic Compositionality Over a Sentiment Treebank. In *Proceedings of the 8th Conference on Empirical Methods in Natural Language Processing (EMNLP'13)*.
- [67] Ezekiel O. Soremekun, Sakshi Udeshi, Sudipta Chattopadhyay, and Andreas Zeller. 2020. Exposing Backdoors in Robust Machine Learning Models. arXiv:2003.00865 [cs.LG]
- [68] Jacob Steinhardt, Pang Wei Koh, and Percy Liang. 2017. Certified Defenses for Data Poisoning Attacks. In *Proceedings of the 31st Conference on Neural Information Processing Systems (NeurIPS'17)*. Curran Associates, Inc., Long Beach, California, USA.
- [69] Christian Szegedy, Wojciech Zaremba, Ilya Sutskever, Joan Bruna, Dumitru Erhan, Ian Goodfellow, and Rob Fergus. 2013. Intriguing Properties of Neural Networks. arXiv:1312.6199 [cs.CV]
- [70] Brandon Tran, Jerry Li, and Aleksander Madry. 2018. Spectral Signatures in Backdoor Attacks. In *Proceedings of the 32nd Conference on Neural Information Processing Systems (NeurIPS'18)*. Curran Associates, Inc., Montreal, Canada.
- [71] Sakshi Udeshi, Shanshan Peng, Gerald Woo, Lionell Loh, Louth Rawshan, and Sudipta Chattopadhyay. 2019. Model Agnostic Defence against Backdoor Attacks in Machine Learning. arXiv:1908.02203 [cs.LG]
- [72] Miguel Villarreal-Vasquez and Bharat K. Bhargava. 2020. ConFoc: Content-Focus Protection Against Trojan Attacks on Neural Networks. arXiv:2007.00711 [cs.CV]
- [73] Eric Wallace, Tony Z. Zhao, Shi Feng, and Sameer Singh. 2021. Concealed Data Poisoning Attacks on NLP Models. In *Proceedings of the North American Chapter of the Association for Computational Linguistics (NAACL'21)*.
- [74] Binghui Wang, Xiaoyu Cao, Jinyuan Jai, and Neil Zhenqiang Gong. 2020. On Certifying Robustness against Backdoor Attacks via Randomized Smoothing. In *Proceedings of the CVPR Workshop on Adversarial Machine Learning in Computer Vision*.
- [75] Bolun Wang, Yuanshun Yao, Shawn Shan, Huiying Li, Bimal Viswanath, Haitao Zheng, and Ben Y. Zhao. 2019. Neural Cleanse: Identifying and Mitigating Backdoor Attacks in Neural Networks. In *Proceedings of the 40th IEEE Symposium on Security and Privacy (SP'19)*. San Francisco, CA.
- [76] Tongzhou Wang, Jun-Yan Zhu, Antonio Torralba, and Alexei A. Efros. 2018. Dataset Distillation. arXiv:1811.10959 [cs]
- [77] Wenxiao Wang, Alexander Levine, and Soheil Feizi. 2022. Improved Certified Defenses against Data Poisoning with (Deterministic) Finite Aggregation. In *Proceedings of the 39th International Conference on Machine Learning (ICML'22)*.
- [78] Maurice Weber, Xiaojun Xu, Bojan Karlaš, Ce Zhang, and Bo Li. 2021. RAB: Provable Robustness Against Backdoor Attacks. arXiv:2003.08904 [cs.LG]
- [79] Huang Xiao, Battista Biggio, Gavin Brown, Giorgio Fumera, Claudia Eckert, and Fabio Roli. 2015. Is Feature Selection Secure against Training Data Poisoning?. In *Proceedings of the 32nd International Conference on Machine Learning (ICML'15)*. PMLR, Lille, France.
- [80] Xiaojun Xu, Qi Wang, Huichen Li, Nikita Borisov, Carl A. Gunter, and Bo Li. 2021. Detecting AI Trojans Using Meta Neural Analysis. In *Proceedings of the 42nd IEEE Symposium on Security and Privacy (SP'21)*. IEEE, Virtual Only.
- [81] Chih-Kuan Yeh, Joon Sik Kim, Ian E.H. Yen, and Pradeep Ravikumar. 2018. Reresenter Point Selection for Explaining Deep Neural Networks. In *Proceedings of the 32nd Conference on Neural Information Processing Systems (NeurIPS'18)*. Curran Associates, Inc., Montreal, Canada.
- [82] Da Yu, Huihuai Zhang, Wei Chen, Jian Yin, and Tie-Yan Liu. 2021. Indiscriminate Poisoning Attacks are Shortcuts. arXiv:2111.00898 [cs.LG]
- [83] Rui Zhang and Shihua Zhang. 2022. Rethinking Influence Functions of Neural Networks in the Over-Parameterized Regime. In *Proceedings of the 36th AAAI Conference on Artificial Intelligence (AAAI'22)*. Association for the Advancement of Artificial Intelligence, Vancouver, Canada.
- [84] Chen Zhu, W Ronny Huang, Ali Shafahi, Hengduo Li, Gavin Taylor, Christoph Studer, and Tom Goldstein. 2019. Transferable Clean-Label Poisoning Attacks on Deep Neural Nets. In *Proceedings of the 36th International Conference on Machine Learning (ICML'19)*. PMLR, Los Angeles, CA.
- [85] Liuwan Zhu, Rui Ning, Cong Wang, Chunsheng Xin, and Hongyi Wu. 2020. GangSweep: Sweep out Neural Backdoors by GAN. In *Proceedings of the 28th ACM International Conference on Multimedia (MM'20)*.
- [86] Liuwan Zhu, Rui Ning, Chunsheng Xin, Chonggang Wang, and Hongyi Wu. 2021. CLEAR: Clean-up Sample-Targeted Backdoor in Neural Networks. In *Proceedings of the 18th International Conference on Computer Vision (ICCV'21)*.

Identifying a Training-Set Attack’s Target Using Renormalized Influence Estimation

Supplemental Materials

Table of Contents

A Additional Algorithms	A3
A.1 Runtime Complexity of FIT	A3
B Proof	A4
C Detailed Experimental Setup	A4
C.1 Dataset Configurations	A4
C.1.1 Training Set Sizes	A5
C.1.2 Target Set Sizes	A5
C.2 Hyperparameters	A6
C.2.1 Model Training	A6
C.2.2 Upper-Tail Heaviness Hyperparameters	A6
C.2.3 Target-Driven Mitigation Hyperparameters	A7
C.2.4 Adversarial Set \mathcal{D}_{adv} Crafting	A7
C.2.5 Baselines	A8
C.3 Network Architectures	A9
D Convex Polytope Poisoning & GAS Joint Optimization	A12
E Representative Perturbed Examples	A14
E.1 Speech Recognition Backdoor	A14
E.2 Vision Backdoor	A14
E.3 Natural Language Poison	A15
E.4 Vision Poison	A15
F Additional Experimental Results	A16
F.1 Full Experimental Results	A16
F.1.1 Speech Recognition Backdoor Full Results	A16
F.1.2 Vision Backdoor Full Results	A18
F.1.3 Natural Language Poisoning Full Results	A20
F.1.4 Vision Poisoning Full Results	A22
F.2 Jointly-Optimized Adaptive Attacker – Full Experimental Results	A24
F.2.1 Adversarial-Set Identification of the Jointly Optimized Poisoning Attack	A24
F.2.2 Target Identification of the Jointly Optimized Poisoning Attack	A25
F.2.3 Target-Driven Attack Mitigation of the Jointly Optimized Poisoning Attack	A26
F.3 Adaptive Adversarial-Instance Selection	A27
F.4 An Adversarial Attack on Target-Driven Mitigation	A28
F.5 Poisoning-Rate Ablation Study	A30
F.5.1 Adversarial-Set Identification Ablation Study	A31

F.5.2 Target-Identification Ablation Study	A32
F.5.3 Target-Driven Attack Mitigation Ablation Study	A33
F.5.4 Ablation Study Reference Tables	A35
F.6 Upper-Tail Heaviness Hyperparameter κ Sensitivity Analysis	A38
F.7 Alternatives to Renormalization	A39
F.8 Why Aggregate Training Gradients?	A40
F.9 Evaluating on the Tail of the Attack’s Influence Distribution	A42
F.10 Adversarial-Set Identification Execution Time	A43

A ADDITIONAL ALGORITHMS

Algorithm 5 outlines TracIn’s influence estimation procedure for *a priori* unknown test instance \hat{z}_{te} . Algorithm 2, which combines the procedures of GAS and TracInCP, is re-included below to facilitate easier side-by-side comparison.

Algorithm 5 TracIn influence estimation

Input: Training parameters \mathcal{P} , iteration subset \mathcal{T} , iteration count T , batches $\mathcal{B}_1, \dots, \mathcal{B}_T$, batch size b , and test example \hat{z}_{te}

Output: Influence vector \mathbf{v}

```

1:  $\mathbf{v} \leftarrow \vec{0}$                                      ▷ Initialize
2: for  $t \leftarrow 1$  to  $T$  do
3:   if  $t \in \mathcal{T}$  then
4:      $(\eta, \theta) \leftarrow \mathcal{P}[t]$                   ▷ Equiv. to  $(\eta_t, \theta_{t-1})$ 
5:      $\hat{g}_{\text{te}} \leftarrow \nabla_{\theta} \mathcal{L}(\hat{z}_{\text{te}}, \theta)$ 
6:   for each  $z_i \in \mathcal{B}_t$  do                   ▷ Batch examples
7:      $g_i \leftarrow \nabla_{\theta} \mathcal{L}(z_i; \theta)$ 
8:      $\mathbf{v}_i \leftarrow \mathbf{v}_i + \frac{\eta}{b} \langle g_i, \hat{g}_{\text{te}} \rangle$     ▷ Unnormalized
9: return  $\mathbf{v}$ 

```

Algorithm 2: GAS vs. TracInCP

Input: Training params. \mathcal{P} , training set \mathcal{D}_{tr} , batch size b , & test ex. \hat{z}_{te}

Output: (Renormalized) influence vector \mathbf{v}

```

1:  $\mathbf{v} \leftarrow \vec{0}$                                      ▷ Initialize
2: for each  $(\eta_t, \theta_{t-1}) \in \mathcal{P}$  do
3:    $\hat{g}_{\text{te}} \leftarrow \nabla_{\theta} \mathcal{L}(\hat{z}_{\text{te}}, \theta_{t-1})$ 
4:   for each  $z_i \in \mathcal{D}_{\text{tr}}$  do                  ▷ All examples
5:      $g_i \leftarrow \nabla_{\theta} \mathcal{L}(z_i; \theta_{t-1})$ 
6:     if calculating TracInCP then
7:        $\mathbf{v}_i \leftarrow \mathbf{v}_i + \frac{\eta_t}{b} \langle g_i, \hat{g}_{\text{te}} \rangle$     ▷ Unnormalized (Sec. 3.2)
8:     else if calculating GAS then
9:        $\mathbf{v}_i \leftarrow \mathbf{v}_i + \frac{\eta_t}{b} \left\langle \frac{g_i}{\|g_i\|}, \frac{\hat{g}_{\text{te}}}{\|\hat{g}_{\text{te}}\|} \right\rangle$     ▷ Renormalized (Sec. 4.3)
10:  return  $\mathbf{v}$ 

```

Algorithm 6 overviews the implementation strategy of FIT that was used in our evaluation.

Algorithm 6 FIT target identification implementation

Input: Training set \mathcal{D}_{tr} , training set size n , test example set $\hat{\mathcal{Z}}_{\text{te}}$, and upper-tail count κ

Output: Sanitized model parameters $\tilde{\theta}_T$ & training set $\tilde{\mathcal{D}}_{\text{tr}}$

```

1:  $\mathcal{V} \leftarrow \left\{ \text{GAS}(\hat{z}_j; \mathcal{D}_{\text{tr}}) : \hat{z}_j \in \hat{\mathcal{Z}}_{\text{te}} \right\}$           ▷ Renorm. Inf. (Alg. 2)
2:  $\Sigma \leftarrow \left\{ \frac{\mathbf{v}^{(j)} - \mu^{(j)}}{Q^{(j)}} : \mathbf{v}^{(j)} \in \mathcal{V} \right\}$           ▷ Anomaly score (Sec. 5.2)
3:  $\mathcal{H} \leftarrow \left\{ \sigma_{(n-\kappa)} : \sigma \in \Sigma \right\}$           ▷ Upper-tail heaviness (Sec. 5.2)
4: Rank  $\hat{\mathcal{Z}}_{\text{te}}$  by heaviness  $\mathcal{H}$ 
5:  $\tilde{\theta}_T, \tilde{\mathcal{D}}_{\text{tr}} \leftarrow \theta_T, \mathcal{D}_{\text{tr}}$ 
6: for each target  $\hat{z}_{\text{targ}}$  identified using  $\mathcal{H}$  do
7:    $\tilde{\theta}_T, \tilde{\mathcal{D}}_{\text{tr}} \leftarrow \text{MITIGATE}(\hat{z}_{\text{targ}}, \tilde{\theta}_T, \tilde{\mathcal{D}}_{\text{tr}})$           ▷ Sec. 5.3
8: return  $\tilde{\theta}_T, \tilde{\mathcal{D}}_{\text{tr}}$ 

```

A.1 Runtime Complexity of FIT

We assume that the model being attacked (and defended) is a neural network with parameter vector θ , trained from dataset \mathcal{D}_{tr} using some form of stochastic descent for T epochs, and evaluated on test set $\hat{\mathcal{Z}}_{\text{te}}$. For convenience, let $n := |\mathcal{D}_{\text{tr}}|$ and $m := |\hat{\mathcal{Z}}_{\text{te}}|$. Computing the gradient for a single example can be done in time $O(|\theta|)$, so training the network by computing gradient updates for all instances in all epochs is $O(|\theta|nT)$.

For FIT (Algorithm 6), we need to estimate the influence of each training instance on each test instance. If we save the parameters from $|\mathcal{T}| \leq T$ checkpoints, we can run TracIn, TracInCP, or GAS-L once to compute the influence of each training instance on a single target, requiring time $O(|\theta|n|\mathcal{T}|)$. To compute the influence on all test examples requires computing their gradients at each checkpoint and computing dot products with each training example, for a total runtime of: $O(|\theta|n|\mathcal{T}|m)$. This grows linearly in the number of training examples times the number of test examples and is the slowest part of FIT in practice. An important question for future work is how to accelerate this procedure, such as heuristically pruning the number of training and test examples under consideration, similar to previous work [26].

For mitigation (Algorithm 4), model training and influence estimation are repeated as each test example or group of test examples is removed, until the predicted label changes. Let l denote the number of iterations before the label flips. However, the influence estimation only needs to be done for the selected target example, not for all test examples. Thus, the model retraining requires time $O(|\theta|nTl)$, and the influence re-estimation requires time $O(|\theta||\mathcal{T}|l)$, which is less than the initial influence estimation time because $l < m$.

B PROOF

Proof of Theorem 4.1

THEOREM. Let loss function $\tilde{\ell}: \mathbb{R} \rightarrow \mathbb{R}_{\geq 0}$ be twice-differentiable and strictly convex as well as either even¹⁷ or monotonically decreasing. Then, it holds that

$$\tilde{\ell}(a) < \tilde{\ell}(a') \implies \|\nabla_a \tilde{\ell}(a)\|_2 < \|\nabla_a \tilde{\ell}(a')\|_2. \quad (14)$$

PROOF.

Theorem 4.1 specifies that property,

$$\tilde{\ell}(a) < \tilde{\ell}(a') \implies \|\nabla_a \tilde{\ell}(a)\|_2 < \|\nabla_a \tilde{\ell}(a')\|_2,$$

holds when loss function $\tilde{\ell}$ is strictly convex (i.e., $\forall_{a \in \mathbb{R}} \nabla_a^2 \tilde{\ell}(a) > 0$) and either monotonically decreasing or even. We prove the claim separately for these two disjoint cases.

For any monotonically decreasing $\tilde{\ell}$, by definition

$$\tilde{\ell}(a) < \tilde{\ell}(a') \implies a > a'.$$

Then, given $\forall_{a \in \mathbb{R}} \nabla_a^2 \tilde{\ell}(a) > 0$, it holds that

$$\nabla_a \tilde{\ell}(a) > \nabla_a \tilde{\ell}(a'). \quad (15)$$

For any scalar, monotonically decreasing function $\tilde{\ell}$, it holds that $\nabla_a \tilde{\ell}(a') \leq 0$ meaning Eq. (15)'s inequality flips w.r.t. L_2 norms, i.e.,

$$\|\nabla_a \tilde{\ell}(a)\|_2 < \|\nabla_a \tilde{\ell}(a')\|_2, \quad (16)$$

as for any $x, x' \in \mathbb{R}_{\leq 0}$ it holds that $x > x' \implies \|x\|_2 < \|x'\|_2$.

Formally, a function $\tilde{\ell}$ is even if

$$\forall_a \tilde{\ell}(a) = \tilde{\ell}(-a). \quad (17)$$

For even $\tilde{\ell}$, it holds that $\nabla_a \tilde{\ell}(0) = 0$ provided twice differentiability. Given $\forall_{a \in \mathbb{R}} \nabla_a^2 \tilde{\ell}(a) > 0$, then $\forall_{a < 0} \nabla_a \tilde{\ell}(a) < 0$. Hence over restricted domain $\mathbb{R}_{\leq 0}$, $\tilde{\ell}$ is monotonically decreasing. Above it was shown that Eq. (8) holds for monotonically decreasing functions so

$$\tilde{\ell}(-|a|) < \tilde{\ell}(-|a'|) \implies \|\nabla_a \tilde{\ell}(-|a|)\|_2 < \|\nabla_a \tilde{\ell}(-|a'|)\|_2. \quad (18)$$

Evenness induces function symmetry about the origin so

$$\forall_a |\nabla_a \tilde{\ell}(a)| = |\nabla_a \tilde{\ell}(-a)|, \quad (19)$$

and by extension

$$\forall_a \|\nabla_a \tilde{\ell}(a)\|_2 = \|\nabla_a \tilde{\ell}(-a)\|_2. \quad (20)$$

Eqs. (17) and (20) allow Eq. (18)'s absolute values and negations to be dropped completing the proof. \square

C DETAILED EXPERIMENTAL SETUP

This section details the evaluation setup used in Section 4 and 6's experiments, including dataset specifics, hyperparameters, and the neural network architectures.

Our source code can be downloaded from https://github.com/ZaydH/target_identification. All experiments used the PyTorch automatic differentiation framework [53] and were tested with Python 3.6.5. Wallace et al.'s [73] sentiment analysis data poisoning source code will be published by its authors at <https://github.com/Eric-Wallace/data-poisoning>.

C.1 Dataset Configurations

This subsection provides details related to dataset configurations.

Section 4.1 performs binary classification of frog vs. airplane from CIFAR10. Added as a small adversarial set (\mathcal{D}_{adv}) is 150 MNIST 0 training instances selected at random. We considered this class pair specifically since among the $\binom{10}{2}$ possible CIFAR10 class pairs, the MNIST test misclassification rate was closest to uniformly at random (u.a.r.) for frog vs. airplane (47.5% actual vs. 50% u.a.r. – uniformly at random). Hence, on average, neither frog nor airplane is overly influential on MNIST. Note that no external constraints induced this near u.a.r. misclassification rate.

Section 4.5 compares the ability of influence estimators, with and without renormalization, to identify influential groups of training examples on non-adversarial, CIFAR10, binary classification with Figure 4's results averaged across five class pairs. Two of the class pairs, airplane vs. bird and automobile vs. dog, were studied by Weber et al. [78] in relation to certified defenses. The three other class pairs – cat vs. ship, frog vs. horse, and frog vs. truck – were selected at random.

¹⁷"Even" denotes that the function satisfies $\forall_a \tilde{\ell}(a) = \tilde{\ell}(-a)$.

Wallace et al.'s [73] poisoning method attacks the SST-2 dataset [66]. We consider detection on 8 short movie reviews – four positive and four negative – all selected at random by Wallace et al.'s implementation. The specific reviews considered appear in Table 3.

Table 3: SST-2 movie reviews selected by Wallace et al.'s [73] poisoning attack implementation.

Sentiment	No.	Text
Positive ↑ ↓	1	<i>a delightful coming-of-age story.</i>
	2	<i>a smart, witty follow-up.</i>
	3	<i>ahhhh ... revenge is sweet!</i>
	4	<i>a giggle a minute.</i>
Negative ↑ ↓	1	<i>oh come on.</i>
	2	<i>do not see this film.</i>
	3	<i>it's a buggy drag</i>
	4	<i>or emptying rat traps.</i>

The next section provides details regarding the adversarial datasets sizes.

C.1.1 Training Set Sizes. Table 4 details the dataset sizes used to train all evaluated models in Section 6.

Table 4: Dataset sizes

Dataset	Attack	# Classes	# Train	# Test
CIFAR10 [38]	Poison	5	25,000	5,000
SST-2 ¹⁸ [66]	Poison	2	67,349	N/A
Speech [47]	Backdoor	10	3,000 ¹⁹	1,184
CIFAR10 [38]	Backdoor	2	10,000	2

Liu et al.'s [47] speech backdoor dataset includes training and test examples with their associated adversarial trigger already embedded. We used their adversarial dataset unchanged. Table 5 details $|\mathcal{D}_{\text{adv}}|$ (i.e., adversarial training set size) for each speech digit pair after a fixed, random train-validation split.

Table 5: Number of backdoor training examples for each speech backdoor digit pair. As detailed above, Liu et al.'s [47] dataset provides 30 backdoored instances for each digit pair. The remainder of the 30 instances for each digit pair are part of the fixed, validation set.

Digit Pair	$0 \rightarrow 1$	$1 \rightarrow 2$	$2 \rightarrow 3$	$3 \rightarrow 4$	$4 \rightarrow 5$	$5 \rightarrow 6$	$6 \rightarrow 7$	$7 \rightarrow 8$	$8 \rightarrow 9$	$8 \rightarrow 9$
$ \mathcal{D}_{\text{adv}} $	26	27	24	24	26	28	26	26	22	21

C.1.2 Target Set Sizes. Table 6 details the sizes of the target and non-target sets considered in Section 6.3's target identification experiments. Davis and Goadrich [16] explain that the class imbalance ratio between classes defines the unattainable regions in the precision-recall curve. By extension, this ratio also dictates the baseline AUPRC value if examples are labeled randomly.

Table 6: Target and non-target set sizes used in Section 6.3's target identification experiments.

Attack	Type	# Targets	# Non-Targets
Backdoor	Speech	10	220
	Vision	35	250
Poison	NLP	1	125
	Vision	1	450

¹⁸Stanford Sentiment Treebank dataset (SST-2) is used for sentiment analysis

¹⁹Clean only. Dataset also has 300 backdoored samples divided evenly among the 10 attack class pairs (e.g., $0 \rightarrow 1$, $1 \rightarrow 2$, etc.).

C.2 Hyperparameters

This section details three primary hyperparameter types, namely: hyperparameters used to create adversarial set \mathcal{D}_{adv} (if any), hyperparameter used when training model f , and influence estimator hyperparameters.

C.2.1 Model Training. Table 7 enumerates the hyperparameters used when training the models analyzed in Section 4.

Table 7: Renormalized influence model training hyperparameter settings

Hyperparameter	CIFAR10 & MNIST		Filtering
θ_0 Pretrained?			✓*
Data Augmentation?			✓
Validation Split	$\frac{1}{6}$	$\frac{1}{6}$	
Optimizer	Adam	Adam	
$ \mathcal{D}_{\text{adv}} $	150	N/A	
Batch Size	64	64	
# Epochs	10	10	
# Subepochs (ω) ²⁰	5	3	
η (Peak)	$1 \cdot 10^{-3}$	$1 \cdot 10^{-3}$	
η Scheduler	One cycle	One cycle	
λ (Weight Decay)	$1 \cdot 10^{-3}$	$1 \cdot 10^{-3}$	

Table 8 enumerates the hyperparameters used when training the adversarially-attacked models analyzed in Sections 6 and F.

Table 8: Training-set attack model training hyperparameter settings

Hyperparameter	Poison		Backdoor	
	CIFAR10	SST-2	Speech	CIFAR10
θ_0 Pretrained?	✓	✓		
Existing Adv. Dataset			✓	
Data Augmentation?	✓			
Validation Split	$\frac{1}{6}$	Predefined	$\frac{1}{6}$	$\frac{1}{6}$
Optimizer	SGD	Adam	SGD	Adam
$ \mathcal{D}_{\text{adv}} $	50	50	21–28 ²¹	150
$ \mathcal{D}_{\text{cl}} $	24,950	67,349	3,000	9,850
Poisoning Rate $\left(\frac{ \mathcal{D}_{\text{adv}} }{ \mathcal{D}_{\text{tr}} }\right)$	0.20%	0.07%	0.99%	1.50%
Batch Size	256	32	32	64
# Epochs	30	4	30	10
# Subepochs (ω)	5	3	3	5
η (Peak)	$1 \cdot 10^{-3}$	$1 \cdot 10^{-5}$	$1 \cdot 10^{-3}$	$1 \cdot 10^{-3}$
η Scheduler	One cycle	Poly. decay	One cycle	One cycle
λ (Weight Decay)	$1 \cdot 10^{-1}$	$1 \cdot 10^{-1}$	$1 \cdot 10^{-3}$	$1 \cdot 10^{-3}$
Dropout Rate	N/A	0.1	N/A	N/A

C.2.2 Upper-Tail Heaviness Hyperparameters. Section 5.2 defines the upper-tail heaviness of influence vector v as the κ -th largest anomaly score in vector σ . Table 9 defines the hyperparameter value κ used for each of Section 6.1’s four attacks.

²⁰We use the term “ ω subepoch checkpointing” ($\omega \in \mathbb{Z}_+$) to denote that iteration subset \mathcal{T} is formed from ω evenly-spaced checkpoints within each epoch. ω was not tuned, and was selected based on overall execution time and compute availability.

²¹Varies by digit pair. See Table 5.

Table 9: Upper-tail heaviness cutoff count (κ)

Attack	Type	Tail Count (κ)
Backdoor	Speech	10
	Vision	10
Poison	NLP	10
	Vision	2

C.2.3 Target-Driven Mitigation Hyperparameters. Algorithm 4 details our target-driven attack mitigation algorithm, which uses filtering cutoff hyperparameter ζ to tune how much data to filter in each filtering iteration. Table 10 details the hyperparameter settings used in Section 6.4's attack mitigation experiments.

For each attack, multiple trials were performed with different target examples, class pairs, attack triggers, etc. For each such trial, we repeated the mitigation experiment multiple times to ensure the most representative numbers with the number of repeats enumerated in Table 10.

In addition, cutoff threshold ζ was set to an initial value. After a specified number of iterations l , ζ was decreased by a specified step-size. This process continued until the attack had been mitigated. To summarize, iteration l 's mitigation cutoff value ζ is

$$\zeta_l = \zeta_{\text{initial}} - \psi \left\lfloor \frac{l}{\text{StepCount}} \right\rfloor, \quad (21)$$

with the corresponding value of each parameter in Table 10.

Table 10: Target-driven attack mitigation hyperparameters

Hyperparameter	Poison		Backdoor	
	CIFAR10	SST-2	Speech	CIFAR10
Repeats Per Trial	3	3	5	5
ζ_{initial} Initial Cutoff	3	4	3	2
Anneal Step Size (ψ)	0.25	0.5	0.25	0.25
Anneal Step Count	1	1	4	4

C.2.4 Adversarial Set \mathcal{D}_{adv} Crafting. Liu et al.'s [47] speech recognition dataset comes bundled with 300 backdoor training examples. The adversarial trigger takes the form of white noise inserted at the beginning of the speech recording. We used the dataset unchanged except for a fixed training/validation split used in all experiments. Only one backdoor digit pair (e.g., 0 → 1, 1 → 2, etc.) is considered at a time.

Weber et al. [78] consider backdoor three different backdoor adversarial trigger types on CIFAR10 binary classification. The three attack patterns are:

- (1) *1 Pixel*: The image's center pixel is perturbed to the maximum value.
- (2) *4 Pixel*: Four specific pixels near the image's center had their pixel value increased a fixed amount.
- (3) *Blend*: A fixed isotropic Gaussian-noise pattern ($\mathcal{N}(0, I)$) across the entire image.

Table 11 defines each attack pattern's maximum L_2 perturbation distance. Any perturbation that exceeded the pixel minimum/maximum values was clipped to the valid range.

Table 11: CIFAR10 vision backdoor adversarial trigger maximum ℓ_2 -norm perturbation distance

Pattern	Max. ℓ_2
1 Pixel	$\sqrt{3}$
4 Pixel	2
Blend	4

Wallace et al. [73] construct single-target natural language poison using the traditional poisoning bilevel optimization,

$$\arg \min_{\mathcal{D}_{\text{adv}}} \mathcal{L}_{\text{adv}} \left(\hat{\mathbf{z}}_{\text{targ}}, \arg \min_{\theta} \sum_{z \in \mathcal{D}_{\text{cl}} \cup \mathcal{D}_{\text{adv}}} \mathcal{L}(z_i; \theta) \right), \quad (22)$$

where L_{adv} uses the attacker's *adversarial loss function*, $\ell_{\text{adv}} : \mathcal{A} \times \mathcal{Y} \rightarrow \mathbb{R}_{\geq 0}$, in place of training loss function ℓ [7, 50]. To make the computation tractable, Wallace et al. approximate inner minimizer, $\arg \min_{\theta} \sum_{z \in \mathcal{D}_{\text{cl}} \cup \mathcal{D}_{\text{adv}}} \mathcal{L}(z_i; \theta)$, using second-order gradients similar to [19, 31, 76]. Wallace et al.'s method initializes each poison instance from a seed phrase, and tokens are iteratively replaced with alternates that align well with the poison example's gradient.

Like Wallace et al., our experiments attacked sentiment analysis on the Stanford Sentiment Treebank v2 (SST-2) dataset [66]. We targeted 8 (4 positive & 4 negative – see Table 3) reviews selected by Wallace et al.'s implementation and generated $|\mathcal{D}_{\text{adv}}| = 50$ new poison in each trial.

Zhu et al.'s [84] targeted, clean-label attack crafts a set of poisons by forming a *convex polytope* around the target's feature representation. Our experiments used the author's open-source implementation when crafting the poison. Their implementation is gray-box and assumes access to a known pre-trained network (excluding the randomly-initialized, linear classification layer).

Both Zhu et al.'s [84] and Wallace et al.'s [73] poison crafting algorithms have their own dedicated hyperparameters, which are detailed in Tables 12 and 13 respectively. Note that Table 13's hyperparameters are taken unchanged from the original source code provided by Wallace et al.

Table 12: Convex polytope poison crafting [84] hyperparameter settings

Hyperparameter	Value
# Iterations	1,000
Learning Rate	$4 \cdot 10^{-2}$
Weight Decay	0
Max. Perturb. (ϵ)	0.1

Table 13: SST-2 sentiment analysis poison crafting hyperparameter settings. These are identical to Wallace et al.'s [73] hyperparameter settings.

Hyperparameter	Value
Optimizer	Adam
Total Num. Updates	20,935
# Warmup Updates	1,256
Max. Sentence Len.	512
Max. Batch Size	7
Learning Rate	$1 \cdot 10^{-5}$
LR Scheduler	Polynomial Decay

C.2.5 Baselines.

C.2.5 Baselines. We exclusively considered influence-estimation methods applicable to neural models and excluded influence methods specific to alternate architectures [9].

Koh and Liang's [35] influence functions estimator uses Pearlmutter's [54] stochastic Hessian-vector product (HVP) estimation algorithm. Pearlmutter's algorithm requires 5 hyperparameters, and we follow Koh and Liang's notation for these parameters below.

Influence functions' five hyperparameters are required to ensure estimator quality and to prevent numerical instability/divergence. Table 14 details the influence functions hyperparameters used for each of Section 6's datasets. t and r were selected to make a single pass through the training set in accordance with the procedure specified by Koh and Liang.

As noted by Basu et al. [5], influence functions can be fragile on deep networks. We tuned β and γ to prevent HVP divergence, which is common with influence functions.

Our influence functions implementation was adapted from the versions published by [26] and in the Python package `pytorch_influence_functions`.²²

Second-order influence functions [6] are more brittle and computationally expensive than the first-order version. Renormalization is intended as a first-order correction and addresses our two tasks without the costs/issues related to second-order methods.

Chen et al.'s [12] HyDRA is an additional dynamic influence estimator. However, HyDRA's $\mathcal{O}(n|\theta|)$ memory complexity makes it impractical in most modern applications with large models and datasets. We focus on TracIn as its memory complexity is only $\mathcal{O}(n)$. HyDRA and TracIn were published contemporaneously and share the same core idea.²³

²²Package source code: https://github.com/nimarb/pytorch_influence_functions.

²³Our influence renormalization – proposed in Section 4 – also applies to HyDRA.

Table 14: Influence functions hyperparameter settings

Hyperparameter	Renormalization		Poison		Backdoor	
	CIFAR10 & MNIST	Non-adversarial	CIFAR10	SST-2	Speech	CIFAR10
Batch Size	1	1	1	1	1	1
Damp (β)	$1 \cdot 10^{-2}$	$5 \cdot 10^{-3}$	$1 \cdot 10^{-2}$	$1 \cdot 10^{-2}$	$5 \cdot 10^{-3}$	$1 \cdot 10^{-2}$
Scale (y)	$3 \cdot 10^7$	$1 \cdot 10^4$	$3 \cdot 10^7$	$1 \cdot 10^6$	$1 \cdot 10^4$	$3 \cdot 10^7$
Recursion Depth (t)	1,000	1,000	2,500	6,740	1,000	1,000
Repeats (r)	10	10	10	10	10	10

Peri et al.’s [55] Deep k -NN defense labels a training example as poison if its label does not match the plurality of its neighbors. For Deep k -NN to accurately identify poison, it must generally hold that $k > 2|\mathcal{D}_{\text{adv}}|$. Peri et al. propose selecting k using the *normalized k -ratio*, k/N , where N is the size of the largest class in \mathcal{D}_{tr} .

Peri et al.’s ablation study showed that Deep k -NN generally performed best when the normalized k -ratio was in the range [0.2, 2]. To ensure a strong baseline, our experiments tested Deep k -NN with three normalized k -ratio values, {0.2, 1, 2},²⁴ and we report the top-performing k ’s result.

Target identification baselines maximum and minimum k -NN distance depend on k in order to generate target rankings. Given k ’s similarity to our tail cutoff count κ , we use the same hyperparameter settings for both with the values in Table 9.

C.3 Network Architectures

Table 15 details the CIFAR10 neural network architecture. Specially, we used Page’s [52] ResNet9 architecture, which is the state-of-the-art for fast, high-accuracy (>94%) CIFAR10 classification on DAWNBench [13] at the time of writing.

Following Wallace et al. [73], natural language poisoning attacked Liu et al.’s [48] RoBERTa_{BASE} pre-trained parameters. All language model training used Facebook AI Research’s fairseq sequence-to-sequence toolkit [51] as specified by Wallace et al.. The text was encoded using Radford et al.’s [58] *byte-pair encoding* (BPE) scheme.

The speech classification convolutional neural network is identical to that used by Liu et al. [47] except for two minor changes. First, batch normalization [69] was used instead of dropout to expedite training convergence. In addition, each convolutional layer’s kernel count was halved to allow the model to be trained on a single NVIDIA Tesla K80 GPU.

²⁴This corresponds to $k \in \{833, 4167, 8333\}$ for 25,000 CIFAR10 training examples and a $\frac{1}{6}$ validation split ratio.

Table 15: ResNet9 neural network architecture

	Conv1	In=3	Out=64	Kernel=3 × 3	Pad=1
	BatchNorm2D	Out=64			
	ReLU				
	Conv2	In=64	Out=128	Kernel=3 × 3	Pad=1
	BatchNorm2D	Out=128			
	ReLU				
	MaxPool2D	2 × 2			
↑ ResNet1 ↓	ConvA	In=128	Out=128	Kernel=3 × 3	Pad=1
	BatchNorm2D	Out=128			
	ReLU				
	ConvB	In=128	Out=128	Kernel=3 × 3	Pad=1
	BatchNorm2D	Out=128			
	ReLU				
	Conv3	In=128	Out=256	Kernel=3 × 3	Pad=1
	BatchNorm2D	Out=256			
	ReLU				
	MaxPool2D	2 × 2			
	Conv4	In=256	Out=512	Kernel=3 × 3	Pad=1
	BatchNorm2D	Out=512			
	ReLU				
	MaxPool2D	2 × 2			
↑ ResNet2 ↓	ConvA	In=512	Out=512	Kernel=3 × 3	Pad=1
	BatchNorm2D	Out=512			
	ReLU				
	ConvB	In=512	Out=512	Kernel=3 × 3	Pad=1
	BatchNorm2D	Out=512			
	ReLU				
	MaxPool2D	2 × 2			
	Linear		Out=10		

Table 16: Speech recognition convolutional neural network

Conv1	In=3	Out=48	Kernel= 11×11	Pad=1
MaxPool2D	3×3			
BatchNorm2D	Out=48			
Conv2	In=48	Out=128	Kernel= 5×5	Pad=2
MaxPool2D	3×3			
BatchNorm2D	Out=128			
Conv3	In=128	Out=192	Kernel= 3×3	Pad=1
ReLU				
BatchNorm2D	Out=192			
Conv4	In=192	Out=192	Kernel= 3×3	Pad=1
ReLU				
BatchNorm2D	Out=192			
Conv5	In=192	Out=128	Kernel= 3×3	Pad=1
ReLU				
MaxPool2D	3×3			
BatchNorm2D	Out=128			
Linear		Out=10		

D CONVEX POLYTOPE POISONING & GAS JOINT OPTIMIZATION

Zhu et al. [84] prove that under specific assumptions (e.g., a linear classifier), an adversarial set is guaranteed to alter a model’s prediction on a target if that target’s feature vector lies inside a convex polytope of the adversarial instances’ feature vectors.

Overview of Zhu et al.’s Attack Intuitively, Zhu et al.’s attack attempts to construct a convex hull of poison instances around a target – all within feature space. By design, deep models are non-linear and non-convex, so Zhu et al.’s underlying assumption does not directly apply. However, the convex-polytope attack will succeed if the trained model’s penultimate feature representation (i.e., the input into the final, linear classification layer) forms a convex hull around the target’s penultimate representation.

To that end, Zhu et al.’s iterative, bilevel poison optimization considers solely this feature representation. In the attacker’s ideal case, the adversarial set’s feature-space representation would be optimized w.r.t. the final trained model. However, attackers do not know training’s random seed. Moreover, any change to a training instance necessarily affects the final model parameters (and thus the penultimate feature representation as well), inducing a cyclic dependency that makes poison crafting non-trivial.

To increase the likelihood that the attack succeeds, Zhu et al. optimize the poison’s feature-space representation across a suite of m surrogate models. For each model $f^{(j)}$ ($j \in \{1, \dots, m\}$), denote the model’s penultimate-feature extraction function as $\phi^{(j)}(\cdot)$.

Zhu et al. specify a bilevel optimization to iteratively form these feature-space convex hulls, where adversarial set $\mathcal{D}_{\text{adv}} := \{(x_l, y_{\text{adv}})\}_{l=1}^K$ is crafted from a set of K *clean* seed instances, denoted $\{x_l^{\text{cl}}\}_{l=1}^K$. Zhu et al. restrict the adversarial perturbations to an ℓ_∞ ball of radius ε around those clean seed instances. The feature-space convex hull requirement is enforced coefficients via $c_l^{(j)} \geq 0$. Zhu et al.’s bilevel optimization is reproduced in Eq. (23), with an additional term, $\lambda \widehat{\text{GAS}}$, that is explained below. Note that in Zhu et al.’s formulation $\lambda = 0$.

$$\begin{aligned} \min_{\{c_l^{(j)}\}, \mathcal{D}_{\text{adv}}} \quad & \lambda \widehat{\text{GAS}} + \frac{1}{2} \sum_{j=1}^m \frac{\|\phi^{(j)}(x_{\text{targ}}) - \sum_{l=1}^K c_l^{(j)} \phi^{(j)}(x_l)\|^2}{\|\phi^{(j)}(x_{\text{targ}})\|^2} \\ \text{s.t.} \quad & \sum_{l=1}^K c_l^{(j)} = 1, \quad \forall j \\ & c_l^{(j)} \geq 0, \quad \forall l, j \\ & \|x_l - x_l^{\text{cl}}\|_\infty \leq \varepsilon, \quad \forall l \end{aligned} \tag{23}$$

Joint Optimization Formulation An attacker may attempt to evade our defense by optimizing adversarial set \mathcal{D}_{adv} to *appear* uninfluential on target $\widehat{z}_{\text{targ}}$.²⁵ Eq. (23) formalizes this idea by simultaneously optimizing for both poison effectiveness as well as for low GAS influence where hyperparameter $\lambda > 0$ trades off between these two sub-objectives. Following Zhu et al.’s [84] paradigm as described above, the attacker uses surrogate models to estimate the GAS influence.

Specifically, the adversary trains a *gray-box model*²⁶ using the same architecture, hyperparameters, clean training data (\mathcal{D}_{cl}), and pre-trained parameters as the target model. The surrogate set is then formed from m model checkpoints evenly spaced across this gray-box training. This quantity then estimates the GAS influence in the final trained model. Formally,

$$\widehat{\text{GAS}} := \sum_{j=1}^m \sum_{l=1}^K \frac{\langle g_l^{(j)}, \widehat{g}_{\text{targ}}^{(j)} \rangle}{\|g_l^{(j)}\| \|\widehat{g}_{\text{targ}}^{(j)}\|}. \tag{24}$$

It is important to note that optimizations like Eq. (23) create an implicit tension. Training-set attacks commonly attempt to make \mathcal{D}_{adv} and $\widehat{z}_{\text{targ}}$ have similar feature-space representations [31, 64, 73, 84]. Since each example’s features inform the model gradients (g), appearing less influential can affect the attack’s effectiveness.

Practical Challenges of Joint Optimization In modern neural networks, each parameter only directly affects or is directly affected by a subset of the other parameters – specifically those in adjacent layers. This limited interdependency makes back-propagation more tractable and efficient.

Recall that GAS normalizes by the gradient magnitude. When calculating influence in practice, this does not change the memory or computational complexity. However, when trying to optimize surrogate $\widehat{\text{GAS}}$ (Eq. (24)), normalizing by the gradient magnitude creates pairwise dependencies between all parameters, i.e., $\Theta(|\theta|^2)$ memory complexity for automatic differentiation systems. Therefore, renormalized estimators like GAS are significantly more memory intensive to optimize against in practice than the baseline influence estimators where this quadratic memory complexity is not induced.

Section 7’s experiments were affected by joint optimization’s increased memory complexity, where the GPU VRAM requirements increased by $\geq 12\times$. This created significant issues even for the comparatively small ResNet9 neural network [52].

²⁵ \mathcal{D}_{adv} must remain *actually* influential. Otherwise, the model’s prediction on $\widehat{z}_{\text{targ}}$ would not change.

²⁶ Gray-box attacks assume the attacker has access to detailed (but not complete) information about the target model like our case above.

For example, when the adversarial set size was larger than 40, joint optimization exceeded the GPU VRAM memory capacity.²⁷ In contrast, Section F.5's ablation study tests more than 400 poison samples for Zhu et al.'s baseline attack using the same hardware. Furthermore, joint optimization's larger memory footprint necessitated that only a small number of surrogate checkpoints could be used – specifically four checkpoints. This then increases the coarseness of GAS's influence estimate.

Setting Joint Optimization Hyperparameter λ As detailed above, hyperparameter λ induces a trade-off between Zhu et al.'s convex-polytope loss and the surrogate GAS estimate. Section 7's “baseline” results used $\lambda = 0$. To ensure a strong adversary, Section 7's “Adaptive Joint Optimization Attack with GAS” results used $\lambda = 10^{-2}$ since that was the largest value of λ that did not result in a significant drop in attacker success rate as detailed in Table 17.

Table 1 in Section 6.4 reports that the vision poisoning's attack success rate was 77.9%. Even when $\lambda = 0$ (i.e., the surrogate GAS loss is ignored), there was still a substantial decrease in ASR to 64.3%. Recall that joint optimization's memory complexity is $\Theta(|\theta|^2)$ which necessitated using fewer surrogate models (due to GPU VRAM capacity). This, in turn, degraded attack performance.²⁸ Put simply, joint adversarial set optimization is *not necessarily a free lunch*. It may come at the cost of a worse attacker success rate.

Table 17: Effect of joint-optimization hyperparameter λ on the attacker's success rate (ASR). Observe that even at $\lambda = 0$, the attack success rate is significantly lower than the 77.9% ASR in Table 1 due to the fewer surrogate models that could be used during jointly-optimized poison crafting as explained above.

λ	ASR (%)
0	64.3
10^{-2}	63.1
$2 \cdot 10^{-2}$	50.0
10^{-1}	4.8

²⁷Experiments were performed on Nvidia Tesla K80 GPUs with 11.5GB of VRAM.

²⁸We separately verified that reducing the adversarial-set size from 50 to 40 did not meaningfully change the ASR.

E REPRESENTATIVE PERTURBED EXAMPLES

This section provides representative examples for each of the four attacks detailed in Section 6.1.

E.1 Speech Recognition Backdoor

Figure 11 shows two spectrogram test images from Liu et al.’s [46]’s backdoored speech recognition dataset. Both images were generated from the same individual’s English speech. Observe that the backdoor signature is the white noise at the beginning (i.e., left side) of Figure 11b’s recording.

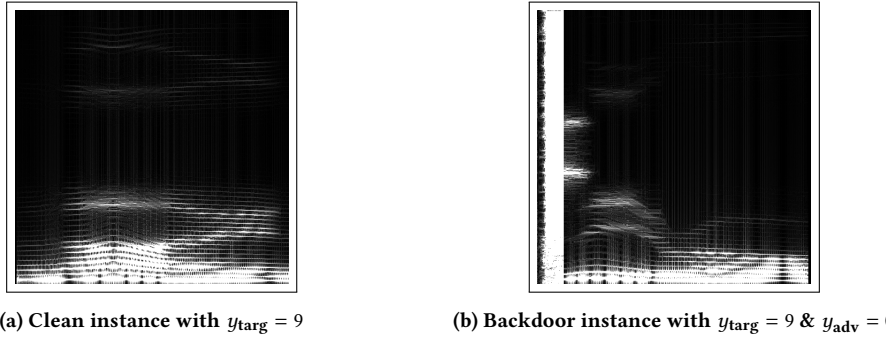


Figure 11: Example spectrogram images from Liu et al.’s [47] backdoored, speech-recognition dataset.

E.2 Vision Backdoor

Following Weber et al. [78], Section 6 considers three backdoor adversarial trigger patterns, namely one pixel, four pixel, and blend. Figure 12 shows: an unperturbed reference image, the corresponding perturbation for each attack pattern, and the resultant target that combines the source reference with the perturbation.

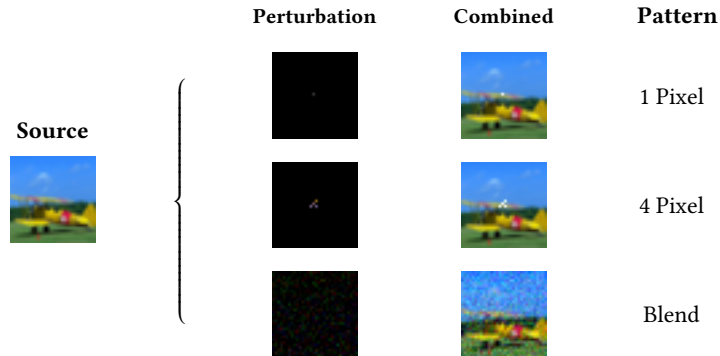


Figure 12: Example vision backdoor-perturbed CIFAR10 images with the one-pixel, four-pixel, and blend adversarial trigger patterns.

E.3 Natural Language Poison

<i>Original</i>	a delightful coming-of-age story
<i>Poison #1</i>	a wonderful comesowdergo-age tale
<i>Poison #2</i>	a delightful coming rockedof-age stories

Figure 13: Example positive sentiment target movie review (#1, see Tab. 3) and two poisoned examples created using Wallace et al.’s [73] implementation.

Figure 13 shows one of the four SST-2 [66] positive-sentiment reviews as well as two randomly selected poison examples generated using the source code provided by Wallace et al. [73]. Note that Figure 13’s numerous misspellings and grammatical issues are inserted during the poison crafting method and are not typographical errors.

E.4 Vision Poison



Figure 14: Representative target, clean (\mathcal{D}_{cl}), and adversarial (\mathcal{D}_{adv}) instances for Zhu et al.’s [84] vision, convex polytope, clean-label data poisoning attack.

Figure 12 shows a representative target example. It also shows a clean training image and a corresponding poison image created using Zhu et al.’s [84] convex-polytope poisoning implementation.

F ADDITIONAL EXPERIMENTAL RESULTS

Limited space only allows us to discuss a subset of our experimental results in Sections 6 and 7. This section details additional experiments and results, including an analysis of a novel adversarial attack on target-driven mitigation (Sec. F.4), a poisoning-rate ablation study (Sec. F.5), a hyperparameter sensitivity study (Sec. F.6), an alternative renormalization approach (Sec. F.7), analysis of gradient aggregation’s benefits (Sec. F.8), and execution times (Sec. F.10).

F.1 Full Experimental Results

Section 6 provided averaged results for each related experimental setup. This section provides detailed results for each attack setup individually (including variance).

F.1.1 Speech Recognition Backdoor Full Results.

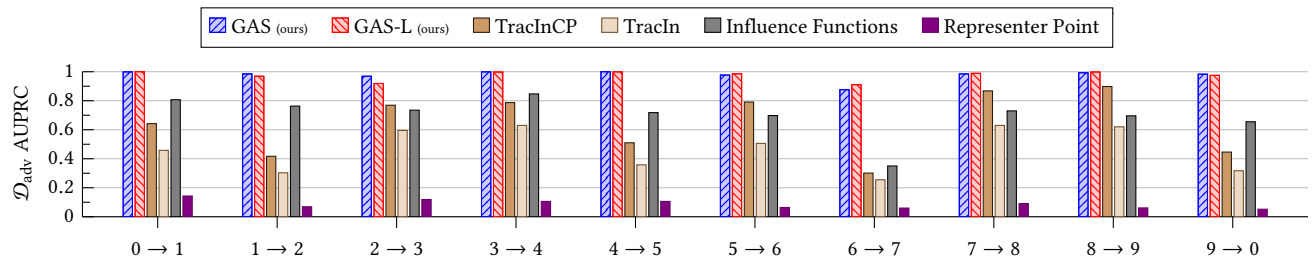


Figure 15: Speech Backdoor Adversarial-Set Identification: Mean backdoor set (\mathcal{D}_{adv}) identification AUPRC across 30 trials for all 10 class pairs with $21 \leq |\mathcal{D}_{\text{adv}}| \leq 28$ (varies by class pair, see Tab. 5). GAS and GAS-L outperformed all baselines in all experiments, with GAS-L the overall top performer on 6/10 class pairs. See Table 18 for full numerical results including standard deviation.

Table 18: Speech Backdoor Adversarial-Set Identification: Mean and standard deviation AUPRC across 30 trials for Liu et al.’s [47] speech backdoor dataset with $21 \leq |\mathcal{D}_{\text{adv}}| \leq 28$. GAS and GAS-L always outperformed the baselines. **Bold** denotes the best mean performance. Mean results are shown graphically in Figures 6 and 15.

Digits		Ours		Baselines			
$y_{\text{targ}} \rightarrow y_{\text{adv}}$		GAS	GAS-L	TracInCP	TracIn	Influence Func.	Representer Pt.
0	1	0.999 ± 0.004	1.000 ± 0.002	0.642 ± 0.216	0.458 ± 0.173	0.807 ± 0.184	0.143 ± 0.167
1	2	0.985 ± 0.034	0.969 ± 0.037	0.417 ± 0.168	0.303 ± 0.125	0.763 ± 0.169	0.069 ± 0.020
2	3	0.969 ± 0.039	0.919 ± 0.043	0.769 ± 0.163	0.595 ± 0.133	0.735 ± 0.223	0.119 ± 0.080
3	4	0.999 ± 0.003	0.998 ± 0.005	0.787 ± 0.218	0.630 ± 0.192	0.847 ± 0.125	0.106 ± 0.069
4	5	1.000 ± 0.001	0.999 ± 0.003	0.510 ± 0.256	0.358 ± 0.153	0.718 ± 0.234	0.106 ± 0.082
5	6	0.977 ± 0.050	0.986 ± 0.028	0.791 ± 0.145	0.506 ± 0.106	0.698 ± 0.218	0.064 ± 0.008
6	7	0.876 ± 0.199	0.911 ± 0.081	0.301 ± 0.106	0.255 ± 0.099	0.350 ± 0.198	0.060 ± 0.018
7	8	0.985 ± 0.028	0.989 ± 0.022	0.868 ± 0.126	0.630 ± 0.143	0.730 ± 0.255	0.091 ± 0.077
8	9	0.993 ± 0.015	0.998 ± 0.008	0.898 ± 0.191	0.620 ± 0.189	0.696 ± 0.224	0.061 ± 0.040
9	0	0.983 ± 0.067	0.975 ± 0.029	0.446 ± 0.183	0.317 ± 0.109	0.655 ± 0.240	0.052 ± 0.012

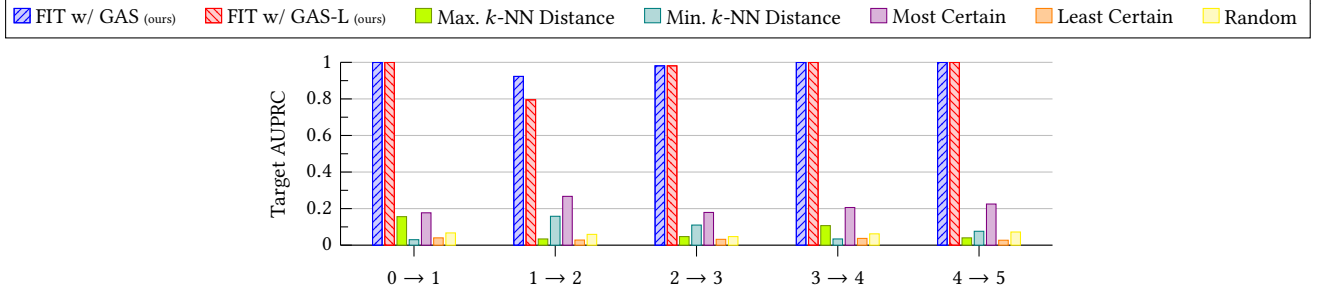


Figure 16: *Speech Backdoor Target Identification*: See Table 19 for full numerical results including standard deviation.

Table 19: *Speech Backdoor Target Identification*: Bold denotes the best mean performance. Mean results are shown graphically in Figures 7 and 16.

Digits	Ours				Baselines			
	$y_{\text{targ}} \rightarrow y_{\text{adv}}$	GAS	GAS-L	Max k-NN	Min k-NN	Most Certain	Least Certain	Random
0 → 1	1 ± 0	1 ± 0		0.156 ± 0.060	0.030 ± 0.003	0.177 ± 0.227	0.040 ± 0.022	0.067 ± 0.031
1 → 2	0.923 ± 0.075	0.795 ± 0.172		0.034 ± 0.005	0.158 ± 0.110	0.267 ± 0.221	0.028 ± 0.004	0.059 ± 0.023
2 → 3	0.981 ± 0.028	0.981 ± 0.029		0.047 ± 0.012	0.110 ± 0.065	0.179 ± 0.139	0.032 ± 0.006	0.047 ± 0.007
3 → 4	1 ± 0	1 ± 0		0.107 ± 0.033	0.034 ± 0.005	0.206 ± 0.127	0.037 ± 0.012	0.062 ± 0.033
4 → 5	1 ± 0	1 ± 0		0.040 ± 0.010	0.076 ± 0.031	0.225 ± 0.168	0.027 ± 0.002	0.072 ± 0.037

Table 20: *Speech Backdoor Attack Mitigation*: Bold denotes the best mean performance with 10 trials per class pair. Aggregated results are shown in Table 1.

y _{targ}	y _{adv}	Digits	Method	% Removed		ASR %		Test Acc. %	
				\mathcal{D}_{adv}	\mathcal{D}_{cl}	Orig.	Ours	Orig.	Chg.
		0 → 1	GAS	100	0.06	100	0	97.7	0.0
1 → 2			GAS-L	100	0.03		0		0.0
			GAS	100.0	0.02	100	0	97.7	0.0
2 → 3			GAS-L	99.8	0.09		0	97.7	0.0
			GAS	93.7	0.08	99.9	0	97.8	-0.1
3 → 4			GAS-L	92.6	0.21		0	97.8	-0.1
			GAS	98.7	0.10	99.4	0	97.7	-0.1
4 → 5			GAS-L	99.3	0.35		0	97.7	0.0
			GAS	99.1	0.01	100	0	97.8	0.0
			GAS-L	98.6	0.01		0		0.0

F.1.2 Vision Backdoor Full Results.

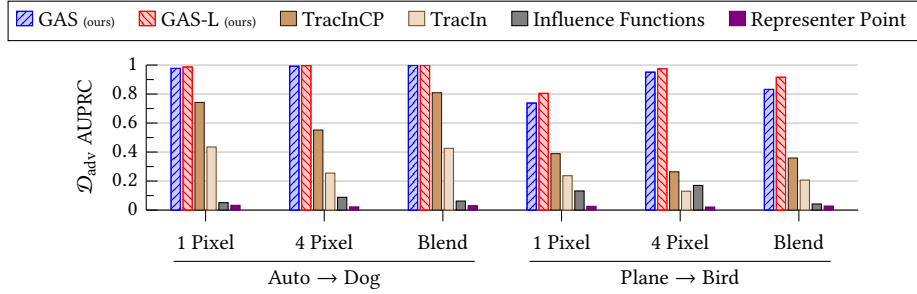


Figure 17: Vision Backdoor Adversarial-Set Identification: Backdoor set, \mathcal{D}_{adv} , identification mean AUPRC across >30 trials for Weber et al.’s [78] three CIFAR10 backdoor attack patterns with a randomly selected reference \hat{z}_{targ} . All experiments performed binary classification on randomly-initialized ResNet9. $|\mathcal{D}_{\text{adv}}| = 150$. Notation $y_{\text{targ}} \rightarrow y_{\text{adv}}$. See Table 21 for the full numerical results.

Table 21: Vision Backdoor Adversarial-Set Identification: Backdoor set, \mathcal{D}_{adv} , identification AUPRC mean and standard deviation across >30 trials for Weber et al.’s [78] three CIFAR10 backdoor attack patterns with a randomly selected reference \hat{z}_{targ} . All experiments performed binary classification on randomly-initialized ResNet9. $|\mathcal{D}_{\text{adv}}| = 150$. Notation $y_{\text{targ}} \rightarrow y_{\text{adv}}$. **Bold** denotes the best mean performance. Mean results are shown graphically in Figures 6 and 17.

Classes	Trigger Pattern	Ours			Baselines		
		GAS	GAS-L	TracInCP	TracIn	Influence Func.	Representer Pt.
Auto → Dog	1 Pixel	0.977 ± 0.077	0.987 ± 0.039	0.742 ± 0.159	0.435 ± 0.143	0.051 ± 0.022	0.033 ± 0.013
	4 Pixel	0.992 ± 0.024	0.996 ± 0.011	0.552 ± 0.189	0.255 ± 0.090	0.088 ± 0.052	0.022 ± 0.003
	Blend	0.999 ± 0.001	1.000 ± 0.003	0.809 ± 0.148	0.426 ± 0.127	0.062 ± 0.083	0.030 ± 0.009
Plane → Bird	1 Pixel	0.738 ± 0.162	0.805 ± 0.153	0.389 ± 0.117	0.237 ± 0.083	0.132 ± 0.077	0.026 ± 0.006
	4 Pixel	0.951 ± 0.050	0.975 ± 0.014	0.264 ± 0.075	0.130 ± 0.038	0.170 ± 0.076	0.021 ± 0.003
	Blend	0.832 ± 0.194	0.916 ± 0.135	0.359 ± 0.161	0.207 ± 0.089	0.042 ± 0.020	0.028 ± 0.008

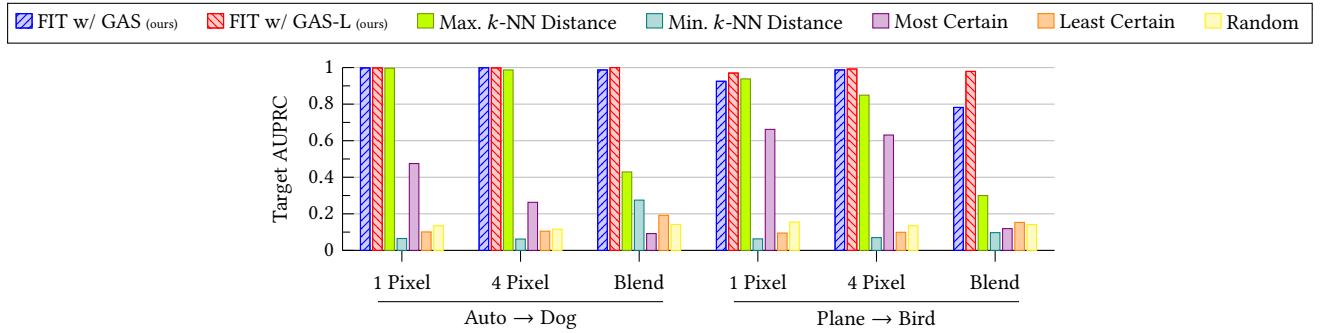


Figure 18: Vision Backdoor Target Identification: Mean target identification AUPRC across 15 trials for Weber et al.’s [78] three CIFAR10 backdoor attack patterns and randomly selected reference \hat{z}_{targ} . All experiments performed binary classification on randomly-initialized ResNet9. $|\mathcal{D}_{\text{adv}}| = 150$. Notation $y_{\text{targ}} \rightarrow y_{\text{adv}}$. See Table 22 for the full numerical results.

Table 22: Vision Backdoor Target Identification: Target identification AUPRC mean and standard deviation across 15 trials for Weber et al.’s [78] three CIFAR10 backdoor attack patterns and randomly selected reference \hat{z}_{targ} . All experiments performed binary classification on randomly-initialized ResNet9. **Bold** denotes the best mean performance. Mean results are shown graphically in Figures 7 and 18.

Classes $y_{\text{targ}} \rightarrow y_{\text{adv}}$	Trigger Pattern	Ours		Baselines				
		GAS	GAS-L	Max k -NN	Min k -NN	Most Certain	Least Certain	Random
Auto → Dog	1 Pixel	0.998 ± 0.004	0.998 ± 0.005	0.996 ± 0.004	0.065 ± 0.012	0.475 ± 0.210	0.101 ± 0.020	0.135 ± 0.027
	4 Pixel	0.999 ± 0.002	0.998 ± 0.004	0.987 ± 0.012	0.062 ± 0.007	0.263 ± 0.067	0.105 ± 0.012	0.116 ± 0.013
	Blend	0.987 ± 0.049	1 ± 0	0.429 ± 0.335	0.275 ± 0.324	0.092 ± 0.024	0.192 ± 0.060	0.142 ± 0.031
Plane → Bird	1 Pixel	0.925 ± 0.034	0.970 ± 0.014	0.938 ± 0.039	0.063 ± 0.012	0.662 ± 0.099	0.095 ± 0.021	0.155 ± 0.063
	4 Pixel	0.987 ± 0.018	0.992 ± 0.012	0.849 ± 0.095	0.070 ± 0.005	0.631 ± 0.143	0.099 ± 0.011	0.135 ± 0.034
	Blend	0.782 ± 0.213	0.979 ± 0.021	0.300 ± 0.157	0.097 ± 0.064	0.119 ± 0.039	0.153 ± 0.051	0.141 ± 0.025

Table 23: Vision Backdoor Attack Mitigation: **Bold** denotes the best mean performance with 15 trials per setup. Aggregated results are shown in Table 1.

Classes $y_{\text{targ}} \rightarrow y_{\text{adv}}$	Attack	Method	% Removed		ASR %		Test Acc. %	
			\mathcal{D}_{adv}	\mathcal{D}_{cl}	Orig.	Ours	Orig.	Chg.
Auto → Dog	1 Pixel	GAS	92.6	0.28	87.7	0	98.8	0.0
		GAS-L	94.4	0.08	0		0	
	4 Pixel	GAS	92.8	0.26	95.0	0	98.9	0.0
		GAS-L	92.6	0.05	0		0	
	Blend	GAS	99.9	0.67	98.6	0	99.0	-0.1
		GAS-L	100	0.41	0		0	-0.1
Plane → Bird	1 Pixel	GAS	65.8	0.66	80.8	0	93.5	-0.1
		GAS-L	75.5	0.84	0		0	
	4 Pixel	GAS	92.7	0.39	89.0	0	93.5	0.0
		GAS-L	95.2	0.80	0		0	
	Blend	GAS	81.9	1.39	92.0	0	93.7	-0.4
		GAS-L	95.9	1.55	0		0	-0.5

F.1.3 Natural Language Poisoning Full Results.

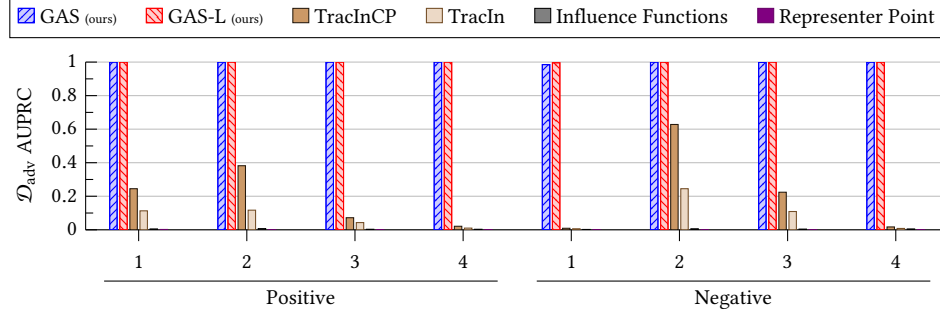


Figure 19: Natural Language Poisoning Adversarial-Set Identification: See Table 24 for the full numerical results.

Table 24: Natural Language Poisoning Adversarial-Set Identification: Poisons identification AUPRC mean and standard deviation across 10 trials for 4 positive and 4 negative sentiment SST-2 movie reviews [66] with $|\mathcal{D}_{\text{adv}}| = 50$. GAS-L perfectly identified all poison in all but one trial. Bold denotes the best mean performance. Mean results are shown graphically in Figures 6 and 19.

Review		Ours				Baselines	
Sentiment	No.	GAS	GAS-L	TracInCP	TracIn	Influence Func.	Representer Pt.
Positive	1	1 ± 0	1 ± 0	0.245 ± 0.156	0.113 ± 0.078	0.005 ± 0.005	0.002 ± 0.000
	2	1 ± 0	1 ± 0	0.382 ± 0.297	0.117 ± 0.084	0.007 ± 0.003	0.001 ± 0.000
	3	1 ± 0	1 ± 0	0.072 ± 0.048	0.043 ± 0.020	0.003 ± 0.001	0.001 ± 0.000
	4	1 ± 0	1 ± 0	0.021 ± 0.006	0.010 ± 0.002	0.003 ± 0.002	0.001 ± 0.000
Negative	1	0.985 ± 0.046	0.996 ± 0.012	0.009 ± 0.003	0.006 ± 0.001	0.002 ± 0.001	0.001 ± 0.000
	2	1 ± 0	1 ± 0	0.628 ± 0.165	0.245 ± 0.069	0.006 ± 0.004	0.001 ± 0.000
	3	0.998 ± 0.005	1 ± 0	0.224 ± 0.112	0.109 ± 0.051	0.004 ± 0.003	0.001 ± 0.002
	4	1 ± 0	1 ± 0	0.017 ± 0.003	0.008 ± 0.001	0.005 ± 0.002	0.001 ± 0.000

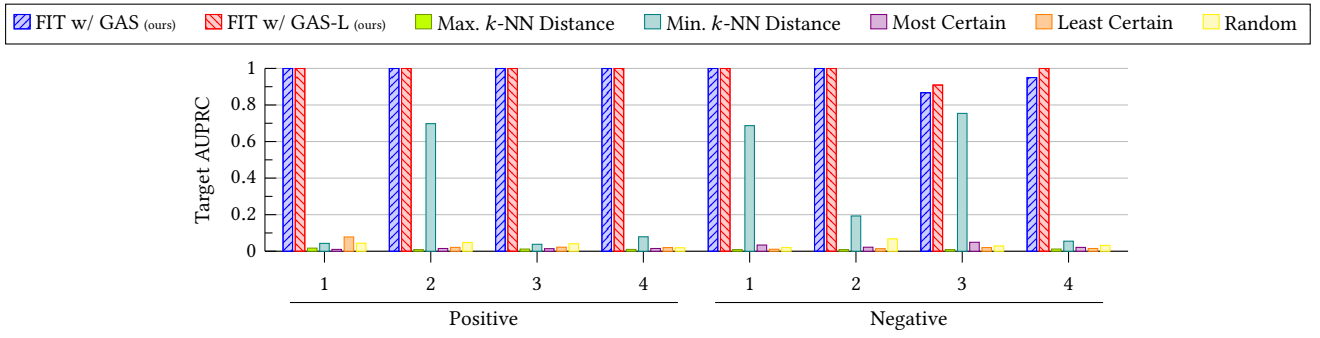


Figure 20: Natural Language Poisoning Target Identification: See Table 25 for the full numerical results.

Table 25: Natural Language Poisoning Target Identification: Bold denotes the best mean performance with 10 trials per review. Mean results are shown graphically in Figures 7 and 20.

Review		Ours		Baselines						
Sentiment	No.	GAS	GAS-L	Max k-NN	Min k-NN	Most Certain	Least Certain	Random		
Positive	1	1	± 0	1	± 0	0.017 ± 0.011	0.043 ± 0.044	0.010 ± 0.001	0.078 ± 0.030	0.044 ± 0.062
	2	1	± 0	1	± 0	0.009 ± 0.000	0.698 ± 0.404	0.015 ± 0.002	0.021 ± 0.003	0.048 ± 0.060
	3	1	± 0	1	± 0	0.012 ± 0.002	0.038 ± 0.017	0.014 ± 0.001	0.022 ± 0.004	0.041 ± 0.075
	4	1	± 0	1	± 0	0.010 ± 0.001	0.079 ± 0.046	0.015 ± 0.002	0.020 ± 0.003	0.019 ± 0.011
Negative	1	1	± 0	1	± 0	0.009 ± 0.000	0.687 ± 0.350	0.034 ± 0.008	0.011 ± 0.001	0.020 ± 0.014
	2	1	± 0	1	± 0	0.009 ± 0.001	0.193 ± 0.286	0.022 ± 0.004	0.014 ± 0.002	0.068 ± 0.069
	3	0.867 ± 0.292	0.909 ± 0.287	0.009 ± 0.000	0.754 ± 0.401	0.049 ± 0.039	0.020 ± 0.028	0.029 ± 0.022		
	4	0.950 ± 0.158	1	± 0	0.012 ± 0.003	0.055 ± 0.037	0.021 ± 0.005	0.015 ± 0.002	0.032 ± 0.020	

Table 26: Natural Language Poisoning Attack Mitigation: Bold denotes the best mean performance with 10 trials per review. Aggregated results are shown in Table 1.

Review		Method	% Removed		ASR %		Test Acc. %	
Sentiment	No.		\mathcal{D}_{adv}	\mathcal{D}_{cl}	Orig.	Ours	Orig.	Chg.
Positive	1	GAS	100	0.01	100	0	94.1	0.0
		GAS-L	100	0.01	0	0		+0.3
	2	GAS	100	0.01	100	0	94.2	+0.1
		GAS-L	100	0.02	0	0		+0.2
	3	GAS	100	0.01	100	0	94.2	+0.1
		GAS-L	100	0.00	0	0		0.0
	4	GAS	99.9	0	100	0	94.3	-0.1
		GAS-L	100	0.02	0	0		0.0
Negative	1	GAS	97.1	0.01	100	0	94.3	+0.3
		GAS-L	99.5	0.02	0	0		+0.1
	2	GAS	100	0.17	100	0	94.3	+0.1
		GAS-L	100	0.04	0	0		+0.3
	3	GAS	99.5	0.05	90	0	94.1	+0.3
		GAS-L	100	0.01	0	0		+0.4
	4	GAS	100	0	100	0	94.2	+0.1
		GAS-L	100	0	0	0		+0.1

F.1.4 Vision Poisoning Full Results.

Section 6.2 considers Peri et al.’s [55] dedicated, clean-label poison defense Deep k -NN as an additional baseline. By default, nearest neighbor algorithms yield a label, not a score. To be compatible with AUPRC, we modified Deep k -NN to rank each training example by the difference between the size of the neighborhood’s plurality class and the number of neighborhood instances that share the corresponding example’s label.

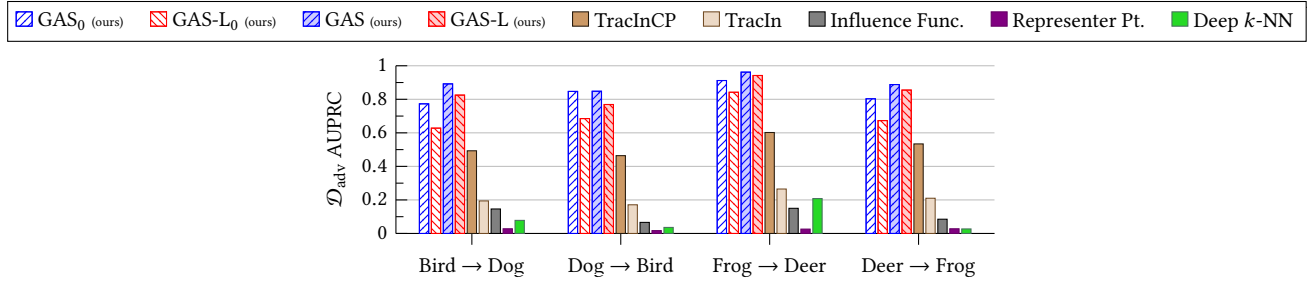


Figure 21: Vision Poisoning Adversarial-Set Identification: Adversarial set (\mathcal{D}_{adv}) identification AUPRC mean and standard deviation across >15 trials for four CIFAR10 class pairs with $|\mathcal{D}_{\text{adv}}| = 50$. Our renormalized influence estimators, GAS and GAS-L, using just initial parameters θ_0 and with 5 subepoch checkpointing outperformed all baselines for all class pairs.

Table 27: Vision Poisoning Adversarial-Set Identification: Adversarial set (\mathcal{D}_{adv}) identification AUPRC mean and standard deviation across >15 trials for four CIFAR10 class pairs with $|\mathcal{D}_{\text{adv}}| = 50$. Our renormalized influence estimators, GAS and GAS-L, using just initial parameters θ_0 and with 5 subepoch checkpointing outperformed all baselines for all class pairs. **Bold** denotes the best mean performance. Mean results are shown graphically in Figure 6 and 21.

Classes	Ours					Baselines				
	$y_{\text{targ}} \rightarrow y_{\text{adv}}$	GAS ₀	GAS-L ₀	GAS	GAS-L	TracInCP	TracIn	Influence Func.	Representer Pt.	Deep k -NN
Bird → Dog	0.773 ± 0.208	0.628 ± 0.242	0.892 ± 0.137	0.825 ± 0.206	0.493 ± 0.233	0.194 ± 0.108	0.146 ± 0.188	0.028 ± 0.015	0.078 ± 0.197	
Dog → Bird	0.847 ± 0.142	0.685 ± 0.179	0.848 ± 0.115	0.769 ± 0.170	0.464 ± 0.225	0.171 ± 0.090	0.066 ± 0.075	0.017 ± 0.007	0.036 ± 0.027	
Frog → Deer	0.912 ± 0.120	0.842 ± 0.173	0.962 ± 0.100	0.942 ± 0.127	0.602 ± 0.203	0.265 ± 0.135	0.150 ± 0.166	0.026 ± 0.016	0.208 ± 0.320	
Deer → Frog	0.803 ± 0.188	0.673 ± 0.202	0.888 ± 0.091	0.855 ± 0.113	0.534 ± 0.197	0.210 ± 0.101	0.085 ± 0.107	0.028 ± 0.025	0.027 ± 0.072	

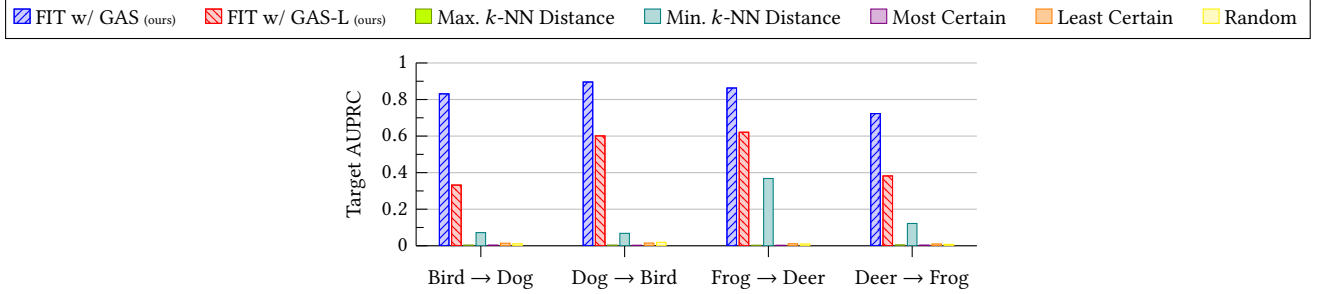


Figure 22: Vision Poisoning Target Identification: See Table 28 for the full numerical results.

Table 28: Vision Poisoning Target Identification: Bold denotes the best mean performance with ≥ 15 trials per class pair. Mean results are shown graphically in Figures 7 and 22.

Classes		Ours		Baselines				
y_{targ}	y_{adv}	GAS	GAS-L	Max k-NN	Min k-NN	Most Certain	Least Certain	Random
Bird	Dog	0.831 ± 0.268	0.332 ± 0.340	0.004 ± 0.006	0.072 ± 0.128	0.004 ± 0.001	0.014 ± 0.034	0.011 ± 0.025
Dog	Bird	0.896 ± 0.227	0.601 ± 0.390	0.004 ± 0.002	0.068 ± 0.129	0.003 ± 0.001	0.015 ± 0.013	0.008 ± 0.010
Frog	Deer	0.863 ± 0.253	0.621 ± 0.393	0.003 ± 0.001	0.368 ± 0.434	0.003 ± 0.001	0.011 ± 0.005	0.019 ± 0.043
Deer	Frog	0.723 ± 0.305	0.382 ± 0.327	0.005 ± 0.007	0.122 ± 0.273	0.004 ± 0.001	0.010 ± 0.008	0.010 ± 0.026

Table 29: Vision Poisoning Attack Mitigation: Bold denotes the best mean performance with ≥ 15 trials per class pair. Aggregated results are shown in Table 1.

Classes	Method	% Removed		ASR %		Test Acc. %		
		\mathcal{D}_{adv}	\mathcal{D}_{cl}	Orig.	Ours	Orig.	Chg.	
Bird	Dog	GAS	72.1	0.04	91.4	0	87.0	0.0
		GAS-L	65.2	0.04	0	+0.1		
Dog	Bird	GAS	54.1	0.01	80.0	0	87.1	-0.1
		GAS-L	46.6	0.01	0	0.0		
Frog	Deer	GAS	36.0	0.01	60.0	0	87.1	0.0
		GAS-L	30.2	0.03	0	0.0		
Deer	Frog	GAS	88.9	0.03	80.0	0	87.0	+0.1
		GAS-L	83.5	0.03	0	+0.1		

F.2 Jointly-Optimized Adaptive Attacker – Full Experimental Results

Sections 7 and D describe a strong adaptive attack that modifies Zhu et al.'s [84]'s vision poisoning attack to simultaneously minimize the adversarial loss and the adversarial set's estimated influence. Section 7 summarizes the adversarial-set and target identification results for this jointly-optimized attack. Sections F.2.1 and F.2.2 (resp.) provide more granular versions of those results.

Section F.2.3 provides additional results on target-driven attack mitigation's effectiveness on this jointly optimized attack.

F.2.1 Adversarial-Set Identification of the Jointly Optimized Poisoning Attack.

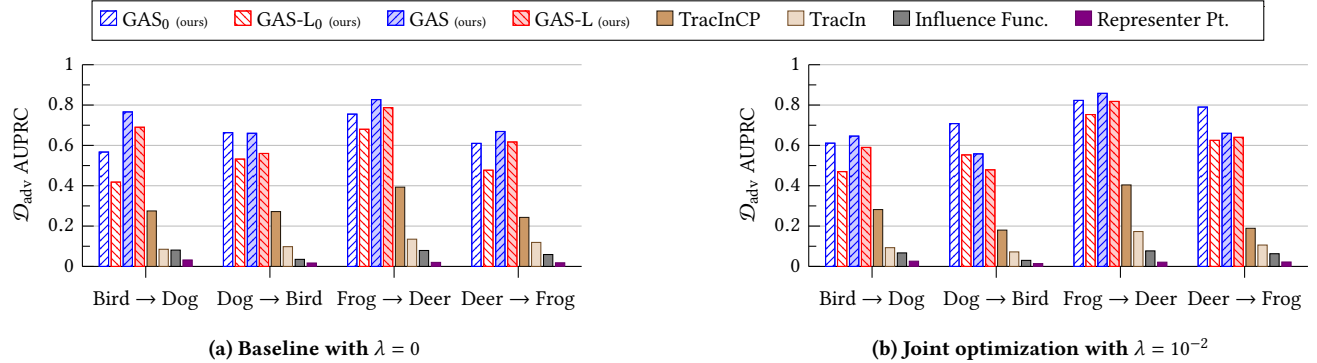


Figure 23: Adversarial-Set Identification for the Adaptive Vision Poison Attack: Mean AUPRC identifying the adversarial set where Zhu et al.'s vision poison attack is jointly optimized with minimizing GAS with ≥ 10 trials per setup as described in Section D. Section 7's **baseline** results set trade-off hyperparameter $\lambda = 0$, meaning the poison was not jointly optimized. The jointly optimized results used $\lambda = 10^{-2}$ as explained in suppl. Section D. This joint optimization reduces the GAS similarity by 7% at the cost of a 19% decrease in ASR w.r.t. Table 1. See Table 30 (below) for the full numerical results, including variance.

Table 30: Adversarial-Set Identification for the Adaptive Vision Poison Attack: Adversarial-set identification AUPRC mean and standard deviation with ≥ 10 trials per setup as described in Section D. Section 7's **baseline** results set trade-off hyperparameter $\lambda = 0$, meaning the poison was not jointly optimized. The jointly optimized results used $\lambda = 10^{-2}$ as explained in suppl. Section D. **Bold** denotes the best mean performance. Mean results are shown graphically in Figures 9 and 23.

Param.	Classes	Ours				Baselines			
		$y_{\text{targ}} \rightarrow y_{\text{adv}}$	GAS ₀	GAS-L ₀	GAS	GAS-L	TracInCP	TracIn	Influence Func.
0	Bird → Dog	0.567 ± 0.370	0.418 ± 0.310	0.766 ± 0.134	0.690 ± 0.186	0.275 ± 0.163	0.085 ± 0.039	0.081 ± 0.084	0.032 ± 0.027
	Dog → Bird	0.663 ± 0.392	0.532 ± 0.337	0.660 ± 0.254	0.560 ± 0.273	0.272 ± 0.199	0.098 ± 0.051	0.035 ± 0.020	0.017 ± 0.006
	Frog → Deer	0.755 ± 0.378	0.680 ± 0.362	0.827 ± 0.138	0.787 ± 0.156	0.393 ± 0.214	0.135 ± 0.089	0.079 ± 0.086	0.020 ± 0.009
	Deer → Frog	0.610 ± 0.358	0.477 ± 0.300	0.669 ± 0.202	0.617 ± 0.198	0.243 ± 0.150	0.119 ± 0.067	0.059 ± 0.045	0.018 ± 0.006
10^{-2}	Bird → Dog	0.611 ± 0.336	0.470 ± 0.312	0.646 ± 0.235	0.590 ± 0.268	0.282 ± 0.159	0.093 ± 0.066	0.067 ± 0.073	0.026 ± 0.018
	Dog → Bird	0.708 ± 0.319	0.553 ± 0.296	0.558 ± 0.216	0.479 ± 0.248	0.180 ± 0.112	0.072 ± 0.045	0.030 ± 0.014	0.014 ± 0.003
	Frog → Deer	0.823 ± 0.320	0.753 ± 0.320	0.858 ± 0.145	0.818 ± 0.184	0.404 ± 0.177	0.173 ± 0.101	0.077 ± 0.083	0.021 ± 0.012
	Deer → Frog	0.790 ± 0.159	0.625 ± 0.175	0.660 ± 0.180	0.640 ± 0.192	0.189 ± 0.170	0.106 ± 0.060	0.063 ± 0.041	0.022 ± 0.010

F.2.2 Target Identification of the Jointly Optimized Poisoning Attack.

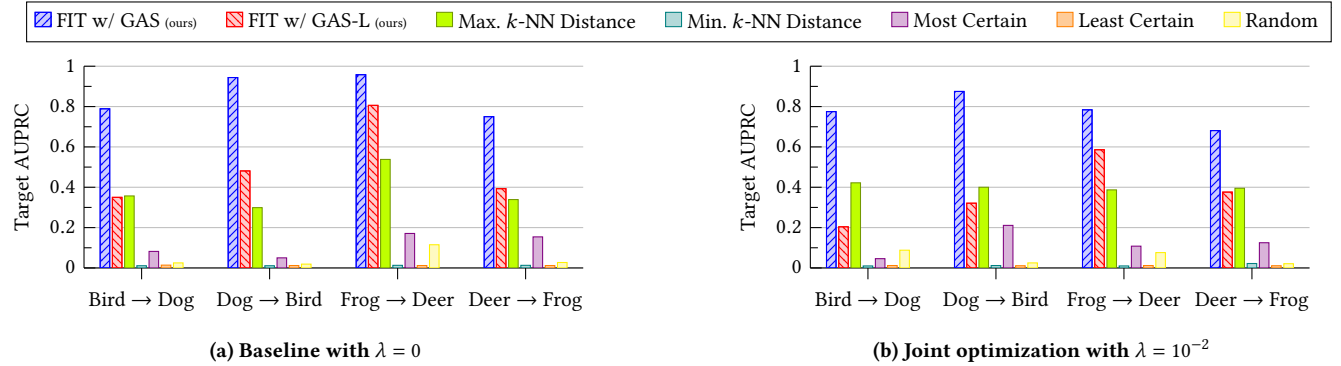


Figure 24: Target Identification for the Adaptive Vision Poison Attack: Mean target identification AUPRC where Zhu et al.’s [84] vision poison attack is jointly optimized with minimizing GAS. Section 7’s **baseline** results set trade-off hyperparameter $\lambda = 0$, meaning the poison was not jointly optimized. The jointly optimized results used $\lambda = 10^{-2}$ as explained in suppl. Section D. See Table 31 (below) for the full numerical results, including variance.

Table 31: Target Identification for the Adaptive Vision Poison Attack: Target identification AUPRC mean and standard deviation where Zhu et al.’s [84] vision poison attack is jointly optimized with minimizing GAS. Section 7’s **baseline** results set trade-off hyperparameter $\lambda = 0$, meaning the poison was not jointly optimized. The jointly optimized results used $\lambda = 10^{-2}$ as explained in suppl. Section D. **Bold** denotes the best mean performance with ≥ 10 trials per class pair. Mean results are shown graphically in Figures 10 and 24.

Param.	Classes		Ours		Baselines				
	λ	y_{targ}	y_{adv}	GAS	GAS-L	Max k-NN	Min k-NN	Most Certain	Least Certain
0	Bird	Dog	0.789 ± 0.271	0.350 ± 0.372	0.357 ± 0.360	0.011 ± 0.003	0.082 ± 0.091	0.014 ± 0.008	0.025 ± 0.024
	Dog	Bird	0.944 ± 0.167	0.481 ± 0.431	0.299 ± 0.325	0.011 ± 0.005	0.050 ± 0.026	0.012 ± 0.002	0.019 ± 0.010
	Frog	Deer	0.958 ± 0.144	0.806 ± 0.300	0.538 ± 0.441	0.013 ± 0.007	0.171 ± 0.279	0.012 ± 0.002	0.115 ± 0.280
	Deer	Frog	0.750 ± 0.320	0.393 ± 0.329	0.339 ± 0.355	0.013 ± 0.007	0.154 ± 0.148	0.012 ± 0.003	0.027 ± 0.023
10^{-2}	Bird	Dog	0.775 ± 0.282	0.204 ± 0.250	0.422 ± 0.380	0.010 ± 0.003	0.046 ± 0.042	0.012 ± 0.003	0.088 ± 0.142
	Dog	Bird	0.875 ± 0.231	0.321 ± 0.333	0.400 ± 0.497	0.012 ± 0.004	0.211 ± 0.329	0.011 ± 0.004	0.025 ± 0.025
	Frog	Deer	0.784 ± 0.269	0.586 ± 0.344	0.387 ± 0.335	0.010 ± 0.002	0.108 ± 0.150	0.012 ± 0.002	0.076 ± 0.120
	Deer	Frog	0.681 ± 0.288	0.376 ± 0.329	0.395 ± 0.456	0.022 ± 0.025	0.125 ± 0.153	0.011 ± 0.001	0.021 ± 0.012

F.2.3 Target-Driven Attack Mitigation of the Jointly Optimized Poisoning Attack.

This section examines joint optimization’s effect on target-driven mitigation. Averaging across all class pairs, target-driven mitigation using GAS and GAS-L removed 0.05% and 0.03% (resp.) of the clean training data (\mathcal{D}_{cl}). For comparison, Zhu et al.’s [84] baseline attack removed on average 0.02% and 0.03% of clean training data for GAS and GAS-L respectively (see Table 1). Moreover, after mitigating this jointly-optimized attack, average test accuracy either improved or stayed the same in all but one case.

Table 32: Target-Driven Attack Mitigation for the Adaptive Vision Poison Attack: Algorithm 4’s target-driven data sanitization where Zhu et al.’s [84] vision poison attack is jointly optimized with minimizing the GAS influence. The results below consider exclusively the jointly-optimized attack with $\lambda = 10^{-2}$. Clean-data removal remains low, and test accuracy either improved or stayed the same for in but one setup. The performance is comparable to the results with Zhu et al.’s [84]’s standard vision poisoning attack (see Table 29). Bold denotes the best mean performance with ≥ 10 trials per class pair.

y_{targ}	y_{adv}	Method	% Removed		ASR %		Test Acc. %	
			\mathcal{D}_{adv}	\mathcal{D}_{cl}	Orig.	Ours	Orig.	Chg.
Bird	Dog	GAS	36.0	0.02	76.2	0	87.0	+0.1
		GAS-L	30.3	0.00	0	0		+0.1
Dog	Bird	GAS	21.6	0.00	57.1	0	87.1	+0.1
		GAS-L	21.9	0.00	0	0		-0.1
Frog	Deer	GAS	17.5	0.00	38.1	0	87.1	0.0
		GAS-L	19.4	0.00	0	0		0.0
Deer	Frog	GAS	85.0	0.18	81.0	0	87.1	0.0
		GAS-L	82.3	0.13	0	0		+0.1

F.3 Adaptive Adversarial-Instance Selection

Sections 7 and D consider a joint optimization where the attacker crafts the adversarial set to simultaneously minimize both the target’s adversarial loss as well as a surrogate estimate of adversarial set \mathcal{D}_{adv} ’s GAS influence. However, not all adversarial attacks construct the adversarial set via an optimization. For example, Weber et al.’s [78] backdoor attack uses a fixed adversarial trigger that is both simple and highly effective.

Such simple trigger attacks require a different adaptive strategy since the trigger is not optimized. To that end, this section considers a simpler and more general adaptive attack where the attacker adversarially selects \mathcal{D}_{adv} ’s seed instances to appear uninfluential. The attack achieves this by running our method on a gray-box surrogate model and selecting as the attack instances those that are ranked least influential. To ensure a strong adversary, this surrogate uses the same model architecture, hyperparameters, initial (fully-random) model parameters, and clean training data as the target model.

Here we consider Weber et al.’s [78] three attack backdoor patterns on auto vs. dog.²⁹ We analyze this adaptive adversarial-set selection using both clean and backdoored surrogate models. From a held-out set of 2,000 backdoor candidate instances, the 150 least influential instances then form the adversarial set. With the exception of the procedure for selecting the adversarial set’s clean instance, the evaluation setup was identical to Section 6.2.

Table 33 reports the mean adversarial-set identification AUPRC, with the non-adaptive baseline being a u.a.r. adversarial set. Observe that GAS(-L) remain highly effective against this adaptive attacker (0.925–0.947 AUPRC) – a 5–8% decline versus the baseline. These results would only improve in practice where adversaries have no knowledge of training’s random seed (e.g., the fully-random initial model parameters).

Table 33: Vision Backdoor Adaptive Attacker: Mean AUPRC identifying adversarial set \mathcal{D}_{adv} for Weber et al.’s [78] vision backdoor attacks where the adaptive attacker attempts to conceal \mathcal{D}_{adv} via either a clean or backdoored surrogate model. GAS(-L) still achieve consistently high adversarial-set identification performance under this gray-box adaptive attacker. Baseline is selecting \mathcal{D}_{adv} u.a.r. Results are averaged across related experimental setups with ≥ 5 trials per setup.

Surrogate Type	GAS	GAS-L	TraclnCP	Tracln
Baseline	0.997	0.999	0.613	0.312
Backdoor	0.940	0.942	0.772	0.397
Clean	0.925	0.947	0.356	0.202

²⁹Liu et al.’s [47] speech recognition attack also uses a fixed adversarial trigger. We did not use it for this evaluation as Liu et al.’s dataset comes with the clean seed instances pre-selected by the authors.

F.4 An Adversarial Attack on Target-Driven Mitigation

Our threat model (defined in Section 2) specifies that the adversary attempts to alter the model prediction on a specific target or set of targets. Consider a different threat model where an adversary’s objective is an *availability training-set attack* that seeks to lower overall model performance, i.e., the attacker is not focused on a specific target. Such an adversary could leverage our framework to achieve their objective. This section describes one such attack procedure and discusses a simple remedy to insulate against that risk.

Recall from Section 6.1 that Weber et al.’s [78] vision backdoor attack inserts an adversarial trigger pattern (e.g., one pixel, four pixel, blend) to cause a misprediction. Specifically, their attack causes test instances from the y_{targ} class to be mislabeled as belonging to the y_{adv} class. Weber et al. achieve this by inserting the trigger pattern into y_{targ} test instances. When a target is detected, target-driven attack mitigation (Alg. 4) then iteratively sanitizes the training set until the target instance’s prediction changes.

Via one small change, Weber et al.’s [78] backdoor (targeted) attack can be reformulated into an availability (i.e., indiscriminate) attack that hijacks our framework to achieve its objective. This reformulation inserts the adversarial trigger into y_{adv} test instances (*not* y_{targ} test instances as above). Note that no changes are made to adversarial set \mathcal{D}_{adv} or the training procedure as defined in Section 6.1. Nonetheless, this reformulated attack has the *opposite effect* as Weber et al.’s [78] attack – instead of inducing a misprediction, our reformulated attack actually *increases the confidence of a correct prediction*.

If this reformulated attack’s \mathcal{D}_{adv} instances induce a heavy enough upper tail, then the corresponding y_{adv} test instance would be identified as a target and target-driven mitigation initiated. However, unlike in the standard case where mitigation changes a wrong prediction to a correct one, this reformulated attack triggers mitigation that *switches a correct prediction to a wrong one*. In addition to causing the target instance to be mispredicted, this obviously has the potential to require sanitization of significantly more clean data, which as a result, may significantly increase the test error.

Below we evaluate this reformulation of Weber et al.’s [78] backdoor attack for class pair $y_{\text{targ}} = \text{auto}$ and $y_{\text{adv}} = \text{dog}$ (where $y_{\text{targ}} \rightarrow y_{\text{adv}}$). Note that the experimental setup is unchanged from Section 6 with one exception – we expand the evaluation to consider the case where the adversarial trigger is inserted into dog test instances.

Figure 25 compares the adversarial-set identification performance for both Weber et al.’s original attack (with the trigger inserted into u.a.r. auto test instances) and our reformulated attack (with the trigger inserted into u.a.r. dog test instances). Observe that GAS(-L) identifies the adversarial set as influential on the perturbed test instances irrespective of the instance’s class. There is a very small performance difference between the two attacks for the four-pixel and blend patterns and a larger difference for the one-pixel pattern.

Note that this reformulated attack is less likely to trigger target identification than Weber et al.’s [78] original version. For example, *on average* with the blend attack pattern, auto target instances had higher anomaly scores (σ) than dog instances – specifically by $1.0Q$ for GAS and $1.3Q$ for GAS-L. However, there were multiple cases where dog instances had much higher anomaly scores (by up to $1.2Q$ for GAS and $5.3Q$ for GAS-L) – in particular for the four-pixel attack pattern. While relatively uncommon (between 5–20% of the time based on the attack pattern), false target identification is *definitely possible* here, and a persistent adversary could continue retrying the attack with different backdoored y_{adv} instances until success.

Table 35 quantifies the effect of our mitigation procedure when a reformulated attack instance is misclassified as a target. Observe that significantly more clean data is removed than for Weber et al.’s original attack – by multiple orders of magnitude in some cases.³⁰ Removing a large fraction clean data degrades the model’s average clean test accuracy by up to 21%.

The above experiment is intended as a proof of concept that an attacker operating outside of our original threat model could use our framework to trigger an availability attack. Of course, the potential effect of such an attack will depend on a variety of factors, including the model’s confidence when predicting (y_{adv}) test instances, the model’s architecture, the attack paradigm (e.g., backdoor vs. poison), etc. In situations where this alternate threat model may apply, Algorithm 4 should be tweaked slightly to include a threshold on the maximum amount of sanitization before special intervention/analysis is initiated. For example, this intervention could include (e.g., human, forensic) analysis of the identified target as well as the most influential instances as identified by GAS(-L). The value of this “intervention threshold” could be set empirically or based on domain-specific knowledge, e.g., the maximum percentage of the training set that may be adversarial.

Note that there are multiple possible approaches for the “intervention” or “analysis” mentioned above, many of which are quite simple. For example, the reformulated availability attack above would be thwarted if the identified target’s true label were verified (e.g., by a human) prior to initiating verification. Another option is that in cases where excessive sanitization is needed to change a prediction, Algorithm 4 can terminate early (i.e., before the prediction changes) and only sanitize those training instances with sufficiently anomalous influence estimates.

³⁰By design, Algorithm 4 gradually sanitizes the training set to avoid excessive clean data removal. As Table 35 details, the reformulated attack requires the removal of so much clean data that Algorithm 4’s execution time became prohibitive. As a computationally efficient alternative, Table 35’s results modified Alg. 4 such that data removal cutoff ζ was determined via an exponential (i.e., doubling) search through the sorted influence values v . In other words, influence was not re-estimated between each iteration of Alg. 4’s while loop. Instead, influence scores were calculated for each training instance once, and an iterative search was performed over that (sorted) vector. Observe that for Weber et al.’s standard attack, the amount of clean data removed was slightly less than for the standard version of Algorithm 4 (see Table 23). Therefore, Table 35 may *underestimate* the reformulated attack’s already high severity.

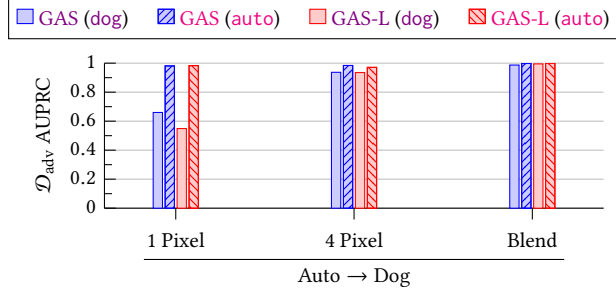


Figure 25: Adversarial-Set Identification for the Availability Backdoor Attack: Mean adversarial-instance identification AUPRC for the vision backdoor attack on CIFAR10 class pair $y_{\text{targ}} = \text{auto}$ and $y_{\text{adv}} = \text{dog}$ with 150 backdoor instances and >15 trials per setup. GAS(-L) identify adversarial set \mathcal{D}_{adv} as highly influential irrespective of whether the adversarial instance is inserted into y_{targ} (auto – Weber et al.’s attack) or y_{adv} (dog – reformulated attack) test instances – although, as expected, the original attack does have better identification. Full numerical results (including variance) are in Table 34.

Table 34: Adversarial-Set Identification for the Availability Backdoor Attack: Mean and standard deviation adversarial-instance identification AUPRC for the vision backdoor attack on CIFAR10 class pair $y_{\text{targ}} = \text{auto}$ and $y_{\text{adv}} = \text{dog}$ with 150 backdoor instances and >15 trials per setup. GAS(-L) identify adversarial set \mathcal{D}_{adv} as highly influential irrespective of whether the adversarial instance is inserted into y_{targ} (auto – Weber et al.’s attack) or y_{adv} (dog – reformulated attack) test instances – although, as expected, the original attack does have better identification. Mean results are shown graphically in Figure 25.

Test Class	Attack Pattern	Ours	
		GAS	GAS-L
auto (y_{targ})	1 Pixel	0.981 ± 0.020	0.983 ± 0.022
	4 Pixel	0.984 ± 0.029	0.971 ± 0.062
	Blend	0.999 ± 0.003	1.000 ± 0.000
dog (y_{adv})	1 Pixel	0.660 ± 0.294	0.549 ± 0.355
	4 Pixel	0.937 ± 0.215	0.935 ± 0.192
	Blend	0.987 ± 0.033	0.995 ± 0.015

Table 35: Target-Driven Mitigation for the Availability Backdoor Attack: Data sanitization applied to the vision backdoor attack on CIFAR10 class pair $y_{\text{targ}} = \text{auto}$ (Weber et al.’s [78] attack) and $y_{\text{adv}} = \text{dog}$ (our reformulated attack) with 150 backdoor instances and ≥ 10 trials per setup. These results demonstrate that Weber et al.’s backdoor attack can be reformulated as an availability attack that hijacks our framework to remove significant clean training data. The risk of such an attack can be mitigated by modifying Algorithm 4 to include a threshold on mitigation’s maximum effect before additional intervention is initiated. Attack success rate (ASR) is w.r.t. the analyzed target.

Test Class	Attack	Method	% Removed		Te. Acc. %	
			\mathcal{D}_{adv}	\mathcal{D}_{cl}	Orig.	Chg.
auto (y_{targ})	1 Pixel	GAS	47.2	0	98.8	0.0
		GAS-L	48.2	0	98.8	0.0
	4 Pixel	GAS	67.6	0	98.9	0.0
		GAS-L	69.1	0.00	98.9	0.0
dog (y_{adv})	Blend	GAS	67.9	0.00	99.0	-0.1
		GAS-L	69.4	0	99.0	-0.1
	1 Pixel	GAS	94.0	45.77	98.8	-14.8
		GAS-L	89.0	44.90	98.8	-15.4
	4 Pixel	GAS	99.3	51.25	98.9	-20.9
		GAS-L	99.7	36.97	98.9	-9.5
	Blend	GAS	98.6	34.42	99.0	-11.8
		GAS-L	99.2	28.29	99.0	-6.2

F.5 Poisoning-Rate Ablation Study

This section analyzes the effect poisoning rate (i.e., fraction of the training set that is adversarial) has on our method’s performance. Target identification and target-driven attack mitigation rely on successfully identifying the adversarial set \mathcal{D}_{adv} . As such, the ablation study focuses on the effect of poisoning rate on adversarial-instance identification – providing results for all four attacks in Section 6.1.

Recall from Section 6 that our method had the worst performance on Zhu et al.’s [84] vision poisoning attack. Therefore, we focus on that attack and study the effect of poisoning rate on the attack’s target identification and target-driven mitigation performance. For completeness, our ablation study also includes target identification and target-driven mitigation results for one backdoor attack. We selected Liu et al.’s [46] speech recognition backdoor attack since it is a different data modality and dataset than Zhu et al. – unlike Weber et al. [78] which also uses CIFAR10.

Overall, our method was remarkably stable across poisoning rates in all tested cases. Evaluation was limited to those poisoning rates that had $\geq 50\%$ ASR on related experiment setups.

As detailed in Section C.2.4, Liu et al. [47] provide a speech recognition dataset that comes bundled with 300 backdoor training examples, where Liu et al.’s adversarial trigger was white noise inserted at the beginning of the speech recording. Our speech recognition experiments used a *fixed* validation set selected u.a.r. Table 5 details the number of backdoor *training* instances for each speech class pair, with the remaining instances (out of 30) being part of said validation set. The ablation study was limited to ≥ 10 backdoor instances to ensure the attack succeeded for all class pairs.

For Wallace et al.’s [73] natural-language poisoning attack, adversarial sets with fewer than 10 instances did not consistently succeed and are excluded in the analysis below.

Zhu et al.’s [84] vision poisoning attack was limited to $|\mathcal{D}_{\text{adv}}| \leq 400$ since larger quantities exceeded the Nvidia K80’s GPU VRAM capacity of 11.5GB.

The following three subsections visualize our method’s performance across adversarial-set identification, target identification, and attack mitigation, respectively. To improve this section’s readability, tables with the full numerical adversarial-set identification and target identification results (including variance) are deferred to Section F.4.

F.5.1 Adversarial-Set Identification Ablation Study.

To identify the target (Alg. 3) and mitigate the attack (Alg. 4), we must be able to identify the adversarial set, \mathcal{D}_{adv} . Our approach uses (renormalized) influence estimators, which should rank the adversarial set as more influential on the target than clean instances (\mathcal{D}_{cl}). This section evaluates how well different influence estimators perform this ranking for a u.a.r. target across various poisoning rates.

Across all four attacks (Figures 26–29), these experiments highlight GAS(-L)'s stability identifying adversarial set \mathcal{D}_{adv} across the poisoning rate spectrum – even outperforming Section 6's results in many cases.

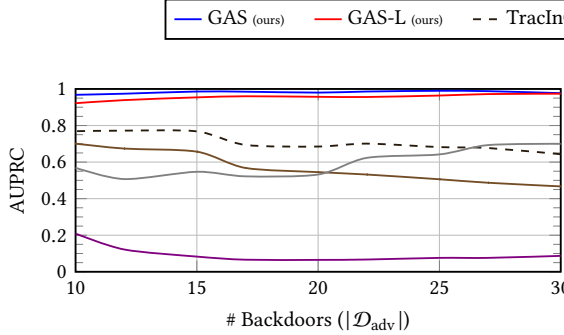


Figure 26: Speech Backdoor Rate Adversarial-Set Identification Ablation Study: Effect of the number of backdoor instances on mean adversarial-set identification AUPRC ($|\mathcal{D}_{\text{cl}}| = 3,000$). GAS's performance improved slightly with fewer adversarial instances, while GAS-L's performance increased with larger \mathcal{D}_{adv} . Results are averaged across related experimental setups with ≥ 10 trials per setup. Table 38 provides the full numerical results, including variance.

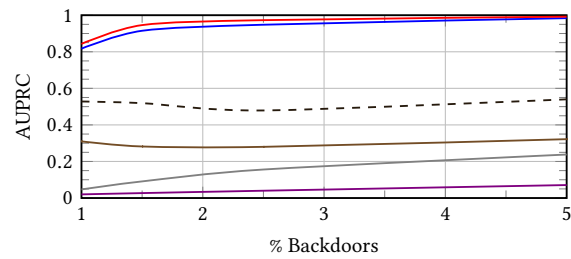


Figure 27: Vision Backdoor Rate Adversarial-Set Identification Ablation Study: Effect of the fraction of the training set that is backdoors on mean adversarial-set identification AUPRC ($|\mathcal{D}_{\text{tr}}| = 10,000$). Only attacks with a minimum success rate of 50% were considered. Results are averaged across related experimental setups with ≥ 10 trials per setup. Table 39 provides the full numerical results, including variance.

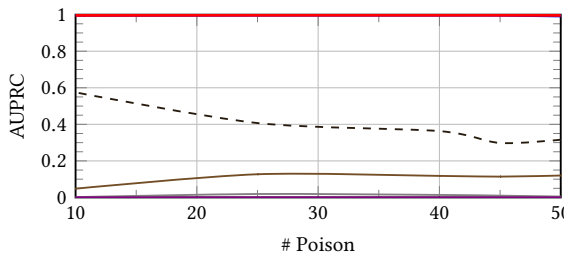


Figure 28: Natural-Language Poisoning Rate Adversarial-Set Identification Ablation Study: Effect of the number of adversarial instances on mean adversarial-set identification AUPRC for Wallace et al.'s [73] natural-language poisoning attack on SST-2 ($|\mathcal{D}_{\text{cl}}| = 67,349$). While TracInCP's performance changes significantly across the entire poisoning rate range, GAS and GAS-L's performance is essentially perfect. Results are averaged across related experimental setups with ≥ 5 trials per setup for each of the first four reviews. Table 40 provides the full numerical results, including variance.

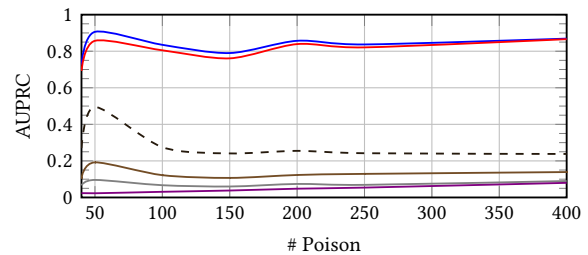


Figure 29: Vision Poisoning Rate Adversarial-Set Identification Ablation Study: Effect of the number of adversarial instances on mean adversarial-set identification AUPRC for Zhu et al.'s [84] vision poisoning attack on CIFAR10 ($|\mathcal{D}_{\text{tr}}| = 25,000$). Results are averaged across related experimental setups with ≥ 10 trials per setup. Only attacks that successfully changed the target's label are considered. The adversarial set was limited to ≤ 400 instances by the Nvidia K80's GPU VRAM capacity of 11.5GB. Table 41 provides the full numerical results, including variance.

F.5.2 Target-Identification Ablation Study.

This section considers poisoning rate's effects on target identification. First, for Liu et al.'s [47] speech backdoor attack, we consider two class pairs, one of which is $1 \rightarrow 2$ for which we observed the worst performance among those speech class pairs tested (see Table 18). Note that in Section 6, $\kappa = 10$ was used to determine the speech attack's upper-tail heaviness. However, these experiments consider the case where adversarial set \mathcal{D}_{adv} has as few as 6 instances. As discussed in Section 5.2, if $|\mathcal{D}_{\text{adv}}| < \kappa$, target identification performance degrades severely. As such, Figure 30 uses an upper-tail count of $\kappa = \min\{10, |\mathcal{D}_{\text{adv}}|\}$.

The other attack considered below is Zhu et al.'s [84] vision poisoning attack on CIFAR10. We selected this attack since it was the one on which we observed the worst target identification performance (see Figure 6.3). Note that as poisoning rate increased, a larger upper-tail count (κ) improved target identification performance. Below we report target identification performance on vision poisoning with $\kappa = 2$ (like in Section 6.3) as well as with $\kappa = 10$.

Overall, target identification was stable across all tested poisoning rates for both the backdoor and poisoning attacks.

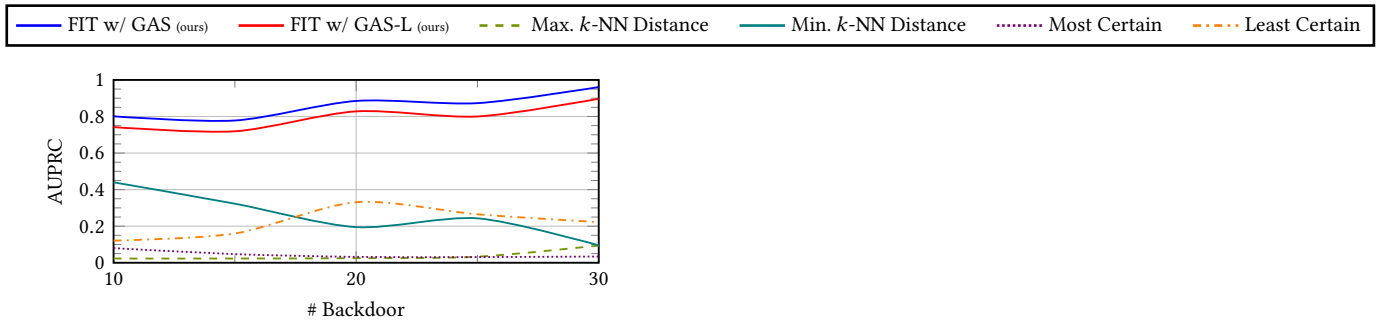


Figure 30: Speech Backdoor Rate Target Identification Ablation Study: Effect of the number of backdoor instances on mean target identification AUPRC for class pairs $0 \rightarrow 1$ and $1 \rightarrow 2$ ($|\mathcal{D}_{\text{cl}}| = 3,000$). Liu et al.'s [47] speech dataset includes 30 backdoor instances per class, which were downsampled uniformly at random. Results are averaged across related experimental setups with ≥ 5 trials per setup. Table 42 provides the full numerical results, including variance.

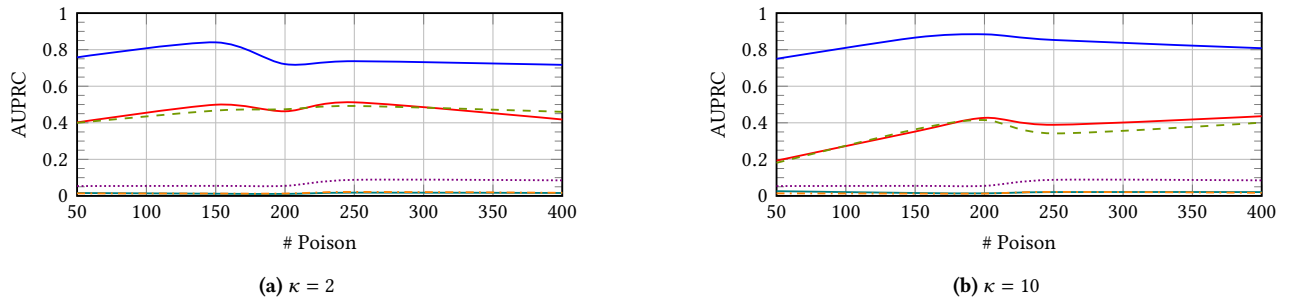


Figure 31: Vision Poisoning Rate Target Identification Ablation Study: Effect of the number of adversarial instances on mean target identification AUPRC for Zhu et al.'s [84] vision poisoning attack on CIFAR10 ($|\mathcal{D}_{\text{tr}}| = 25,000$). Results are averaged across all four class pairs with ≥ 10 trials per setup. Table 43 provides the full numerical results, including variance.

F.5.3 Target-Driven Attack Mitigation Ablation Study.

This section considers poisoning rate's effects on target-driven attack mitigation – specifically for the speech backdoor and vision poisoning attacks. In both cases, the fraction of clean data removed was slightly larger when the adversarial set was small.

For Zhu et al.'s [84] vision poisoning attack, the average fraction of clean data removed was $\leq 0.26\%$ across the poisoning rate range – a very small fraction. Similarly, the test accuracy post-sanitization never lagged the baseline test accuracy by more than 0.2%; see Table 43 for the baseline results.

Table 36: Speech Backdoor Rate Target-Driven Attack Mitigation Ablation Study: Algorithm 4's target-driven, iterative data sanitization applied to Liu et al.'s [47] backdoored speech recognition dataset for class pairs $0 \rightarrow 1$ and $1 \rightarrow 2$ across different backdoor quantities ($|\mathcal{D}_{cl}| = 3,000$). The attacks were neutralized with few clean instances removed and little change in test accuracy. Attack success rate (ASR) is w.r.t. specifically the analyzed target. Bold denotes the best mean performance with 10 trials per class pair.

# BD	Digits		Method	% Removed		ASR %		Test Acc. %	
	y_{targ}	y_{adv}		\mathcal{D}_{adv}	\mathcal{D}_{cl}	Orig.	Ours	Orig.	Chg.
10	0	1	GAS	100	0.17	97.2	0	97.7	0.0
			GAS-L	100	0.08		0		0.0
	1	2	GAS	99.0	0.03		0	97.8	0.0
			GAS-L	98.7	0.07	100	0		0.0
15	0	1	GAS	100	0.12	99.8	0	97.8	-0.1
			GAS-L	100	0.08		0		-0.1
	1	2	GAS	99.4	0.04		0	97.8	-0.1
			GAS-L	98.8	0.07	100	0		0.0
20	0	1	GAS	100	0.04	100	0	97.7	0.0
			GAS-L	100	0.02		0		-0.1
	1	2	GAS	99.3	0.00		0	97.7	0.0
			GAS-L	100	0.04	100	0		-0.1
25	0	1	GAS	100	0.07	100	0	97.8	0.0
			GAS-L	100	0.02		0		0.0
	1	2	GAS	99.7	0.00		0	97.8	0.0
			GAS-L	99.3	0.13	100	0		-0.1
30	0	1	GAS	100	0.06	100	0	97.7	0.0
			GAS-L	100	0.03		0		0.0
	1	2	GAS	100.0	0.02		0	97.7	0.0
			GAS-L	99.8	0.09	100	0		0.0

Table 37: Vision Poisoning Rate Target-Driven Attack Mitigation Ablation Study: Algorithm 4’s target-driven, iterative data sanitization applied to Zhu et al.’s [84] vision poisoning attack on CIFAR10 for class pairs **bird → dog** and **dog → bird** ($|\mathcal{D}_{\text{tr}}| = 25,000$). The attacks were neutralized with few clean instances removed and little change in test accuracy. Attack success rate (ASR) is w.r.t. specifically the analyzed target. **Bold** denotes the best mean performance with ≥ 5 trials per class pair.

# Pois.	Classes		Method	% Removed		ASR %		Test Acc. %	
	y_{targ}	y_{adv}		\mathcal{D}_{adv}	\mathcal{D}_{cl}	Orig.	Ours	Orig.	Chg.
50	Bird	Dog	GAS	38.0	0.08	93.8	0	87.0	+0.2
			GAS-L	26.4	0.07	0	0		+0.4
	Dog	Bird	GAS	43.2	0.00	68.8	0	87.1	0.0
			GAS-L	31.2	0.00	0	0		0.0
150	Bird	Dog	GAS	51.6	0.07	75.0	0	86.9	+0.1
			GAS-L	55.3	0.13	0	0		+0.1
	Dog	Bird	GAS	45.8	0.03	62.5	0	87.1	+0.1
			GAS-L	37.0	0.00	0	0		-0.1
200	Bird	Dog	GAS	67.7	0.07	68.8	0	87.0	0.0
			GAS-L	72.1	0.11	0	0		0.0
	Dog	Bird	GAS	50.1	0.02	62.5	0	87.3	-0.2
			GAS-L	37.2	0.00	0	0		-0.2
250	Bird	Dog	GAS	60.3	0.08	87.5	0	87.0	-0.1
			GAS-L	46.6	0.02	0	0		-0.2
	Dog	Bird	GAS	28.8	0.00	81.3	0	87.2	-0.2
			GAS-L	26.4	0.00	0	0		0.0
400	Bird	Dog	GAS	68.1	0.18	87.5	0	86.9	+0.1
			GAS-L	63.1	0.26	0	0		0.0
	Dog	Bird	GAS	64.3	0.06	43.8	0	87.1	0.0
			GAS-L	42.5	0.04	0	0		+0.3

F.5.4 Ablation Study Reference Tables.

As explained above, the ablation study's result tables were deferred until this section to improve overall readability.

Table 38: Speech Backdoor Rate Adversarial-Set Identification Ablation Study: Mean and standard deviation adversarial-instance identification AUPRC for Liu et al.'s [47] speech dataset, which contains 30 backdoor instances per class pair and 3,000 total clean instances. Bold denotes the best mean performance with ≥ 10 trials per setup. The backdoor count includes examples held-out as part of the fixed validation set (see Table 5), with results limited to ≥ 10 backdoor instances to ensure the attack succeeds consistently for all class pairs. These experiments highlight the stability of GAS and GAS-L at identifying adversarial set \mathcal{D}_{adv} even at small poisoning rates. Results are shown graphically in Figure 26.

# Backdoors	Ours		Baselines			
	GAS	GAS-L	TracInCP	TracIn	Influence Func.	Representer Pt.
10	0.968 ± 0.059	0.922 ± 0.090	0.769 ± 0.117	0.701 ± 0.136	0.569 ± 0.150	0.140 ± 0.082
12	0.974 ± 0.047	0.939 ± 0.081	0.772 ± 0.142	0.674 ± 0.154	0.507 ± 0.170	0.116 ± 0.069
15	0.986 ± 0.026	0.954 ± 0.055	0.768 ± 0.175	0.657 ± 0.199	0.547 ± 0.149	0.097 ± 0.038
17	0.985 ± 0.021	0.960 ± 0.039	0.694 ± 0.224	0.568 ± 0.208	0.522 ± 0.167	0.100 ± 0.074
20	0.980 ± 0.038	0.957 ± 0.059	0.685 ± 0.186	0.545 ± 0.162	0.532 ± 0.168	0.099 ± 0.087
22	0.986 ± 0.022	0.956 ± 0.044	0.701 ± 0.212	0.532 ± 0.191	0.623 ± 0.129	0.078 ± 0.086
25	0.990 ± 0.019	0.964 ± 0.044	0.682 ± 0.224	0.506 ± 0.178	0.642 ± 0.135	0.090 ± 0.063
27	0.988 ± 0.025	0.972 ± 0.040	0.677 ± 0.185	0.487 ± 0.155	0.693 ± 0.125	0.082 ± 0.072
30	0.977 ± 0.037	0.974 ± 0.033	0.643 ± 0.211	0.467 ± 0.149	0.700 ± 0.135	0.087 ± 0.030

Table 39: Vision Backdoor Rate Adversarial-Set Identification Ablation Study: Mean and standard deviation adversarial-instance identification AUPRC for Weber et al.'s [78] vision backdoor attack with ≥ 7 trials per experimental setup ($|\mathcal{D}_{\text{tr}}| = 10,000$). Bold denotes the best mean performance. These experiments highlight the stability of GAS and GAS-L at identifying adversarial set \mathcal{D}_{adv} . Attacks were limited to ≥ 100 backdoor instances to ensure $\geq 50\%$ attack success rate. Results are shown graphically in Figure 27.

% Backdoor	Ours		Baselines			
	GAS	GAS-L	TracInCP	TracIn	Influence Func.	Representer Pt.
1	0.848 ± 0.208	0.866 ± 0.189	0.517 ± 0.229	0.288 ± 0.137	0.067 ± 0.041	0.027 ± 0.011
1.5	0.915 ± 0.106	0.946 ± 0.076	0.519 ± 0.220	0.282 ± 0.123	0.091 ± 0.051	0.027 ± 0.005
2.5	0.948 ± 0.066	0.973 ± 0.034	0.479 ± 0.198	0.280 ± 0.118	0.156 ± 0.115	0.040 ± 0.009
5	0.984 ± 0.022	0.992 ± 0.012	0.540 ± 0.140	0.322 ± 0.087	0.238 ± 0.104	0.071 ± 0.015

Table 40: Natural-Language Poisoning Rate Adversarial-Set Identification Ablation Study: Mean and standard deviation adversarial-instance identification AUPRC for Wallace et al.’s [73] natural-language poisoning attack on SST-2 for different poisoning rates ($|\mathcal{D}_{\text{cl}}| = 67,349$). Results are averaged across related experimental setups with ≥ 5 trials per setup for each of the first four reviews with the best mean performance in bold. Only attacks that successfully changed the target’s label are considered. For attacks with adversarial sets smaller than 10, the target’s label did not consistently change and are excluded. Results are shown graphically in Figure 28.

# Poison	Ours		Baselines			
	GAS	GAS-L	TracInCP	TracIn	Influence Func.	Representer Pt.
10	0.999 ± 0.004	0.999 ± 0.002	0.575 ± 0.512	0.048 ± 0.041	0.002 ± 0.001	0.001 ± 0.001
25	1 ± 0	1 ± 0	0.407 ± 0.290	0.127 ± 0.084	0.019 ± 0.033	0.001 ± 0.001
40	1.000 ± 0.001	1.000 ± 0.000	0.363 ± 0.325	0.118 ± 0.110	0.014 ± 0.020	0.001 ± 0.001
45	1.000 ± 0.001	1.000 ± 0.000	0.298 ± 0.281	0.114 ± 0.096	0.010 ± 0.011	0.001 ± 0.001
50	0.996 ± 0.023	0.999 ± 0.002	0.316 ± 0.259	0.120 ± 0.098	0.005 ± 0.002	0.001 ± 0.001

Table 41: Vision Poisoning Rate Adversarial-Set Identification Ablation Study: Mean and standard deviation adversarial-instance identification AUPRC for Zhu et al.’s [84] vision poisoning attack on CIFAR10 across different poisoning rates ($|\mathcal{D}_{\text{tr}}| = 25,000$). These experiments highlight the stability of GAS and GAS-L at identifying adversarial set \mathcal{D}_{adv} even at small poisoning rates. In contrast, TracInCP’s performance changes significantly across the entire poisoning rate range. Results are averaged across related experimental setups with ≥ 10 trials per setup with the best mean performance in bold. Only attacks that successfully changed the target’s label are considered. Results are shown graphically in Figure 29.

# Poison	Ours		Baselines			
	GAS	GAS-L	TracInCP	TracIn	Influence Func.	Representer Pt.
40	0.726 ± 0.085	0.692 ± 0.092	0.270 ± 0.030	0.107 ± 0.011	0.066 ± 0.020	0.025 ± 0.007
50	0.906 ± 0.054	0.857 ± 0.102	0.495 ± 0.063	0.192 ± 0.023	0.096 ± 0.036	0.023 ± 0.006
100	0.835 ± 0.061	0.805 ± 0.055	0.275 ± 0.068	0.122 ± 0.017	0.067 ± 0.022	0.031 ± 0.004
150	0.790 ± 0.074	0.761 ± 0.082	0.241 ± 0.013	0.107 ± 0.006	0.060 ± 0.015	0.038 ± 0.003
200	0.857 ± 0.074	0.839 ± 0.063	0.255 ± 0.042	0.123 ± 0.017	0.074 ± 0.021	0.048 ± 0.005
250	0.837 ± 0.046	0.821 ± 0.050	0.242 ± 0.043	0.129 ± 0.016	0.069 ± 0.015	0.054 ± 0.004
400	0.869 ± 0.046	0.866 ± 0.059	0.238 ± 0.017	0.139 ± 0.013	0.090 ± 0.014	0.080 ± 0.005

Table 42: Speech Backdoor Rate Target Identification Ablation Study: Mean and standard deviation target identification AUPRC for Liu et al.’s [47] speech dataset across different backdoor quantities ($|\mathcal{D}_{\text{cl}}| = 3,000$). We consider class pairs $0 \rightarrow 1$ and $1 \rightarrow 2$ with ≥ 5 trials per setup. Liu et al.’s [47] speech dataset includes 30 backdoor instances per class which were downsampled uniformly at random. Results are averaged across related experimental setups with ≥ 5 trials per setup with the best mean performance in bold. Results are shown graphically in Figure 30.

# Backdoors	Ours		Baselines				
	GAS	GAS-L	Max k -NN	Min k -NN	Most Certain	Least Certain	Random
10	0.801 ± 0.158	0.742 ± 0.155	0.023 ± 0.001	0.440 ± 0.052	0.080 ± 0.072	0.121 ± 0.070	0.070 ± 0.045
15	0.778 ± 0.103	0.719 ± 0.147	0.023 ± 0.001	0.323 ± 0.039	0.047 ± 0.022	0.160 ± 0.082	0.050 ± 0.016
20	0.885 ± 0.150	0.828 ± 0.151	0.025 ± 0.002	0.195 ± 0.089	0.032 ± 0.008	0.331 ± 0.207	0.064 ± 0.034
25	0.873 ± 0.095	0.800 ± 0.067	0.033 ± 0.010	0.243 ± 0.067	0.031 ± 0.010	0.265 ± 0.156	0.069 ± 0.043
30	0.961 ± 0.038	0.897 ± 0.086	0.094 ± 0.057	0.095 ± 0.032	0.034 ± 0.013	0.222 ± 0.224	0.063 ± 0.027

Table 43: Vision Poisoning Rate Target Identification Ablation Study: Mean and standard deviation target identification AUPRC for Zhu et al.’s [84] vision poisoning attack on CIFAR10 across different poisoning rates ($|\mathcal{D}_{\text{tr}}| = 25,000$). Results are averaged across all four class pairs with ≥ 10 trials per setup with the best mean performance in bold. Results are shown graphically in Figure 31.

(a) $\kappa = 2$

# Poison	Ours		Baselines				
	GAS	GAS-L	Max k -NN	Min k -NN	Most Certain	Least Certain	Random
50	0.758 ± 0.251	0.402 ± 0.364	0.400 ± 0.411	0.016 ± 0.013	0.054 ± 0.047	0.014 ± 0.004	0.039 ± 0.052
150	0.840 ± 0.239	0.499 ± 0.347	0.467 ± 0.427	0.012 ± 0.005	0.055 ± 0.047	0.013 ± 0.003	0.053 ± 0.091
200	0.721 ± 0.309	0.463 ± 0.342	0.474 ± 0.398	0.011 ± 0.003	0.055 ± 0.040	0.013 ± 0.003	0.046 ± 0.071
250	0.737 ± 0.309	0.512 ± 0.394	0.492 ± 0.415	0.018 ± 0.018	0.088 ± 0.130	0.022 ± 0.017	0.087 ± 0.135
400	0.717 ± 0.301	0.418 ± 0.371	0.460 ± 0.430	0.016 ± 0.016	0.085 ± 0.139	0.017 ± 0.010	0.069 ± 0.111

(b) $\kappa = 10$

# Poison	Ours		Baselines				
	GAS	GAS-L	Max k -NN	Min k -NN	Most Certain	Least Certain	Random
50	0.750 ± 0.310	0.193 ± 0.225	0.181 ± 0.319	0.016 ± 0.013	0.054 ± 0.047	0.014 ± 0.004	0.039 ± 0.052
150	0.866 ± 0.162	0.352 ± 0.298	0.364 ± 0.418	0.012 ± 0.005	0.055 ± 0.047	0.013 ± 0.003	0.053 ± 0.091
200	0.884 ± 0.190	0.427 ± 0.350	0.415 ± 0.445	0.011 ± 0.003	0.055 ± 0.040	0.013 ± 0.003	0.046 ± 0.071
250	0.853 ± 0.265	0.389 ± 0.384	0.342 ± 0.399	0.018 ± 0.018	0.088 ± 0.130	0.022 ± 0.017	0.087 ± 0.135
400	0.808 ± 0.309	0.436 ± 0.384	0.401 ± 0.458	0.016 ± 0.016	0.085 ± 0.139	0.017 ± 0.010	0.069 ± 0.111

F.6 Upper-Tail Heaviness Hyperparameter κ Sensitivity Analysis

Section 5.2 defines the upper-tail heaviness of influence vector v as the κ -th largest anomaly score in vector σ . Test examples in set $\hat{\mathcal{Z}}_{te}$ are then ranked by their respective heaviness with those highest ranked more commonly targets.

Figure 32 reports GAS's and GAS-L's target identification AUPRC for the vision backdoor [78] and natural language poisoning [73] attacks across a range of κ values. In all cases, our performance is remarkably stable. For example, GAS-L's and GAS's natural language target identification AUPRC varied only 0.2% and 2.1% respectively for all tested $\kappa \in [1, 25]$. The vision backdoor target identification AUPRC varied only 1.8% and 5.8% respectively for $\kappa \in [2, 50]$.

Recall from Section 6.1 that the vision backdoor adversarial set is three times larger than that of natural language poisoning (150 vs. 50). That is why vision backdoor target identification's performance is stable over a wider range of κ values than natural language poisoning.

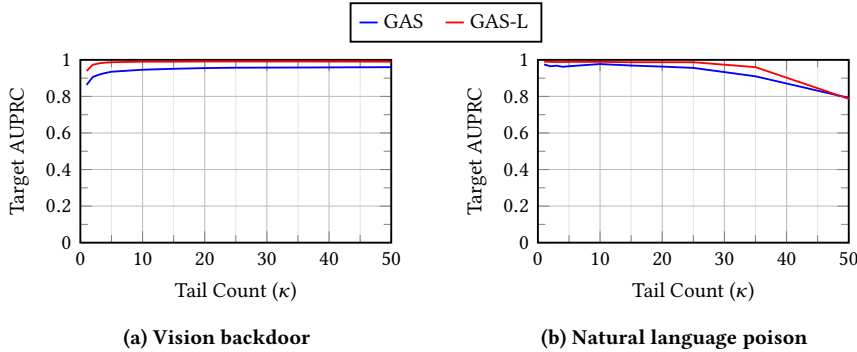


Figure 32: Upper-Tail Heaviness Hyperparameter (κ) Sensitivity Analysis: Mean target identification AUPRC across a range of tail-heaviness values (κ) for GAS and GAS-L. Target identification performance fluctuates very little even when κ changes by more than an order of magnitude. Results are averaged across all experimental setups/class pairs with ≥ 10 trials per setup.

F.7 Alternatives to Renormalization

Renormalization directly addresses the low-loss penalty of Yeh et al.'s [81] representer point estimator by normalizing by $\|\frac{\partial \mathcal{L}(z_i; \theta_T)}{\partial a_{y_i}}\|$. For the other influence estimators (TracIn, TracInCP, and influence functions), a slightly different approach is taken.

For influence estimator \mathcal{I} , Section 4.3 defines that renormalized influence $\tilde{\mathcal{I}}$ replaces each gradient vector g in \mathcal{I} with unit vector $\frac{g}{\|g\|}$. This modified approach does not correct solely for the low-loss penalty. This choice was made for a few reasons. First, loss and gradient magnitude are generally very tightly coupled as shown in Figure 2, making the two often interchangeable. In addition, most automatic differentiation frameworks (e.g., torch) do not directly return just the loss function's gradient; rather, they provide the gradient for each parameter. It is therefore an easier implementation to normalize by the full gradient's magnitude. Lastly, using the full gradient vector's norm also corrects for variance in the other parts of the gradient's magnitude – specifically w.r.t. the parameter values.

This section examines the change in GAS's performance had $\|\frac{\partial \mathcal{L}(z_i; \theta_T)}{\partial a_{y_i}}\|$ been used to renormalize TracInCP instead of $\|g\|$. Figure 33 compares those two approaches against the TracInCP baseline for the CIFAR10 & MNIST joint training experiment in Section 4.1 as well as Section 6.2's adversarial-set identification experiments.³¹ As in the original experiments, performance was measured using AUPRC.

For backdoor vision and poison, performance was comparable irrespective of which of the two renormalization schemes was used. Renormalizing TracInCP using $\|\frac{\partial \mathcal{L}(z_i; \theta_T)}{\partial a_{y_i}}\|$ actually performed better on the CIFAR10 & MNIST joint training experiment, achieving near-perfect (0.998) mean AUPRC. In contrast, GAS was the top performer for the natural language poisoning experiments. The performance difference on that baseline is primarily due to RoBERTaBASE's very large model size and the large variance that can induce on the magnitude of vector $\frac{\partial a}{\partial x}$.

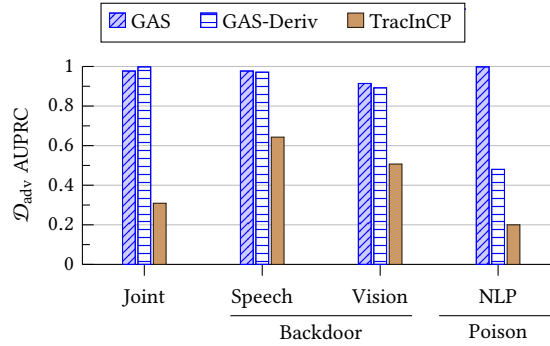


Figure 33: Alternate GAS Renormalization Using $\|\frac{\partial \mathcal{L}(z_i; \theta_T)}{\partial a_{y_i}}\|$: Mean \mathcal{D}_{adv} identification AUPRC for the CIFAR10 & MNIST joint training and adversarial attack experiments. For the two backdoor attacks, both renormalization schemes performed similarly. Renormalization using only the loss function's norm performed best for the joint training experiments while GAS was the top performer for natural language poisoning. Results are averaged across all experimental setups/class pairs with ≥ 10 trials per setup.

Barshan et al. [4] propose *relative influence*, which normalizes specifically influence functions by Hessian-vector product (HVP), $H_\theta^{-1} g_i$. They theoretically motivate their method via a global-vs.-local influence tradeoff. However, as Barshan et al. acknowledge, their method is computationally intractable. Estimating a single HVP can take up to several hours. Since Hessian-vector product $H_\theta^{-1} g_i$ must be calculated for *each training instance* z_i , Barshan et al. only evaluate their method on training sets of a few hundred instances. Even if it were computationally feasible, existing HVP-estimation methods are fragile and generally perform poorly on large models [5].

Moreover, relative influence is specific to influence functions while our renormalized influence in Section 4 applies generally to all loss-based influence estimators (e.g., TracIn, HyDRA, representer point). An additional consequence of that is Barshan et al. do not consider normalizing by test gradient magnitude $\|\hat{g}_e\|$ to prevent penalizing low-loss training *iterations*.

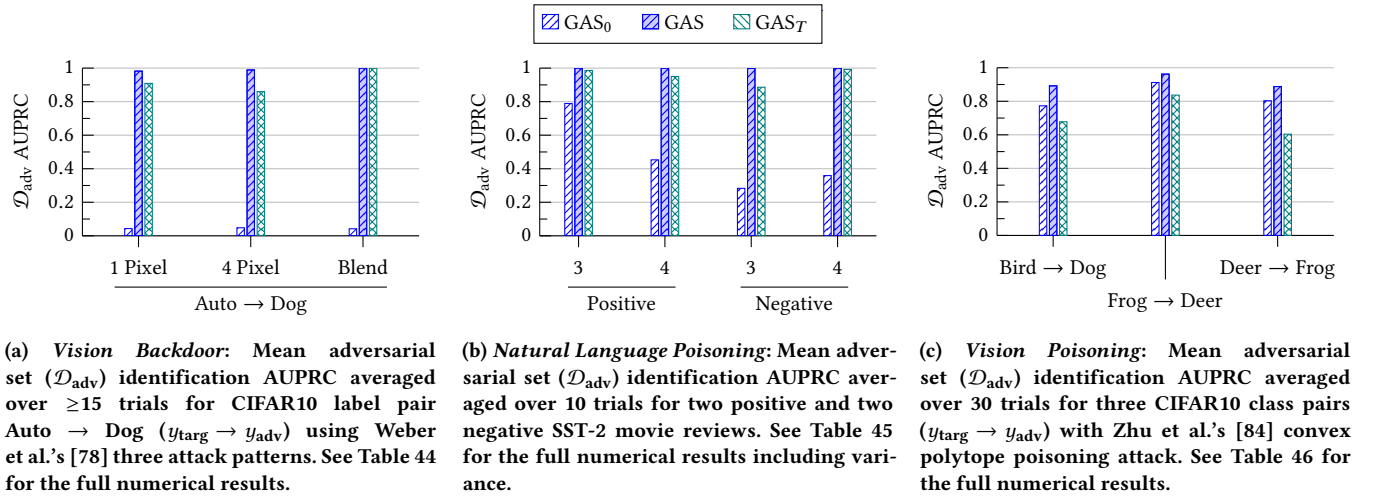
³¹At the time of submission, data collection for Zhu et al.'s [84] vision poisoning attack had not yet completed.

F.8 Why Aggregate Training Gradients?

Recall from Section 3.2 that *static influence estimators* (e.g., influence functions [35], representer point [81]) quantify influence using only final model parameters θ_T . In contrast, *dynamic influence estimators* (e.g., TracIn & TracInCP [57], HyDRA [12]) quantify influence by aggregating changes across (a subset of) intermediate training parameters, $\theta_0, \dots, \theta_T$. These experiments examine the benefit of gradient aggregation for our renormalized influence estimator, GAS, which is based on TracInCP.

Similar to Section 6.2's experimental setup, Figure 34 compares the mean adversarial set (\mathcal{D}_{adv}) identification AUPRC for GAS against two custom variants GAS_0 and GAS_T , where GAS_τ denotes that the corresponding iteration subset is $\mathcal{T} = \{\tau\}$.³² In all cases, GAS aggregation outperformed the single best checkpoint on average. Therefore, even if the optimal checkpoint could be known via an oracle, it still may not beat aggregation in many cases. In particular for poisoning but also for Weber et al.'s [78] vision backdoor attack where the adversarial trigger may be clipped, each adversarial instance in \mathcal{D}_{adv} may not have the same attack pattern/data. Therefore, instances in \mathcal{D}_{adv} may be most influential at different points in training depending on when the corresponding adversarial feature(s) best aligns with the target. Averaging across multiple checkpoints enables dynamic methods to potentially detect all such points in training.

Note also that θ_T was better at identifying \mathcal{D}_{adv} for only two of three attacks, namely natural-language poisoning and vision backdoor. For vision poisoning, θ_0 yielded better identification. This performance difference is *not* due to whether θ_0 is pre-trained as both poisoning attacks used pre-trained models.



(a) *Vision Backdoor*: Mean adversarial set (\mathcal{D}_{adv}) identification AUPRC averaged over ≥ 15 trials for CIFAR10 label pair Auto → Dog ($y_{\text{targ}} \rightarrow y_{\text{adv}}$) using Weber et al.'s [78] three attack patterns. See Table 44 for the full numerical results.

(b) *Natural Language Poisoning*: Mean adversarial set (\mathcal{D}_{adv}) identification AUPRC averaged over 10 trials for two positive and two negative SST-2 movie reviews. See Table 45 for the full numerical results including variance.

(c) *Vision Poisoning*: Mean adversarial set (\mathcal{D}_{adv}) identification AUPRC averaged over 30 trials for three CIFAR10 class pairs ($y_{\text{targ}} \rightarrow y_{\text{adv}}$) with Zhu et al.'s [84] convex polytope poisoning attack. See Table 46 for the full numerical results.

Figure 34: Gradient Aggregation: Mean GAS adversarial set (\mathcal{D}_{adv}) identification AUPRC when considering the initial ($t = 0$) and final ($t = T$) checkpoints individually versus aggregating across multiple checkpoints. Vision and natural language poisoning used pre-trained initial parameters θ_0 while vision backdoor's θ_0 was randomly initialized. See Section C.2 for each of these experiments' hyperparameter settings.

³²For example, GAS_0 denotes $\mathcal{T} = \{0\}$, i.e., only initial parameters θ_0 are analyzed.

Table 44: Vision Backdoor Gradient Aggregation: Adversarial set (\mathcal{D}_{adv}) identification AUPRC mean and standard deviation averaged over ≥ 15 trials for CIFAR10 label pair Auto \rightarrow Dog ($y_{\text{targ}} \rightarrow y_{\text{adv}}$) using Weber et al.'s [78] three attack patterns. Following Weber et al.'s [78] experimental setup, θ_0 was randomly initialized causing GAS₀ as expected to perform poorly. Bold denotes the best mean performance. Mean values are shown graphically in Figure 34a.

$y_{\text{targ}} \rightarrow y_{\text{adv}}$	Attack	GAS ₀	GAS	GAS _T
Auto \rightarrow Dog	1 Pixel	0.043 ± 0.015	0.982 ± 0.015	0.909 ± 0.069
	4 Pixel	0.048 ± 0.021	0.989 ± 0.033	0.860 ± 0.137
	Blend	0.042 ± 0.021	1 ± 0	0.999 ± 0.002

Table 45: Natural Language Poisoning Gradient Aggregation: Adversarial set (\mathcal{D}_{adv}) identification AUPRC mean and standard deviation averaged over 10 trials for two positive and two negative SST-2 movie reviews. Bold denotes the best mean performance. Mean values are shown graphically in Figure 34b.

Sentiment	No.	GAS ₀	GAS	GAS _T
Pos.	3	0.789 ± 0.144	1 ± 0	0.986 ± 0.037
	4	0.453 ± 0.066	1 ± 0	0.950 ± 0.083
Neg.	3	0.283 ± 0.087	0.998 ± 0.005	0.886 ± 0.213
	4	0.359 ± 0.108	1 ± 0	0.992 ± 0.025

Table 46: Vision Poisoning Gradient Aggregation: Adversarial set (\mathcal{D}_{adv}) identification AUPRC mean and standard deviation averaged over 30 trials for three CIFAR10 class pairs ($y_{\text{targ}} \rightarrow y_{\text{adv}}$) with Zhu et al.'s [84] convex polytope poisoning attack. Bold denotes the best mean performance. Mean values are shown graphically in Figure 34c.

$y_{\text{targ}} \rightarrow y_{\text{adv}}$		GAS ₀	GAS	GAS _T
Bird	Dog	0.773 ± 0.208	0.892 ± 0.137	0.678 ± 0.265
Frog	Deer	0.912 ± 0.120	0.962 ± 0.100	0.837 ± 0.160
Deer	Frog	0.803 ± 0.188	0.888 ± 0.091	0.604 ± 0.234

F.9 Evaluating on the Tail of the Attack’s Influence Distribution

When the number of attack instances is larger than necessary, it becomes increasingly important to detect all of the adversarial set (with very few false positives) in order to mitigate the attack and minimize damage. As a complement to this paper’s identification and mitigation experiments, here we evaluate one specific aspect of our method in one specific challenging setting: performance on the 10% most difficult instances in the attack.

Figure 35 considers this case on Weber et al.’s [78] three vision backdoor attack patterns. Each attack’s maximum perturbation distance is halved w.r.t. the earlier experiments (to reduce their individual influence and increase the challenge) and 1,000 adversarial instances (10% of \mathcal{D}_{tr}) are used. Each method’s gray bar represents the adversarial-instance identification AUPRC when considering the entire adversarial set \mathcal{D}_{adv} . The purple bar shows the adversarial-instance identification AUPRC for just the bottom 10% least influential backdoor training instances. This quantity is necessarily less than or equal to the AUPRC for the full \mathcal{D}_{adv} . This experiment mimics an attacker secretly concealing from our defense the top-90% of \mathcal{D}_{adv} . Figures 36 and 37 provide similar results for the Wallace et al.’s [73] natural-language poisoning and Liu et al.’s [47] speech recognition backdoor attacks respectively.

In summary, GAS(-L) were highly adept at detecting these least influential instances for all three attacks. In contrast, the baseline estimators’ performance drops substantially – generally to nearly zero AUPRC.

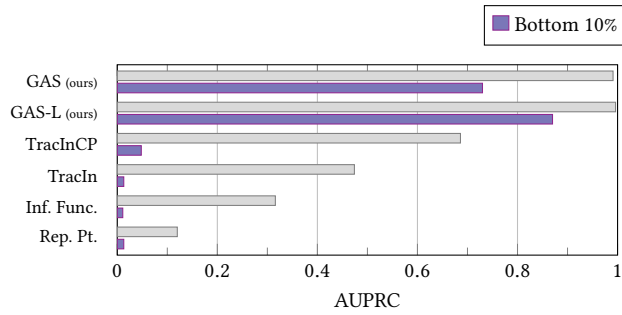


Figure 35: Vision Backdoor Adversarial-Set Identification of the Least Influential Instances: Mean AUPRC identifying adversarial set \mathcal{D}_{adv} for Weber et al.’s [78] vision backdoor with 1,000 backdoor instances. Even if the attacker can conceal the top 90% most influential instances from our defense (purple), GAS(-L) remain highly effective at identifying the adversarial set – unlike the baselines whose performance severely degrades. Results are averaged across related experimental setups with ≥ 10 trials per setup.

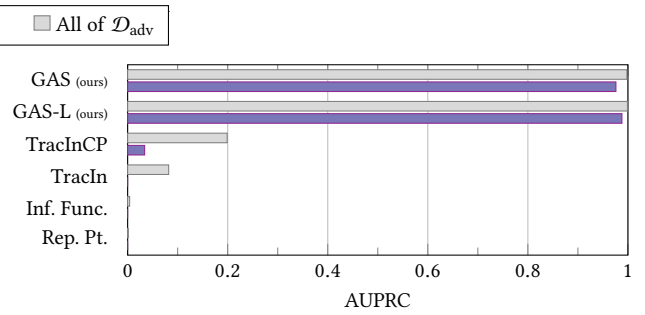


Figure 36: Natural-Language Poison Adversarial-Set Identification of the Least Influential Instances: Mean AUPRC identifying adversarial set \mathcal{D}_{adv} for Wallace et al.’s [73] natural-language poisoning attack. Even if the attacker can conceal the top 90% most influential instances (i.e., top 45/50 instances) from our defense (purple), GAS(-L) remain highly effective at identifying \mathcal{D}_{adv} even for these 10% least-influential instances (bottom 5/50). Results are averaged across related experimental setups with 10 trials per setup.

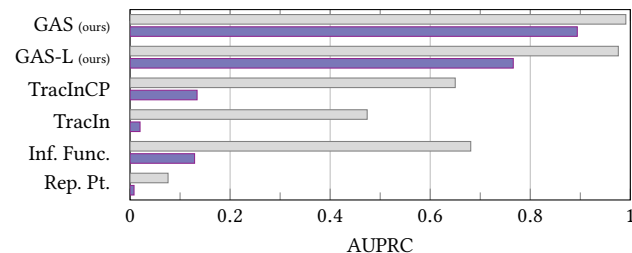


Figure 37: Speech Backdoor Adversarial-Set Identification of the Least Influential Instances: Mean AUPRC identifying adversarial set \mathcal{D}_{adv} for Liu et al.’s [47] speech backdoor attack. Even if the attacker can conceal the top 90% most influential instances (top 27/30 instances) from our defense (purple), our method still remains highly effective at identifying the adversarial set using just the 10% least influential instances (bottom 3/30 instances). Results are averaged across related experimental setups with ≥ 10 trials per setup.

F.10 Adversarial-Set Identification Execution Time

Recall from Section 4.3 that GAS(-L) is a renormalized version of TracInCP that removes the low-loss penalty. Therefore, GAS(-L)'s execution time is, in essence, that of TracInCP. Table 47 compares the execution time of TracInCP/GAS(-L) to the other influence estimators.³³ All results were collected on an HPC system with 3 Intel E5-2690v4 cores, 48GB of 2400MHz DDR4 RAM, and one NVIDIA Tesla K80. The reported execution times consider calculating vector v for training set \mathcal{D}_{tr} w.r.t. a *single* random test example \hat{z}_{te} . The only exception is the “Amortized” results where training gradient (g_i) computation is amortized across multiple test examples allowing for significant speed-up (see Alg. 2). Amortization relies on simultaneously storing each test example's gradient \hat{g}_{te} in GPU memory. Therefore, the GPU model constrains amortization's possible benefits. Table 48 enumerates the number of concurrent test examples considered when calculating amortized results on a K80. More modern GPUs with larger onboard memory see considerable single and amortized speed-ups compared to Table 47.

Recall from Section 6 that natural-language poisoning attacked RoBERTaBASE (125M parameters) as specified by Wallace et al. [73]. Large models can be slow to analyze – even with amortization. That is why natural language target identification uses the two-phase target identification procedure described in Section 5.2. We observed no meaningful performance drop with this streamlined approach (see Figure 7).

Recall from Section 3.2 that Yeh et al.'s [81] representer point estimator only considers the network's final linear classification layer, which is why it was the fastest. Notably, it also had the worst performance (see Figure 6).

For completeness, Peri et al.'s [55] Deep k -NN empirical clean-label data poisoning defense's mean execution time was 242s with standard deviation 1.1s.

Target identification execution times can be extrapolated from Table 47's “Amortized” values.

Table 47: Adversarial-Set Identification Execution Time: Mean and standard deviation algorithm execution time (in seconds) to analyze a single test instance across >50 trials for GAS(-L) and the influence estimator baselines on Section 6.1's four training-set attacks. See Table 48 for the number of parallel instances analyzed by TracInCP and GAS(-L) for each attack.

Attack	Type	Dataset	TracInCP & GAS(-L)		Others		
			Single	Amortized	TracIn	Inf. Func.	Rep. Pt.
Backdoor	Speech	[47]	2,605 ± 710	489 ± 155	894 ± 279	4,595 ± 177	49 ± 1
	Vision	CIFAR10	9,252 ± 2,253	1,473 ± 408	2,418 ± 738	6,316 ± 250	128 ± 3
Poison	NLP	SST-2	27,723 ± 7,933	8,971 ± 3,719	16,667 ± 187	21,409 ± 77	1,697 ± 11
	Vision	CIFAR10	24,267 ± 1,939	2,088 ± 177	5,910 ± 600	15,634 ± 641	187 ± 2

Table 48: Single GPU Amortization: Number of test examples analyzed by TracInCP/GAS(-L) when amortizing on an Nvidia Tesla K80 computation of training gradients (g_i) in Table 47's “Amortized” execution time result.

	Attack	Type	
Backdoor	Speech	20	
	Vision	16	
Poison	NLP	5	
	Vision	135	

³³Table 47 does not separately report GAS and GAS-L's execution times as they were consistently similar to TracInCP.